



Synthesis of WSi_2 from Scheelite (CaWO_4) by Self-Propagating High-Temperature Synthesis (SHS) Process

Si Thu Myint Maung

**A Thesis Submitted in Fulfillment of the Requirements for the
Degree of Master of Engineering in Materials Engineering
Prince of Songkla University
2018**

Copyright of Prince of Songkla University



Synthesis of WSi_2 from Scheelite (CaWO_4) by Self-Propagating High-Temperature Synthesis (SHS) Process

Si Thu Myint Maung

**A Thesis Submitted in Fulfillment of the Requirements for the
Degree of Master of Engineering in Materials Engineering
Prince of Songkla University
2018**

Copyright of Prince of Songkla University

Thesis Title Synthesis of WSi_2 from Scheelite ($CaWO_4$) by Self-Propagating High-Temperature Synthesis (SHS) Process
Author Mr. Si Thu Myint Maung
Major Program Materials Engineering

Major Advisor

.....
 (Assoc. Prof. Dr. Sutham Niyomwas)

Examining Committee :

.....Chairperson
 (Asst. Prof. Dr. Vishnu Rachpech)

.....Committee
 (Assoc. Prof. Dr. Sutham Niyomwas)

Co-advisor

.....
 (Dr. Tawat Chanadee)

.....Committee
 (Dr. Tawat Chanadee)

.....Committee
 (Dr. Matthana Khanghamano)

.....Committee
 (Dr. Ruangdaj Tongstri)

The Graduate School, Prince of Songkla University, has approved this thesis as fulfillment of the requirements for the Master of Engineering Degree in Materials Engineering

.....
 (Prof. Dr. Damrongsak Faroongsarng)
 Dean of Graduate School

This is to certify that the work here submitted is the result of the candidate's own investigations. Due acknowledgement has been made of any assistance received.

.....Signature
(Assoc. Prof. Dr. Sutham Niyomwas)
Major Advisor

.....Signature
(Dr. Tawat Chanadee)
Co-advisor

.....Signature
(Si Thu Myint Maung)
Candidate

I hereby certify that this work has not been accepted in substance for any degree, and is not being currently submitted in candidature for any degree.

.....Signature
(Si Thu Myint Maung)
Candidate

Thesis Title	Synthesis of WSi_2 from Scheelite ($CaWO_4$) by Self-Propagating High-Temperature Synthesis (SHS) Process
Author	Mr. Si Thu Myint Maung
Major Program	Materials Engineering
Academic Year	2017

ABSTRACT

In this research work, tungsten silicide (WSi_2) intermetallic and tungsten silicide (WSi_2 - W_5Si_3) intermetallic alloy were prepared via self-propagating high-temperature synthesis (SHS) from two aluminothermic and magnesiothermic reactant systems. The equilibrium compositions of the reactions were calculated by standard Gibbs energy minimization. The phase separation with and without the sand mold to produce these materials was applied. The resulted products properties such as phase separation, density, and micro-hardness were examined. The phase constituents and microstructure morphologies of the products were characterized by X-ray diffraction (XRD) and scanning electron microscopy (SEM) with energy dispersive X-ray (EDX)-capability.

In the first part, tungsten silicide (WSi_2) intermetallic was prepared via SHS from two aluminothermic reactant systems using scheelite ($CaWO_4$ -Si-Al) and pure oxide (CaO - WO_3 -Si-Al). The effects of high-energy milling of reactants, for the duration of 0.5, 2, 4 and 8 hr, and the effects of sand mold on the result products were studied. According to the experimental results, intermetallic WSi_2 was successfully synthesized with both systems. Using pure oxide (CaO - WO_3 -Si-Al) reactant gave a higher yield of WSi_2 than that of scheelite mineral ($CaWO_4$ -Si-Al), and the yield can be optimized by increasing the proportion of Si in the ($CaWO_4$ -Si-Al) reactant system. Moreover, it was found that the use of a sand mold helped the phase separation of the oxide slag and its intermetallic.

The second part, tungsten silicide (WSi_2 - W_5Si_3) intermetallic alloy was synthesized using SHS from the magnesiothermic reaction. The raw materials used were WO_3 , Si, and Mg as fuel. The SHS process successfully synthesized with higher weight percentage and dense alloy product of the WSi_2 - W_5Si_3 intermetallic alloy. In

addition, the true density (ρ) of intermetallic alloy has 8.97 g/cm^3 which is 96.42% of the theoretical true density. Furthermore, it is important to notice that the magnesiothermic reaction can produce the dense and homogeneous distribution of WSi_2 and W_5Si_3 intermetallic alloy in the as-SHS product.

Acknowledgments

It has been a brilliant experience employing in the Ceramic and Composite Materials Engineering Research Group (CMERG), Center of Excellence in Materials Engineering (CEME) Group in the whole period of thesis research.

I would like to first thank my advisor Assoc. Prof. Dr. Sutham Niyomwas for giving me the opportunity to join his research group and helping me improve my research and experimentation skills. He has really been a motivation to me for this work and useful guidance on how to organize and inspire in real life as well.

I am grateful to my co-advisor Dr. Tawat Chanadee, for his kind help, advice, supervision, discussions, and explanations over the past two years. None of this research would have been possible without the masses of work and support done by him. He explained to me through every step of this process.

I would like to say very thankful to Dr. Matthana Khangkhamano, for her invaluable guidelines and discussions given throughout the whole period of making my research work. She was an extremely patient and kind mentor on both academic life and ordinary life.

Many thanks also to Asst. Prof. Dr. Vishnu Rachpech, for his kind and support. His cooperation is really greatly acknowledged.

I would also like to thank Dr. Ruangdaj Tongstri, for the suggestion of research, thesis draft and as an external examiner.

Special thanks to Dr. Saowanee Singsarothai for teaching me how to use the SHS reactor and explaining the background theory needed to accomplish the synthesis process. Her collaboration is helpful to continue my research work.

Thanks also to all teachers in Department of Mining and Materials Engineering for the kind and welcoming during the whole period of thesis work. I would also like to thank all staff and technician in our department office.

I would also like to express thanks to technician and staff in Scientific Equipment Center (SEC), for technical help and advice for characterization process.

I gratefully acknowledge to Thailand's Education Hub for Southern Region of ASEAN Countries Project Office of the Higher Education Commission (TEH-AC) for giving me a scholarship.

I also would like to acknowledge the financial support of this work from the Graduate School in Prince of Songkla University (PSU). I also sincere thanks to the Ceramic and Composite Materials Engineering Research Group (CMERG), Center of Excellence in Materials Engineering (CEME), Faculty of Engineering, Prince of Songkla University (PSU), Thailand.

I would thanks to my dear colleagues and my research group, for putting up with my fantastic hours while carrying out this work and for their caring and support.

Finally, I would especially like to thank my parents, brother and extended family for all the love, support, and encouragement.

Si Thu Myint Maung

Table of Contents

COVER	i
APPROVAL PAGE	ii
CERTIFICATION	iii
ABSTRACT	v
ACKNOWLEDGEMENT	vii
TABLE OF CONTENTS	ix
LIST OF TABLES	xiii
LIST OF FIGURES	xiv
CHAPTER 1. INTRODUCTION	1
1.1 Objectives	2
1.2 Benefits of Thesis	3
1.3 Outline	3
CHAPTER 2. LITERATURE REVIEW	4
2.1 Tungsten Alloy	4
2.2 Tungsten Silicide	5
2.3 Scheelite	7
2.4 Calcium Oxide	10
2.5 Combustion Synthesis	11
2.6 Self-Propagating High-Temperature Synthesis (SHS)	12
2.6.1 Thermodynamics	13
2.6.2 The Adiabatic Temperature (T _{ad})	14
2.6.3 Gibbs Energy of Formation	17
2.6.4 The effects of Parameters of the SHS Process	18
2.6.4.1 Particle Size	18
2.6.4.2 Inert Gas Pressure	19
2.6.4.3 Green Pellet Density and Diameter	19
2.6.5 The Mechanism of SHS	20
2.6.6 Applications of SHS	22
2.6.7 Advantages and Disadvantages of SHS Process	24

2.7	Related Literatures	26
2.7.1	Synthesis of Orthopedic Implant Materials via Combustion Synthesis	26
2.7.2	SHS-Casting of WSi_2 Intermetallic Compound	28
2.7.3	Investigation of Combustion Channel	30
2.8	Characterization Techniques	33
2.8.1	X-ray Diffraction	33
2.8.1.1	Basic Principles of XRD	34
2.8.1.2	Limitation of XRD	35
2.8.2	Scanning Electron Microscopy	36
2.8.2.1	Basic Principles of SEM	37
2.8.2.2	Limitation of SEM	39
2.8.3	X-ray Spectroscopy	40
2.8.3.1	X-ray Energy Dispersive Spectrometer	40
2.8.3.2	Basic Principle of EDS Analysis	42
2.8.4	X-ray Fluorescence Spectrometer	44
2.8.4.1	Basic Principle of XRF Analysis	44
2.8.5	Density Measurement	47
2.8.5.1	True Density	47
2.8.5.2	Bulk Density and Apparent Porosity	47
CHAPTER	3. RESEARCH METHODOLOGY	50
3.1	Raw Materials	50
3.2	Equipment and Tools	52
3.3	Experimental Procedure	53
3.3.1	Preliminary Synthesis of the Tungsten Silicide Intermetallic Alloy	53
3.3.1.1	$CaWO_4$ -Si-Al Reactant System	53
3.3.1.2	CaO- WO_3 -Si-Al Reactant System	54
3.3.1.3	WO_3 -Si-Mg Reactant System	55
3.4	Preparing the Green Pellet	56
3.5	Preparing the Graphite Mold	57

3.6	Preparing the Sand Mold	58
3.7	Synthesis of Tungsten Silicide Intermetallic without Sand Mold	59
3.7.1	A Study on the Influence of SHS on the Reduction of Heat Loss during the Shear Process	61
3.8	Synthesis of Tungsten Silicide Intermetallic with Sand Mold	62
3.9	Characterization Methods	62
3.9.1	X-ray Fluorescence Spectrometer	62
3.9.2	X-ray diffraction	62
3.9.3	Scanning Electron Microscope	62
3.10	Semi-quantitative Analysis Method	63
3.11	Density Testing Method	63
3.12	Microstructure Examination	63
3.13	Micro Hardness Testing	64
CHAPTER	4. RESULTS AND DISCUSSION	65
4.1	Two Reactant Systems for Self-Propagating High Temperature Synthesis of Tungsten Silicide	66
4.1.1	Particle Size of Reactants	66
4.1.2	Thermodynamic Analysis	66
4.1.2.1	Thermal Analysis for CaWO ₄ -Si-Al reactant System	67
4.1.2.2	Thermal Analysis for CaO-WO ₃ -Si-Al reactant System	69
4.1.3	Characterization of the Intermetallic Product	71
4.1.3.1	Characterization of the CaWO ₄ -Si-Al Reactant System	71
4.1.3.2	Characterization of the CaO-WO ₃ -Si-Al Reactant System	76
4.1.4	Mechanical Properties of the WSi ₂ Intermetallic	79
4.1.4.1	Combustion Front Velocity of the WSi ₂ Intermetallic	79
4.1.4.2	True Density of the WSi ₂ Intermetallic	80
4.1.4.3	Bulk Density of the WSi ₂ Intermetallic	81
4.1.4.4	Apparent Porosity of the WSi ₂ Intermetallic	82
4.1.4.5	Micro-Vickers Hardness of the WSi ₂ Intermetallic	83
4.1.5	Characterization of the Sand Mold and Oxide Slag	85
4.2	Synthesis of Tungsten Silicide Intermetallic Alloy by Magnesiothermic Reduction Reaction	89

4.2.1	Thermal Analysis	89
4.2.2	Intermetallic Product Characterization	90
CHAPTER	5. CONCLUSIONS AND SUGGESTIONS	97
5.1	Conclusions	97
5.2	Suggestions	98
REFERENCES		99
VITAE		109

Lists of Tables

Table 2.1.	Properties of tungsten silicide	5
Table 2.2.	General specifications of scheelite	8
Table 2.3.	General specifications of calcium oxide	11
Table 2.4.	Results of the calculated T_{ad} for some compounds	16
Table 2.5.	Some products that can be synthesized by SHS	23
Table 2.6.	The comparison of the WDXRF and EDXRF techniques	46
Table 3.1.	Chemical composition, particle size and sources of raw materials	50
Table 3.2.	List of chemicals used in the experiment	51
Table 3.3.	The list of equipment models and types for the experiment	52
Table 3.4.	The ratio of the reactants used in Eq. 3.1	53
Table 3.5.	The XRF result of scheelite ($CaWO_4$) minerals	54
Table 3.6.	The ratio of the reactants used in Eq. (3.2)	54
Table 3.7.	The ratio of the reactants used in Eq. (3.3)	55
Table 3.8.	The ratio of the reactants used in Eq. (3.4)	55
Table 3.9.	Properties of the milled reactant powders	56
Table 3.10.	XRF results of natural sand	58
Table 4.1.	Properties of the milled reactant powders	65
Table 4.2.	Semi-quantitative analysis results from XRD results of ($CaWO_4$ -Si-Al) reactant system with ($n = 0$) Si mole	72
Table 4.3	Semi-quantitative analysis results from XRD results of ($CaWO_4$ -Si-Al) reactant system with excess ($n = 0.5$) Si mole	74
Table 4.4.	Semi-quantitative analysis results from XRD results of (CaO - WO_3 -Si- Al) reactant system	78
Table 4.5.	Properties for $CaWO_4$ -Si-Al reactant systems	84
Table 4.6.	Properties for CaO - WO_3 -Si-Al reactant systems	85

Lists of Figures

Figure 2.1.	Applications of tungsten alloys	4
Figure 2.2.	Illustration of the $W\text{Si}_2$ crystal structure (C11b (tI6) crystal structure)	6
Figure 2.3.	Illustration of the $W_5\text{Si}_3$ crystal structure (tI32 (D8m)), α , β , γ , and δ represented the sub lattice	6
Figure 2.4.	Scheelite (CaWO_4) raw materials	9
Figure 2.5.	The illustration of the crystal structure of scheelite viewed along with the [010] direction: AO8 polyhedra are blue color and XO4 polyhedra are green color	9
Figure 2.6.	Calcium oxide (CaO) (a) powder and (b) crystal structure: oxygen atom represents a grey sphere and calcium atom represent a red sphere	10
Figure 2.7.	Combustion synthesis modes (a) SHS, and (b) VCS	12
Figure 2.8.	The relationship between temperature and time of SHS reaction	14
Figure 2.9.	Illustration of the relation of the adiabatic temperature on reactants and products	15
Figure 2.10.	The relationship between $(\Delta H^\circ_{298}/C_{p298})$ of some compounds and the adiabatic temperature	16
Figure 2.11.	Gibbs energy of formation for oxides	17
Figure 2.12.	Final sample density as a function of initial density for B- N_2 and Al- N_2 systems	18
Figure 2.13.	The relation of inert gas pressure and combustion wave velocity on some systems	19
Figure 2.14.	The relation of the pellet diameter and combustion temperature for various mixtures	20
Figure 2.15.	The digital photograph of the sample during combustion synthesis process	21
Figure 2.16.	The schematic of the phase separation steps, (a) reacting, (b) melting and (c) final product (with pores)	27
Figure 2.17.	The schematic of the phase separation steps, (a) reacting, (b) melting and (c) final product (with thin film Al_2O_3 tube)	27

Figure 2.18.	The influence of ambient gas pressure on alloy density and yield	27
Figure 2.19.	As-synthesized specimens and specimens prepared for hardness and tensile tests	28
Figure 2.20.	The illustration of the occurrences of the product during in-situ SHS-casting reaction	29
Figure 2.21.	The macro and microstructure of the as-SHS product	29
Figure 2.22.	XRD pattern of (a) intermetallic WSi_2 , (b) oxide slag ($Al_2O_3-WSi_2$) and (c) EDX analysis of WSi_2	30
Figure 2.23.	The effects of the synthesis parameters on the combustion channel width	31
Figure 2.24.	The effect of cold compaction pressure on the NiTi alloys produced at 250 °C preheating temperature and 60 °C/min heating rate, (a) 50 MPa, (b) 75 MPa, and (c) 100 MPa	31
Figure 2.25.	The effect of preheating temperature on the NiTi alloys produced at 50 MPa pressure, 60 °C/min heating rate, (a) 50 MPa, (b) 75 MPa, and (c) 100 MPa	32
Figure 2.26.	The principle of schematic stretching X-Ray diffraction	34
Figure 2.27.	Schematics of the cross-section of the laboratory X-ray tubes	35
Figure 2.28.	Photograph of (a) the powder X-ray diffractometer, and (b) the main components of the X-ray diffractometer assembly	36
Figure 2.29.	Schematic of the major components of a typical scanning electron microscope	37
Figure 2.30.	Types of signals generated by the collision of electrons with a specimen	38
Figure 2.31.	SEM images of triangular precipitates at SnMnNBo sample (a) SE image, and (b) BSE image	39
Figure 2.32.	A photograph of (a) the scanning electron microscopy, and (b) specimen holder and the vacuum chamber (SEM, Quanta 400, FEI, USA)	40
Figure 2.33.	The typical schematic of an Energy Dispersive Spectrometer	41
Figure 2.34.	Illustration of the atomic model of the characteristic X-ray production	42
Figure 2.35.	A schematic diagram of electron-matter interactions for SEM	42

- Figure 2.36.** The elemental compositions analysis of (a) Mapping analysis of carbon, tungsten, cobalt, and titanium of the sinter obtained from a powder mixture of WC-Co +1wt.% TiC, SEM, EDS , and (b,c) localized elemental information of series of spots and generated spectra, Adopted from 43
- Figure 2.37.** Illustration of the generation of X-ray fluorescence radiation in the atomic model 45
- Figure 2.38.** The difference X-ray detection systems in (a) WDXRF, and (b) EDXRF 45
- Figure 2.39.** A photograph of X-ray fluorescence spectrometer (XRF, PANalytical, Zetium, UK) 46
- Figure 3.1.** Morphologies of the reactant powders used in the experiment (a) CaWO_4 , (b) WO_3 , (c) CaO , (d) Si, (e) Al and (f) Mg 51
- Figure 3.2.** Digital photographs of green pellet sample before SHS (a) side view and (b) top view 56
- Figure 3.3.** Digital photograph of the design of graphite molds used in experiment (a), piece 1 (b), piece 2, (c) piece 3, (d) the stacked condition of all pieces, and an illustration of a cross-section of (d) 57
- Figure 3.4.** Vibratory sieve shaker 58
- Figure 3.5.** Hollow sand mold after firing at 200 °C for 24 hours 59
- Figure 3.6.** Preparing of the sample on top of stacked graphite plates without sand mold (a) digital photograph, and (b) illustration of a cross-section of (a) 60
- Figure 3.7.** A schematic of the experimental setup without sand mold 60
- Figure 3.8.** Preparing of the sample on top of stacked graphite plates with sand mold (a) digital photograph, and (b) illustration of a cross-section of (a) 61
- Figure 3.9.** A schematic of the experimental setup with sand mold 62
- Figure 4.1.** Equilibrium compositions of CaWO_4 -Si-Al reactant systems in inert Ar atmosphere 68
- Figure 4.2.** The relation between temperature and Gibbs energy of reactions under Argon gas atmosphere for CaWO_4 -Si-Al reactant system at a temperature range from 0 to 3500 °C 68
- Figure 4.3.** Equilibrium compositions of CaO - WO_3 -Si-Al reactant systems in inert Ar atmosphere 70

- Figure 4.4.** The relation between temperature and Gibbs energy of reactions under Argon gas atmosphere for CaO-WO₃-Si-Al reactant system at a temperature range from 0 to 3500 °C 70
- Figure 4.5.** XRD patterns of WSi₂ intermetallic products from CaWO₄-Si-Al reactant system obtained with the milling times (a) 0.5, (b) 2, (c) 4, and (d) 8 hr 72
- Figure 4.6.** XRD patterns of WSi₂ intermetallic products from CaWO₄-Si-Al reactant system with (n=0.5) moles Si obtained with the milling times (a) 0.5, (b) 2, (c) 4, and (d) 8 hr 73
- Figure 4.7.** SEM microphotographs of WSi₂ intermetallic products from CaWO₄-Si-Al reactant system obtained with the milling times (a) 0.5, (b) 2, (c) 4, and (d) 8 hr 74
- Figure 4.8.** EDX analysis of WSi₂ intermetallic products from CaWO₄-Si-Al reactant system obtained with the milling times (a) 0.5, (b) 2, (c) 4, and (d) 8 hr 75
- Figure 4.9.** XRD patterns of WSi₂ intermetallic products from CaO-WO₃-Si-Al reactant system obtained with the milling times (a) 0.5, (b) 2, (c) 4, and (d) 8 hr 77
- Figure 4.10.** SEM microphotographs of WSi₂ intermetallic products from CaO-WO₃-Si-Al reactant system obtained with the milling times (a) 0.5, (b) 2, (c) 4, and (d) 8 hr 78
- Figure 4.11.** The effect of high energy milling time on the combustion wave velocity of the green pellet (a) CaWO₄-Si-Al reactant system, and (b) CaO-WO₃-Si-Al reactant system 79
- Figure 4.12.** The effect of high energy milling time on the true density of the WSi₂ intermetallic (a) CaWO₄-Si-Al reactant system, and (b) CaO-WO₃-Si-Al reactant system 80
- Figure 4.13.** The effect of high energy milling time on the bulk density of the WSi₂ intermetallic (a) CaWO₄-Si-Al reactant system, and (b) CaO-WO₃-Si-Al reactant system 81
- Figure 4.14.** The effect of high energy milling time on the apparent porosity percentage of the WSi₂ intermetallic (a) CaWO₄-Si-Al reactant system, and (b) CaO-WO₃-Si-Al reactant system 82

- Figure 4.15.** The effect of high energy milling time on micro-Vicker hardness values of the WSi_2 intermetallic (a) $CaWO_4$ -Si-Al reactant system (2+0) mole Si, and (b) (2+0.5) mole Si, and (c) CaO - WO_3 -Si-Al reactant system 83
- Figure 4.16.** The stages in SHS-reaction based processing of a reactant: (a) with prepared reagent pellet, (b) ignition, and (c) showing the phase formed between oxide slag and sand mold 86
- Figure 4.17.** The digital photograph of the sand mold after SHS-reaction (a) showing the oxide slag trapped on the sand mold wall, and (b) cross-section view of the sand mold 86
- Figure 4.18.** XRD results between sand mold wall and oxide slag (a) 3 mm and (b) 2 mm from the mold wall. The insert shows a cross-section of the sand mold 87
- Figure 4.19.** EDX analysis of select cross-section points including the sand mold wall: points (a) 1, (b) 2, (c) 3, (d) 4, and (e) 5 88
- Figure 4.20.** Equilibrium composition of WO_3 -Si-Mg reactant system in Argon gas atmosphere 90
- Figure 4.21.** As-synthesized SHS-product (a) Digital photograph and (b) illustration of combustion wave travel and phase separation during combustion 90
- Figure 4.22.** Micro hardness values spreading for ten points on the surface of the intermetallic alloy 91
- Figure 4.23.** XRD results of SHS product of (a) intermetallic alloy and (b) oxide slag 92
- Figure 4.24.** SEM microphotograph of the as-SHS crack surface of intermetallic alloy (a) SE and (b) BSE images (WSi_2 dark gray, W_5Si_3 light gray) 93
- Figure 4.25.** SEM secondary electron images of the as-SHS crack surface of oxide slag (a) Mg_2SiO_4 area (dark gray) and (b) WSi_2 - W_5Si_3 area (light gray) 93
- Figure 4.26.** EDX point analysis of as-SHS cross-section of intermetallic alloy (a) WSi_2 dark gray phase and (b) W_5Si_3 light gray phase area 94
- Figure 4.27.** EDX point analysis of the as-SHS crack surface of oxide slag (a) Mg_2SiO_4 dark gray background and (b) WSi_2 - W_5Si_3 light gray particles area 95

Chapter 1

Introduction

The transition metals of many silicides were attracted to elevated temperature structural applications due to their high thermal stability. In addition, their high oxidation resistance in oxidizing environments has been mentioned as a main attractive characteristic. Moreover, intermetallic alloys based on the silicide of tungsten, and their second phases (e.g. WSi_2 , $\text{WSi}_2\text{-W}_5\text{Si}_3$, $\text{WSi}_2\text{-ZrO}_2$, $\text{WSi}_2\text{-MoSi}_2\text{-SiC}$, etc.), have wide applications due to their unique properties, such as excellent oxidation and corrosion resistance, high melting point, high density and hardness, and good mechanical and microstructural stability from room temperature to service temperatures [1-4]. The low electrical resistivity of silicides together with high thermal stability, electromigration resistance, and excellent diffusion barrier characteristics are significant in many areas of electronic and microelectronic fields [5].

Usually, tungsten silicide prepared in a multiple-steps such as the reaction of W and Si at high temperature and followed by milling to form a powder and then pressed by sintering to form solid [6]. In addition, thermal plasma synthesis, chemical vapor deposition (CVD), high-temperature sintering and hot-isostatic pressing techniques can achieve the high-purity and full-density of WSi_2 intermetallic. However, the exceedingly high melting point of tungsten silicide needs long exposures at high temperatures to make WSi_2 and W_5Si_3 intermetallics and some techniques need ultra-high purity gases and expensive reactants, which in turn increases the costs [7, 8].

Nowadays, improvement of energy-saving and effective technologies is of great importance for scientists and researchers. SHS is technically simple, economically attractive and potentially energy-efficient process to produce ceramic matrix composites, in situ refractory ceramics, nanophase materials, and intermetallic alloys. During SHS process, the sample heats locally by an exterior heat source and the heat liberates self-sustaining solid-flame combustion which generates the required heat for the propagation of the whole sample over a short period of time [9-12]. The simplicity, energy savings and economic benefits of this process are widely acknowledged. The

SHS process is considered a cost-saving method to synthesize WSi_2 , with a low-cost reactor and lower supplies for a power source [13-15].

In recent times, a new method to the SHS-casting, reactive casting of bulk ceramic materials or melt-casting has been reported. In this approach, exothermic reactions are applied to attain high temperatures for melting the products. An example, cast $Fe_3Al-Fe_3AlC_{0.5}$ composites [16], molybdenum [17], niobium [18], tungsten silicide (WSi_2) [19] and Si and SiC [12] were prepared using an SHS-casting. It was reported that the synthesis of WSi_2 -SiC composite employed alternative activating additives, such as magnesium–Teflon mixture [20]. In their early studies, the authors T. Chanadee and S. Niyomwas [19] described the formation of tungsten intermetallic compounds (WSi_2 , W_2B) by SHS. The same authors described the phase separation of the oxide ceramic and intermetallic compounds using quartz tube mold, and effects of Ar pressure assist high densification combustion synthesis [21]. P. Pujalte et al. [22] also synthesized (WSi_2 , W_5Si_3)-SiC composite by the reaction between WC and Si.

In this study, tungsten silicide intermetallic was synthesized by SHS from two alternative reactant powders, namely from scheelite mineral ($CaWO_4$) and from pure oxide ($CaO-WO_3$) reacted with Si and Al. The aim of this study is concerned with the thermodynamic modeling of the aluminothermic and magnesiothermic reduction of W from WO_3 and follow the reaction with Si. This was done to determine the equilibrium temperature and compositions of the reaction products under the adiabatic condition as functions of the composition and initial temperature of raw materials. Moreover, the phase composition, microstructure, density and micro-hardness of SHS products fabricated by this process were also characterized. This will be the preliminary guide for the production of the tungsten-based intermetallic compound using SHS-casting process and the usefulness of tungsten silicide for many applications in the further study.

1.1 Objectives

The main objective of this study is to characterize and to investigate the WSi_2 intermetallic compound by SHS process. The research work aims to fulfill the following specific objectives:

- 1) The result should produce the WSi_2 intermetallic alloy from the reactants

system of $\text{CaWO}_4\text{-Si-Al}$ and $\text{CaO-WO}_3\text{-Si-Al}$.

- 2) Comparison of purity of as-SHS WSi_2 intermetallic from the two alternative raw materials of $\text{CaWO}_4\text{-Si-Al}$ and $\text{CaO-WO}_3\text{-Si-Al}$.
- 3) To determine the optimal combustion synthesis conditions for high yield of dense WSi_2 intermetallic by control of Si proportion in the reactant system
- 4) To investigate the effects of sand mold on phase separation of the oxide slag.
- 5) To synthesize the $(\text{WSi}_2\text{-W}_5\text{Si}_3)$ intermetallic alloy by the magnesiothermic reduction reaction.

1.2 Benefits of Thesis

The main benefits of this research are the usefulness of SHS process to produce the high purity and dense intermetallic alloy. This process is the best way to energy saving, low-cost operation, can minimize the production time and can be produced by tungsten silicide intermetallic alloys. This can reduce the high payment for reactant pure material tungsten oxide by substitute using the scheelite minerals and calcium oxide.

1.3 Outline

The thesis is divided into five chapters which are explained as follows:

Chapter one is explained in the introduction of the thesis, including the brief history of the materials and synthesis methods, the objectives and benefits of the research.

Chapter two is a comprehensive literature review focused mainly on the tungsten silicide intermetallic alloys and the SHS method.

Chapter three is the research methodology and facilities used for synthesis and characterization of the intermetallic alloys.

Chapter four represent the experimental results obtained from the synthesis of W-Si based intermetallic alloys and the mechanical properties of each product, respectively, as well as the discussions on the results gained and the phase separation mechanisms between the sand mold and as-SHS products.

Chapter five is the final conclusions and suggestions for future works.

Chapter 2

Literature Review

2.1 Tungsten Alloy

Tungsten alloys or tungsten composite have established considerable consideration for many applications such as radiation shields, electrical contacts, core materials of the kinetic-energy penetrator and counter weights because of their high strength, density, and ductility [23]. High melting point (3410 °C) of Tungsten (W) attracted for many high-temperature applications. Therefore, W is an obvious choice for structural applications exposed to very high temperature. Moreover, the silicide of tungsten-based alloys have a widespread application as materials for current technical use due to their unique belongings such as chemical inertness, high hardness, electronic conductivity,, thermal shock and corrosion resistance at high temperature, and have potentially industrial applications such as abrasive media, turbine blades, the nozzle of a gas burner, electrode materials and thin film of electronic components, which are exposed to accurate environments [24]. Some applications of tungsten alloys are shown in Figure 2.1.



Figure 2.1. Applications of tungsten alloys [25].

2.2 Tungsten Silicide

There are two types of tungsten silicide such as tungsten disilicide (WSi_2) and pentatungsten trisilicide (W_5Si_3). They are an inorganic compound and a silicide of tungsten. Tungsten silicide is a ceramic material and also electrically conductive materials. Tungsten silicide is also used in many microelectronic applications. They are stable from room temperature to 900 °C under normal atmosphere [26].

Table 2.1. Properties of tungsten silicide [25-28].

Properties	Tungsten Disilicide	Pentatungsten Trisilicide
Chemical Formula	WSi_2	W_5Si_3
Theoretical Analysis	78.2% W – 22.8% Si	90.77% W - 9.23% Si
Density (g/cm ³)	9.3 (measured) 9.75 (by X-ray)	12.2 (measured) 14.56 (by X-ray)
Melting Point (°C)	2165	2370
Crystal Structure	Tetragonal (C_{11b}), $MoSi_2$ type, D_{4h}^{17} space group	Tetragonal (D_{8m}), Cr_3B_2 type, D_{4h}^{18} space group
Lattice constant (Å)	a= 3.211 c= 7.868	a= 9.601 c= 4.972
Hardness (Vicker) (kg/mm ²)	1090 (100g, ceramic)	-
Hardness (Knoop) (kg/mm ²)	1090 (100g, ceramic)	770
Electrical Resistivity ($\mu\Omega$.cm)	30-70	-
Superconductive (°K)	<1.2 <1.9	2.84
$-\Delta H^\circ_{298}$ (KJ/mol)	92	125
Heat Capacity (J/kg/K)	33440 (425-1450 °C)	-
Appearance	blue-gray, metallic	-
Solubility in Water	insoluble	insoluble

Tungsten silicide combined with molybdenum silicide is used for a high-temperature thermocouple in atmospheric condition. Moreover, tungsten silicide is insoluble in water but will be attacked with chlorine, fluorine, and alkali, etc. Some properties of tungsten disilicide and pentatungsten trisilicide are listed in Table 2.1. Example of crystal structures for WSi_2 and W_5Si_3 phases are shown in Figure 2.2 and 2.3 [29, 30].

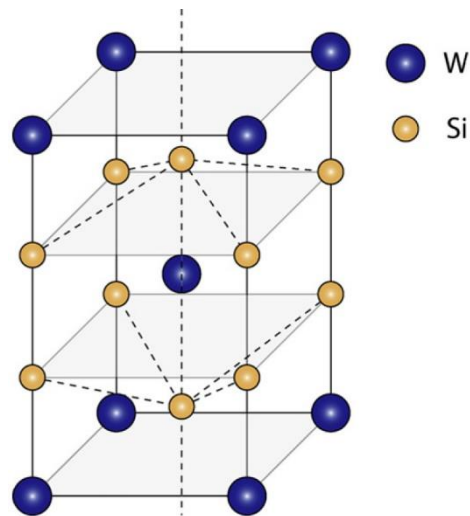


Figure 2.2. Illustration of the WSi_2 crystal structure (C11b (tI6) crystal structure) [1].

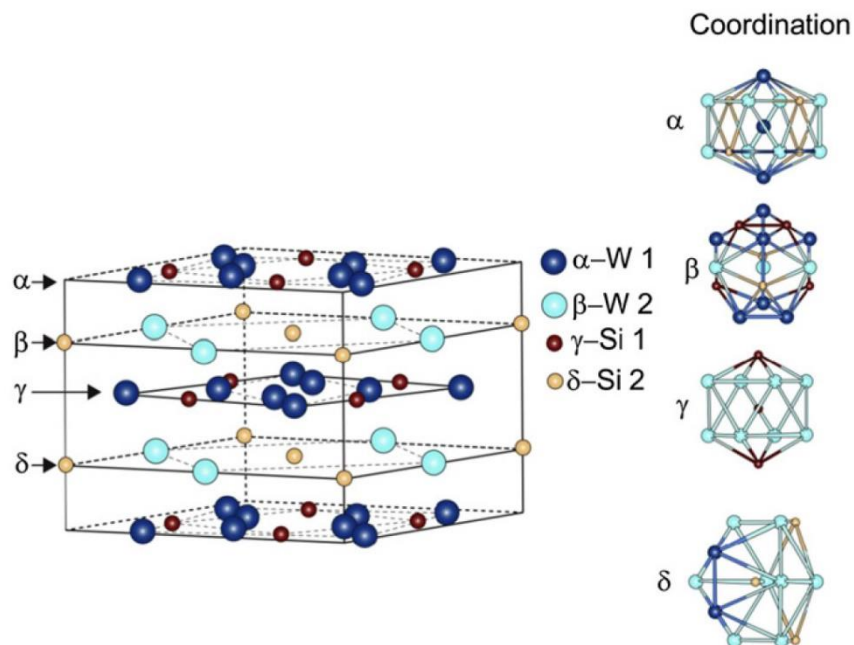


Figure 2.3. Illustration of the W_5Si_3 crystal structure (tI32 (D8m)), α , β , γ , and δ represented the sub lattice [29].

Tungsten silicide can be produced by reacting of reactant powders under argon or nitrogen atmosphere. The use of the starting raw materials, size, reaction temperature, reaction process, crystallinity, present of defects, and experimental conditions determine the reaction product, mechanism, and kinetics. Usually, dense tungsten silicide prepared in multiple-steps such as the reaction of W and Si at high temperature and followed by milling to form a powder and then pressed by sintering to form solid [31, 32]. Tungsten silicide can be prepared from a variety of approaches, such as the reaction between W and Si at high temperature, mechanical alloying, chemical vaporization, (co-evaporation) between the vapor of W and the vapor of Si, co-sputtering between W and Si, a sputtering target made from WSi_2 , and ion beam synthesis.

In addition, carbothermal reduction method, thermal plasma synthesis, chemical vapor deposition (CVD), high-temperature sintering and hot-isostatic pressing (HIP) techniques can achieve the high-purity and full-density of WSi_2 intermetallic [33-37]. However, the extremely high melting point of tungsten silicide requires long exposures at high temperatures to make WSi_2 and W_5Si_3 intermetallic and also some techniques need ultra-high purity gases and expensive reactants, which in turn increases the costs.

2.3 Scheelite

Scheelite is a calcium tungstate mineral with the chemical formula $CaWO_4$. It is an important ore of tungsten. Karl Caesar von Leonhard named Scheelite on 1821 in honor of Carl Wilhelm Scheele (9 December 1742–21 May 1786). Carl Wilhelm Scheele is a chemist and commercial apothecary. Carl Wilhelm Scheele discovered and identified many elements such as tungsten, molybdenum, hydrogen, chlorine (before Humphry Davy) and barium, among others. He examined many vitally important organic compounds. He verified the being of tungstic oxide in the mineral [38].

A fluoroscope with a calcium tungstate-coated screen was invented by Thomas Edison, which made the images six times brighter than those with barium platinocyanide. Scheelite was also used in radium paint, it is almost the same manner as zinc sulfide. Scheelite ($CaWO_4$) mineral is insoluble in acids and soluble in alkalis. The bluish-white to yellow and bright blue fluorescent can examine under short-wave

UV light. Occasionally, scheelite is connected with native gold ore, its fluorescence property is advantageous for geologists for gold deposits searching. Scheelite is having highly transparency ranges and also their crystal faces are highly lustrous. Scheelite generally occurs in tin-bearing veins and is sometimes found in association with gold. Some properties of scheelite is listed in Table 2.2. Natural material is very seldom without internal growth features and inclusions (imperfections), while the synthetic material is usually very clean [39].

Table 2.2. General specifications of scheelite [38-44].

Specifications	Scheelite
Type	Mineral
Chemical Formula	CaWO_4
Lattice Parameters	$a=5.242 \text{ \AA}$ $c=11.373 \text{ \AA}$
Crystal Structure	tetragonal
Crystal Class	dipyramidal pseudo-octahedra
Appearances (Color)	Tan, golden-yellow, pinkish to reddish gray, colorless, white, orange, greenish, dark brown, etc.; colorless in transmitted light
Hardness (Mohs)	4.5 to 5
Specific Density (g/cm^3)	5.9 to 6.1
Bulk Density (gm/cc) (Electron Density)	5.26



Figure 2.4. Scheelite (CaWO_4) raw materials [43].

Figure 2.4 represents photos of scheelite raw materials. The crystal structure of scheelite has been widely studied in the earlier years. The basic accurate crystal structure of scheelite is AXO_4 structure and it can be seen in Figure 2. 5. This structure contains the edge-sharing AO_8 polyhedra which are interconnected with XO_4 tetrahedra by the common apex. Eight and four oxygen ions surround A and X cation, respectively, while two A and one X cation surround each oxygen ion. Normally, X is represented as a W, Mo or V, and A is denoted as an alkaline-earth, alkaline or rare earth [45-47]. In this research work, the minerals of scheelite raw material, from Chiang Mai Mining Co., Ltd., Thailand, is used as reactant material.

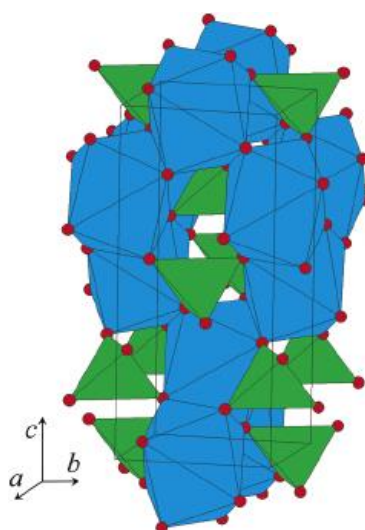


Figure 2.5. The illustration of the crystal structure of scheelite viewed along with the $[010]$ direction: AO_8 polyhedra are blue color and XO_4 polyhedra are green color [45].

2.4 Calcium Oxide

Calcium oxide (CaO), a white crystalline solid chemical compound, is commonly known as lime (quicklime). It is used for many applications. Calcium oxide can be mass-produced thermal decomposition of materials from limestone, seashells, coral, or chalk, that have calcium carbonate (CaCO_3 ; mineral calcite), in a lime kiln. Normally, calcium oxide is a white, alkaline, caustic, and crystalline solid at room temperature. The main widely use of quicklime is in the steelmaking process. The quicklime nullifies some oxides such as Al_2O_3 , SiO_2 , Fe_2O_3 , and acidic oxides to yield a basic molten slag.

Calcium oxide can generate high exothermic energy during SHS as well and also it is used for many SHS processes to start the ignition. Calcium oxide also releases thermal energy about ($\Delta H_f = -63.7 \text{ kJ/mol}$), by the formation of the hydrate and calcium hydrate during mix with water. This hydrate gives the exothermic reaction and the solid wisps up. If the hydration reaction is reversed, the hydrate can be retransformed to quicklime by removing the water by heating it. A convenient portable source of heat obtained by this process can be used to warm the food as a self-heating can, and heating water without open flames, respectively [48-51]. The image of powder CaO and crystal structure are shown in Figure 2.6. Some properties of CaO is listed in Table 2.3.

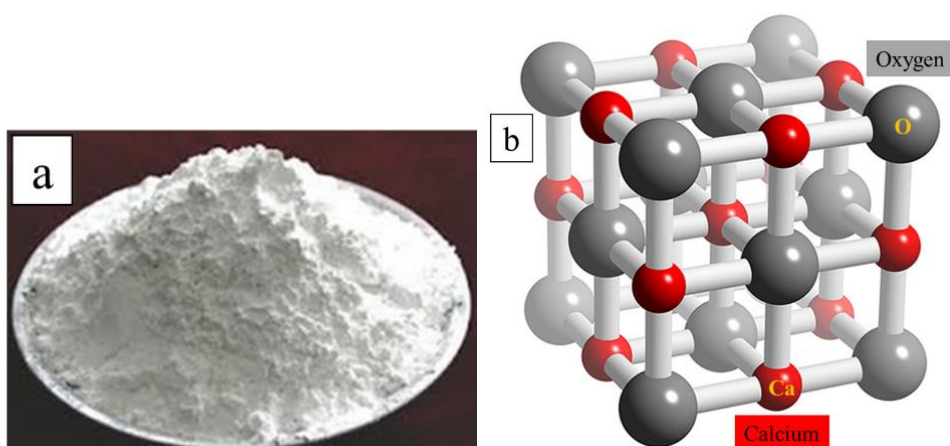


Figure 2.6. Calcium oxide (CaO) (a) powder [51] and (b) crystal structure: oxygen atom represents a grey sphere and calcium atom represent a red sphere [58].

Table 2.3. General specifications of calcium oxide [49-53].

Specifications	Calcium Oxide
Chemical Formula	CaO
Molar Mass (g/mol)	56.08
Standard molar entropy (S°_{298}) (J/mol/K)	40
Standard enthalpy of formation ($\Delta H_f^{\circ}_{298}$) (kJ/mol)	-635
Melting Point ($^{\circ}\text{C}$)	2613
Boiling Point ($^{\circ}\text{C}$)	3850
Density (g/cm ³)	3.34
Crystal structure	Cubic- cF8
Appearance	White, brown, pale yellow powder

2.5 Combustion Synthesis

Combustion synthesis (CS) is an exothermic reaction between an element and a compound. This method is used to synthesize many kinds of materials such as powders and near-net shape products of ceramics, metal compound, intermetallic, and composites. This method was first proposed by Merzhanov et al. [54] in 1971, a physicist and professor from the Soviet Union. The term ‘combustion’ includes flaming (gas-phase), smoldering (heterogeneous), and explosive reactions. It has two modes in combustion synthesis which are self-propagating high-temperature synthesis (SHS) and volume combustion synthesis (VCS). The illustration of two methods is shown in Figure 2.7.

In both methods, reactants need to be pressed into a cylindrical in form shape. The samples are then heated by an external source (e.g., tungsten coil, laser) to initiate an exothermic reaction for both locally SHS and uniformly VCS.

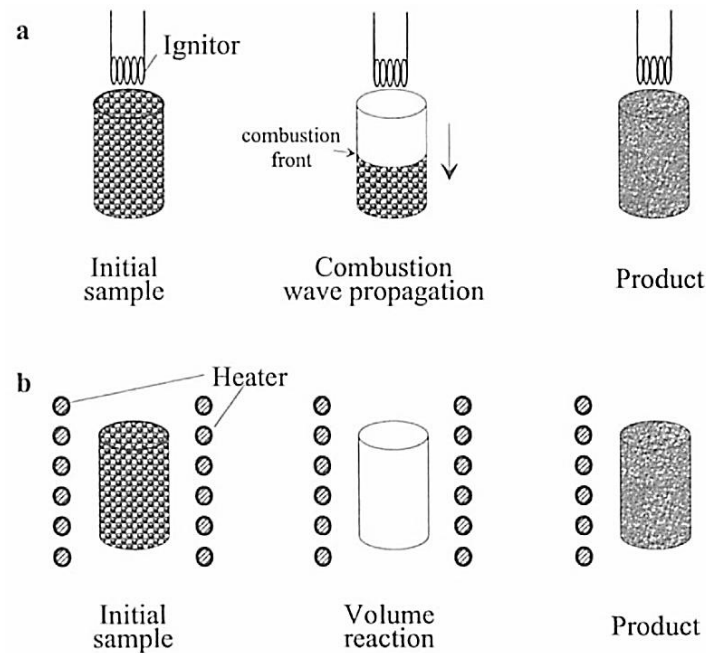


Figure 2.7. Combustion synthesis modes (a) SHS, and (b) VCS [54].

2.6 Self-Propagating High-Temperature Synthesis (SHS)

SHS is also known as fire or furnace less synthesis. The new scientific approach of SHS was advanced at the interface of three scientific fields: combustion, materials science, and high-temperature inorganic chemistry. SHS has been proved to produce a wide variety of advanced materials-nonoxide (e.g. silicides, borides, carbides, etc.) and oxide (semiconducting, refractory oxides, dielectric, magnetic, insulators, catalysts, sensors, etc.) materials. In various circumstances, these novel materials have very unique physical, chemical, and mechanical properties [55].

SHS is an autowave process similar to propagate of the combustion wave with the chemical reaction being localized in the combustion zone. And it can be propagated spontaneously along the chemically active medium. The nature of this method is the development of strongly exothermic reactions along the sample which generating high temperatures as a result of self-propagating of the sample. Because SHS is a highly exothermic reaction, it has a high activation energy that can generate heat from the reaction to produce a high amount of combustion. When the reaction is initiated by

rapid energy input the heat released from the reaction is sufficient to allow the reaction to continue. Normally, the synthesis conditions are as follow;

Temperature-up to 4000 °C,

Temperature growth rate – 10^3 - 10^6 K/s, and

The combustion velocity – 0.1-10 cm/s.

For any reaction system, the chemical and phase composition of the final product is governed by the green mixture composition and particle size, reactive volume, gas pressure, and initial temperature [56].

2.6.1 Thermodynamics

SHS is related to the enthalpy variation, between the reactants and products, during combustion synthesis. There are four important temperatures for SHS process and it can be expressed as follows;

(1) Initial temperature (T_0); the whole reactant sample temperature before the ignition takes place.

(2) Ignition temperature (T_{ig}); typically, the reaction initiated temperature is dependent on the kinetic characteristics (e.g. solid-solid, solid-gas, solid-liquid or liquid-gas) of a reaction.

(3) Adiabatic temperature (T_{ad}); T_{ad} is the maximum temperature obtained by adiabatic conditions. Normally, T_{ad} is associated with thermodynamics (exothermicity of the reactants) and the initial temperature of the reactants.

(4) Actual combustion temperature (T_c); T_c is the maximum temperature obtained by non-adiabatic conditions. T_c is kinetically measured then it will be dependent on heat reduces from the reaction front.

Usually, SHS reaction can measure by the three important temperatures (T_0 , T_{ig} , and T_c). Moreover, the adiabatic temperature (T_{ad}) can be calculated using thermodynamic calculation [57].

SHS starts at the initial temperature T_0 . The feed is heated rapidly to the ignition temperature (T_{ig}), which is where the reaction does not need more energy, but the kinetics of the reaction are greatly increased. The maximum temperature of the theoretical reaction or T_{ad} occurs under the assumption of no heat loss of the reaction

to the environment. In fact, the maximum temperature (T_c) is lower than the calculated adiabatic temperature for every reaction. Typically, the preparation of the compressive powder of the substrate is done under a temperature below the maximum temperature as shown in Figure 2.8.

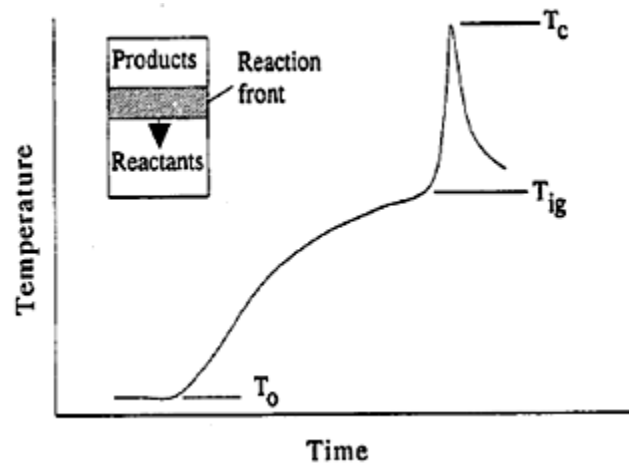


Figure 2.8. The relationship between temperature and time of SHS reaction [57].

2.6.2 The Adiabatic Temperature (T_{ad})

The adiabatic temperature is an important parameter for SHS process. The reaction occurs rapidly in seconds, in the same state as the adiabatic reaction. The energy released by the exothermic reaction is used to heat the sample without loss to the environment. Based on research and experiments, it was found that T_{ad} is the temperature obtained by measuring the heat of the exothermic reaction and determines the maximum temperature of the combustion system. It is known that if the T_{ad} is less than 1200 °C, it will not ignite and if T_{ad} is above 1800 °C, it will ignite by itself. When the calculated T_{ad} is between 1200-1800 °C, if the combustion reaction cannot be performed, preheat of the compact will be needed for self-propagating [58, 59].

Therefore, the adiabatic temperature of the reactant generated for SHS process must be higher than the theoretically self-propagate temperature. However, T_{ad} for SHS reactions is lower than those of the analyzed temperature sometimes because the heat available along the sample will be reduced when the reaction heat up the surface layer. Thus, the adiabatic temperature with zero heat losses is assumed for adiabatic

conditions, the heat of formation increases the temperature, of the pellet. The adiabatic temperature can be calculated by simple thermodynamics analysis. The results can be known that the maximum temperature of the reactants reached during an actual reaction [60].

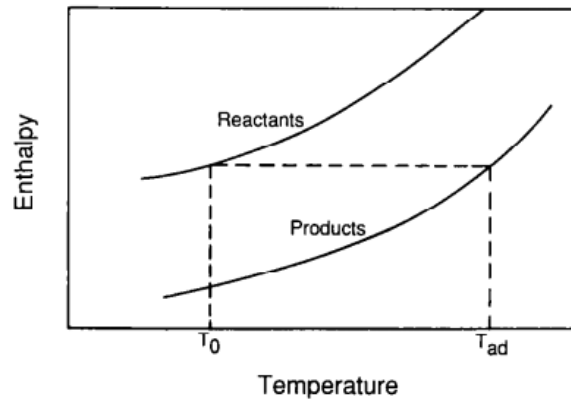


Figure 2.9. Illustration of the relation of the adiabatic temperature on reactants and products [61].

For example, the reactant metal (M) and non-metal (N) propose to synthesize a new solid product. The reaction can be written as,



The adiabatic temperature (T_{ad}) can be calculated from the following Eq 2.2.

$$\Delta H_{T_0}^0 = \int_{T_0}^{T_{ad}} C_p (MN) dT \quad (2.2)$$

Here, the enthalpy of the product MN formation at T_0 is ΔH and the solid matrix molar heat capacity is $C_p (MN)$. The schematic illustration of the relation of T_{ad} is shown in Figure 2.9, the two lines represented as reactants and products. Figure 2.9 shows the value of T_{ad} which is related with the temperature of the calculated heat of formation, i.e. T_0 . Typically, T_{ad} is presented on the basis of $T_0 = 298$ K. It has been proved that ratio of the heat capacity and the heat formation of the product at 298 K showed a roughly linear functionality of T_{ad} . Figure 2.10 shows the relationship

between some compounds and T_{ad} . Table 2.4 shows results of the calculated T_{ad} for some compounds based on the assumption of $T_0 = 298$ K.

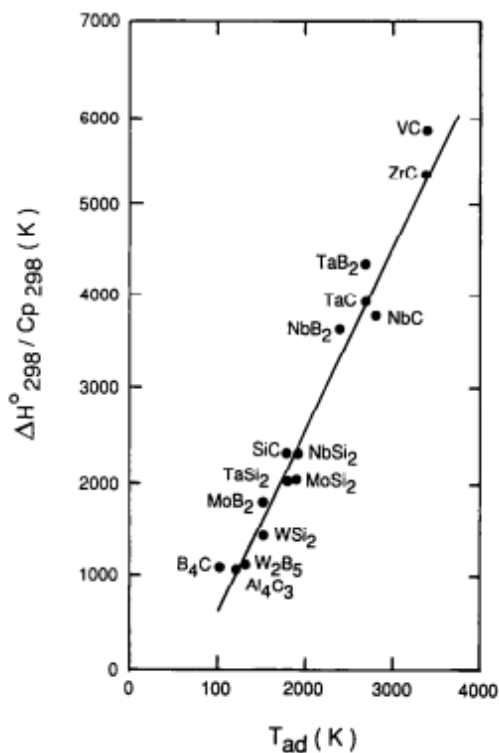


Figure 2.10. The relationship between $(\Delta H^{\circ}_{298}/C_{p298})$ of some compounds and the adiabatic temperature [62].

Table 2.4. Results of the calculated T_{ad} for some compounds [61-64].

Compounds	Adiabatic Temperature (T_{ad}) (K)	Compounds	Adiabatic Temperature (T_{ad}) (K)
SiC	1800	BN	3700
TiC	3210	MnS	3000
B ₄ C	1000	TaB ₂	3370
ZrB ₂	3310	NbB ₂	2400
TiN	4900	TiB ₂	3190
Ti ₅ Si ₃	2500	HfN	5100
MoSi ₂	1900	HfC	3900

2.6.3 Gibbs Energy of Formation

Gibbs energy of formation is a function of temperature for the group of reducing metals (Al, Mg, Ca, Zr, Zn, Ti, C, and H₂) as shown in Figure 2.11. Every metal precursor gives the Gibbs energy of negative oxides at every temperature range. Metal acts as a deformation agent better than non-metal and has the tendency of being able to decrease as the temperature rises. The calcium and magnesium will give Gibbs energy of low oxide formation at low temperature and boiling temperature and volatile at 1 atm pressure of 1090 °C and 1484 °C, respectively. The aluminum and zirconium are classified as popular aliquots, but aluminum is more popular because it is easier to find and less expensive [65-67].

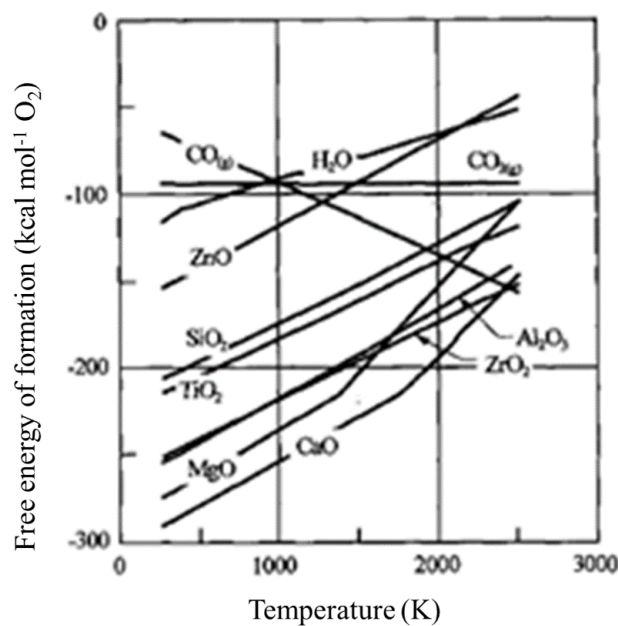


Figure 2.11. Gibbs energy of formation for oxides [68].

For any kinds of application, considering CS as a technique to synthesize materials, the final stage of the system or the maximum combustion temperature of the system performs an important part in considering the properties and microstructure of the products. Low combustion temperature may tend to an incomplete reaction, therefore, resulting in complex products. High combustion temperature may tend to a liquid product producing heterogeneous coarse microstructure, shape change, and large

shrinkage holes. In contrast, high combustion temperature and complete melting of a synthesized product may be required for e.g. joining or coating applications [67-69].

Additionally, the investigation of the propagation manner of the SHS reaction for a reaction system is important as it can as well affect the microstructure of the final product, and therefore its properties.

2.6.4 The effects of Parameters of the SHS Process

There are many parameters these can improve the SHS process. By investigating the effect of some reaction parameters can be improved the optimum condition of the synthesis reaction, and hence product.

2.6.4.1 Particle Size

The function of the reactant particle size is related to the combustion velocity, combustion temperature, thermal conductivity of the reactants and the products. Some investigations have shown that the particle size (d) is an important factor in the synthesis process. The relationship between the reactant initial density and combustion wave velocity are shown in Figure 2.12. While the combustion velocity generally decreases with increasing particle size, the actual function may vary on some factors. Sometimes, the differences can be explained by T_{ad} of the reactants [11-13].

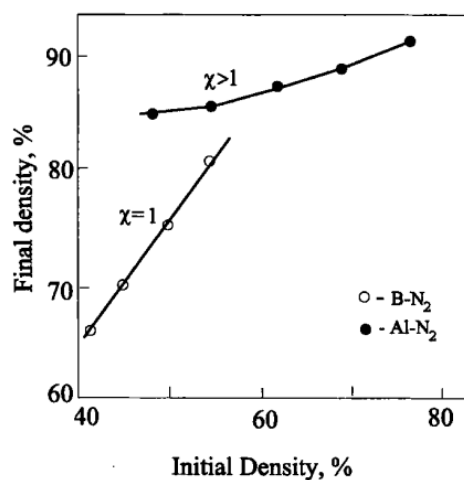


Figure 2.12. Final sample density as a function of initial density for B-N₂ and Al-N₂ systems [4].

2.6.4.2 Inert Gas Pressure

The inert gas pressure is also one of the factors affecting the reaction process as a function of the pressure dependency of the SHS process. The effect of inert gas pressure on the combustion wave for some reactions is shown in Figure 2.13.

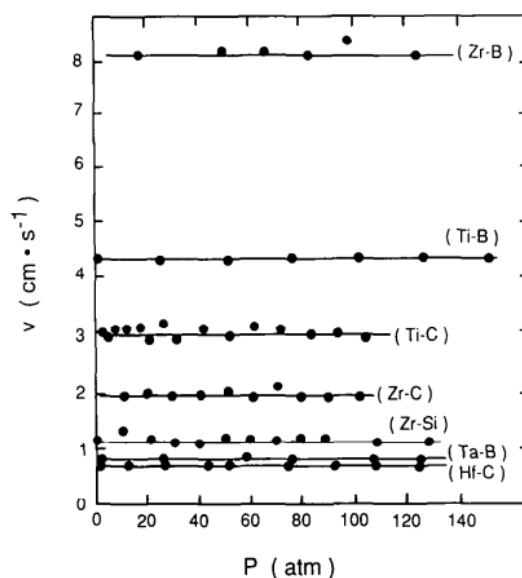


Figure 2.13. The relation of inert gas pressure and combustion wave velocity on some systems [70].

2.6.4.3 Green Pellet Density and Diameter

The properties and morphologies of the final product achieved by SHS reactions are also dependent on the reactant particle processing. The mixing and compaction of the green pellets are also the most important steps for SHS reaction. Dry and wet techniques are normally used to handle the powder processing. The green density of the reactants compacted by both dry and wet processes can vary significantly and will affect the whole SHS reaction and the thermal diffusivity of the reactants. The microstructure of the products was affected by the green density of the pellet, which reported by Moore et al. [13].

An important consideration relating to the deviation from adiabaticity depends on the shape of the combustion sample, especially the ratio of the surface area to

volume. Figure 2.14 shows the example of the influence of the sample shape on the degree of heat loss, in which the effect of the diameter of the cylindrical green pellet on the combustion temperature is presented. The temperature rises with increasing diameter up to an optimum value then turn into relatively constant with further increase in green pellet diameter [70].

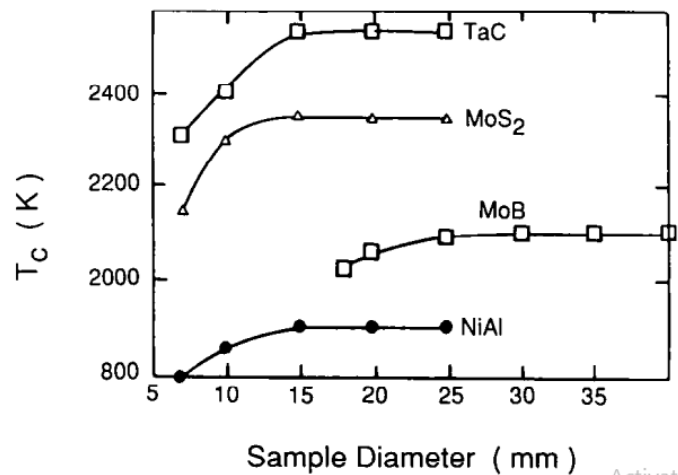


Figure 2.14. The relation of the pellet diameter and combustion temperature for various mixtures [70].

2.6.5 The Mechanism of SHS

Firstly, this process needs to produce the dry mixed reactant powders. For example, one could mix powdered reactants together and then press them into cylindrical pellets. SHS can be divided into 3 main steps; heat the workpiece at one end, reaction and progressively (propagated), and relaxation or cooling back to the initial state [71].

In the SHS mode, a reaction can be self-sustaining even at room temperature and the compacted green pellet only needs to be ignited at one end. The ignition or heating can be done by an electrically heated coil or even a laser. During combustion synthesis, the strongly exothermic reactions occurred, then the actual chemical reaction between the different elements is quickly originated. The temperature in the immediate layer raising to the ignition temperature, T_{ig} . The ignited elements of the pellet will exhibit as a combustion wave in a self-sustained mode and so on such that a combustion

wave travels through the green pellet on its own consensus propagating reactants and transforming them into products.

The process no longer requires the input of energy and thus it is identified as self-propagation. Consequently, effective energy-saving is just one of the many advantages of these simple reactions [11]. Figure 2.15 shows four photographs of a typical combustion synthesis process, which contain the ignition stage and the drive of the combustion wave as a function of time [72].

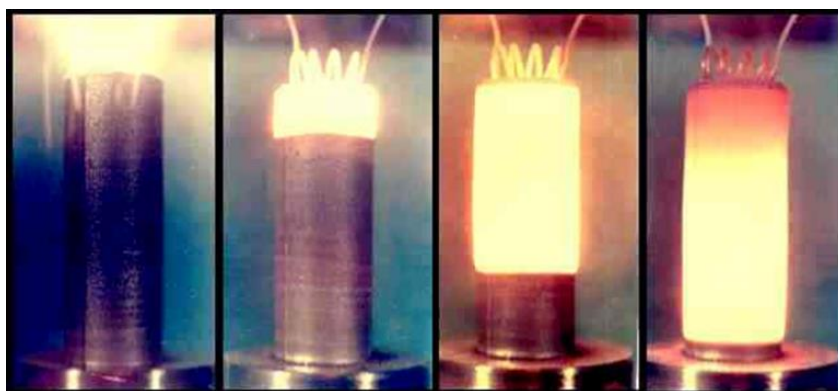


Figure 2.15. The digital photograph of the sample during combustion synthesis process [72].

The combustion wave propagated at a constant velocity, the reaction is called the stable self-sustaining. Conversely, the combustion wave velocity is unstable (stages of low and high propagation velocities) which is formed due to insufficient or not enough thermal and kinetic parameters, therefore, oscillatory or spin (spiral wave round compact) manners and can extinguish. However, there is a number of factors whether the reaction can be self-propagating or not.

The characteristic of chemical mixtures affects chemical and phase composition of the products along with their particle size and morphology [73]. The product structure development for the period of the chemical reaction was called primary structure formation whereas the structure formed in this event was called the primary structure of the product. The formation time of the primary structure is the same as the chemical reaction formation time which is typically 10^{-3} and 10^{-1} seconds. When the chemical reaction finished, the particle size growths as a consequence of the secondary structure development process followed by assembling recrystallization. The period of

the development depends on the sample cooling mode and is generally about certain or ten seconds [74, 75].

There are several ways to express the complicated multi-parametric transformation processes from initial reactants to final SHS products. The main types of the occurring processes are as follows;

- i. Solid-solid system: The combustion mode is solid-flame combustion with the intermediate melted layer.
- ii. Gas-phase SHS: The combustion mode is gas-phase combustion of condensed systems with gaseous intermediate zone, and chain flames.
- iii. Solid-gas system: The combustion mode is combustion of gaseous suspension, and filtration combustion [76, 77].

The SHS method has provided the possibility of producing a great quantity of compounds, ceramic matrix composites, in situ refractory ceramics, nanophase materials, and intermetallic alloys. Among the materials for which the technical backgrounds are well established [78, 79].

2.6.6 Applications of SHS

Two methodologies are being used in SHS technique; the first one is the production of intermediate products, which are then used as raw materials in further processing; the second one is the production of the final finished products, which are structured, shaped and carried out in a single-stage (simultaneous synthesis and densification) [80]. There are a number of materials, including the silicides, borides, carbides, and oxides of refractory metals which are considerable possible for both thermally and chemically stable films for microelectronic and many application [81].

There are many techniques such as hot-isostatic pressing (HIP), hot pressing and sintering, and plasma spraying can be produced the composite target. Nevertheless, these techniques need multi-step processing and can results many defects in target, for example, high oxygen content, porosities, impurities, and ununiformed microstructure. Self-propagating high-temperature synthesis provides an alternative for this production of composite targets used in the sputtering of composite thin films [82].

Table 2.5. Some products that can be synthesized by SHS [78-84].

Type of compound	Compounds and reaction temperatures of some systems (°C)
Silicides	MoSi (1900), Ti ₅ Si ₃ (2900), Zr ₅ Si ₃ (2800), Nb ₅ Si ₃ (3340), WSi ₂ (1500), V ₅ Si ₃ (2260)
Borides	ZrB ₂ (3310), TaB ₂ (3370), TiB ₂ (3190), MoB ₂ (1800), NbB ₂ (2400)
Carbides	TiC (3210), B ₄ C (1000), WC (1000), NbC (2800), TaC (2700), SiC (1800), ZrC (3400),
Carbonitrides	TiC-TiN, NbC-NbN, TaC-TaN
Nitrides	TiN (4900), ZrN (4900), BN (3700), AlN (2900), Si ₃ N ₄ (4300), TaN (3360)
Intermetallics	NiAl, FeAl, Ni ₆ Ge, NiTi, CoTi, CuAl
Chalcogenides	MoS ₂ , TaSe ₂ , NbS ₂ , WSe ₂
Cemented carbides	TiC-Ni, TiC-(Ni, Mo), WC-Co, Cr ₃ C-(Ni, Mo)
Composites	TiC-TiB ₂ , TiB ₂ -Al ₂ O ₃ , B ₄ C-Al ₂ O ₃ , TiN-Al ₂ O ₃
Hydrides	TiH ₂ , ZrH ₂ , NbH ₂

Nowadays, there are many compounds that can be produced by SHS process. Some products that can be synthesized by SHS are listed in Table 2.5. Some popular application of these materials are:

- Abrasives cutting tools and polishing powders,
- Powder for further ceramic processing,
- Resistive heating elements,
- Functionally graded materials,
- Shape-memory alloys,
- High-temperature intermetallic alloys,
- Composite materials, and Materials with specific properties Steel processing additives (nitrided ferroalloys),
- Electrodes for electrolysis of corrosive media,

- Coatings for containment of liquid metals and corrosive media, and
- Thin film and coatings [85, 86].

There are a number of ways of the SHS technologies. The technologically advanced type of SHS reactions is the synthesis reactions of refractory compounds from elements. The chemical reactions can be formed both powders and gaseous elements. Moreover, some additives additions are presented into the initial mixture. Another way is a combination of SHS with thermal reduction when the compounds of elements (oxides, halogenides, etc.) and metal-reducers (Al, Mg, Ca, Zn, etc.) are used for the synthesis [87, 88].

With the purpose of producing ultrafine and nanosized SHS products, one must use the reagents of the same dispersion. In solid-phase systems with the intermediate melted layer, the probability of nano-crystal formation depends on crystallization and recrystallization processes, combustion wave manners and product cooling after the reaction. On the other hand, investigation of the separation methods of chemically pure ultrafine and nanosized compounds from the synthesis products and their analysis are very important too [88].

Application of SHS agree to avoid the main disadvantages of conventional techniques—equipment complexity, high power consumption, and low product output. The advantages of this method are a low price and availability of raw materials.

2.6.7 Advantages and Disadvantages of SHS Process

SHS process has been proved to produce many high melting point materials, in situ refractory ceramics, nanophase materials, ceramic matrix composites, and intermetallic compounds. The significant advantages of the SHS technique are as follows;

1. *The process simplicity:* SHS process experimental configurations are uncomplicated and the process can be prepared with a low-cost reactor.
2. *The economic attraction:* SHS process is economically attractive due to a big cost-saving on the processing time and therefore is a considerable attraction for

the industry. It can also be used for complex structure or near-net-shape production for machine parts.

3. *Synthesis rate*: T_{ad} of the products can be calculated by thermal analysis and so cannot be synthesized directly by SHS. The synthesis process for this technique is fast and the products yield also higher.
4. *Products purity*: High purity of the products can be produced by SHS. The high temperatures associated with the combustion wave fabricated the higher purity of the products.
5. *Energy independence*; SHS technique is energy efficient technique because it is based on the use of highly exothermic reactions. Once the reaction starts, the heat of reaction ignites nearby the reactant layer and the combustion wave propagates throughout the sample itself. Therefore, there is no longer need to provide an external heating source.

Therefore, The SHS process is considered a cost-saving method to produce WSi_2 , with a low-cost reactor and lower requirements for a power source.

SHS is also accompanied by some disadvantages which include the following:

1. *Porosity*: The microstructure of the products often obtain a significant amount of porosity. The possible effect of the porous contamination may be due to the following factors:
 - (i) The vacancy of the green pellet generates the porosities in the product.
 - (ii) The porosity can arise when the product melts at T_c due to the solidification shrinkage.
 - (iii) The macroscopic expansion was caused by Kirkendall effect.
 - (iv) The porosity intrinsically occurs in the product when the volume changed between reactants and products.
 - (v) The entrapment and development of gaseous phases or low boiling point contaminations occurred throughout the reaction [13, 41, 90].
2. *Limited process control*: Subsequently the reaction rapidly take place and the maximum temperatures are sustained only for short times (seconds and minutes) compared to conventional heat treatment (hours and days). The variation in some process considerations is limited [90, 91].

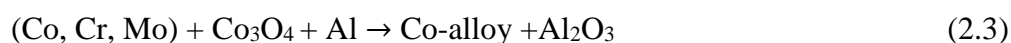
2.7 Related Literature

2.7.1 Synthesis of Orthopedic Implant Materials via Combustion Synthesis

The combustion synthesis phenomena also technologically advanced for biomedical applications. The ability of orthopedic implants to provide rapid healing and long-term clinical performance has been proven over many decades to offer patients a high quality of life while minimizing health care costs. In general, cobalt and titanium-based materials are used for orthopedic products [54, 92].

A. Varma et al. [54] used low-pressure combustion synthesis (LPCS) technique to produce Co-based and other metal alloys for orthopedic implants. These alloys can be used as knee and hip replacement, joint caps, screws, and wire as well. The advantage of this research work is that LPCS technique can be produced porosity free about (> 99% theoretical density) high purity alloys with stable phase and chemical compositions. This research also used quartz tube to cover the green pellet.

This invention used a green pallet, SHS reactor and also quartz tube, the same steps were used for SHS process. The reactants and reaction used for this invention are shown in Eq. (2.3).



In this research, thermodynamic analysis showed that the T_{ad} for the reaction at 1 atm argon atmosphere can be as high as 2900 K. But, even for calculated optimum compositions, experiments under normal ambient pressure show that gas released in the high-temperature reaction zone leads to the formation of pores and cavities in the final products as shown in Figure 2.16. In this figure, Mechanism of formation of CoCrMo alloys was shown and after phase separation between Al_2O_3 and the Co-based alloy, the Al_2O_3 cap appears. By using Low-pressure combustion synthesis (LPCS), it is shown in Figure 2.17, Al_2O_3 separate from the metal alloy in the form of a thin (1mm) tube coating the internal surface of the container. The absence of the aluminum cap speeds up the release of residual gas from the melt alloy bulk, thus leading to a pore-free material and also it avoids problems of alloy-slag adhesion. Figure 2.18 is a chart showing the influence of ambient gas pressure on alloy density and yield [70].

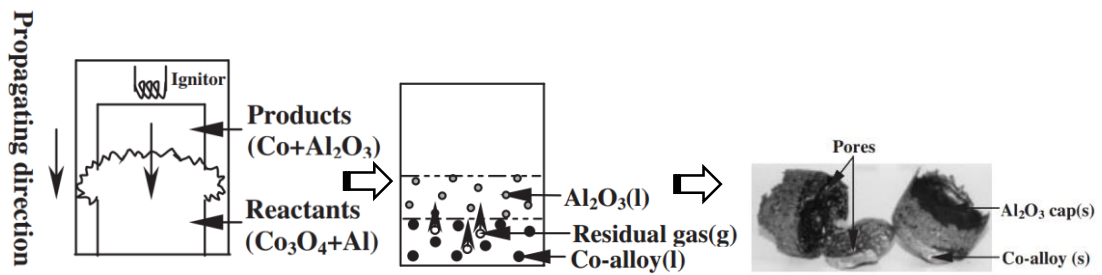


Figure 2.16. The schematic of the phase separation steps, (a) reacting, (b) melting and (c) final product (with pores) [92].

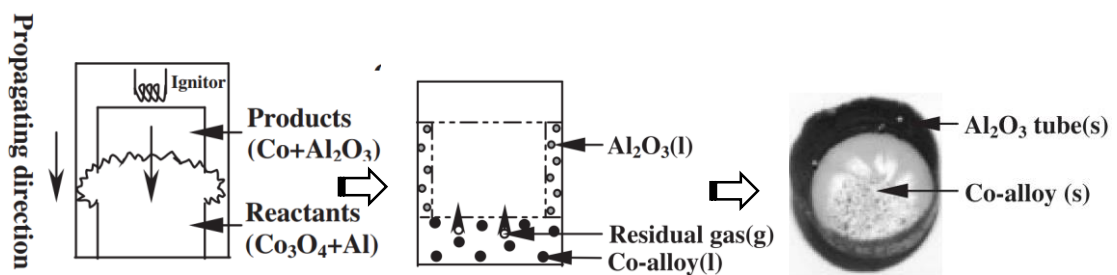


Figure 2.17. The schematic of the phase separation steps, (a) reacting, (b) melting and (c) final product (with thin film Al₂O₃ tube) [92].

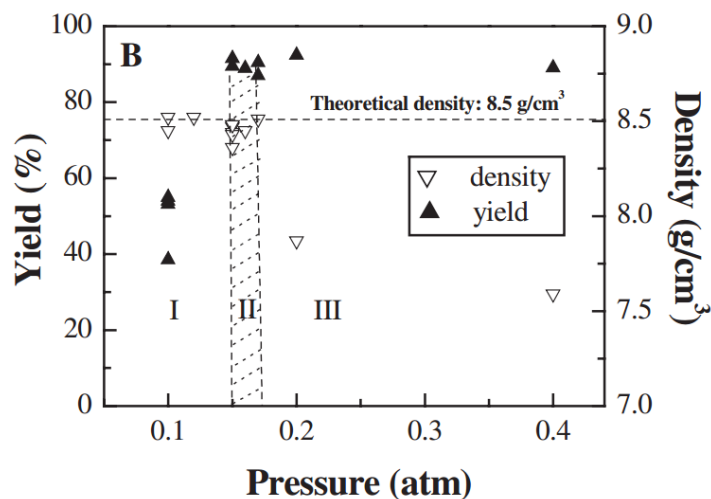


Figure 2.18. The influence of ambient gas pressure on alloy density and yield [92].

Figure 2.18 shows that the optimum yield and density of products can be acceptably obtained in region II. This is due to the absence of Al₂O₃ cap which allowed to move out the residual gas or bubbles from the alloy product as well as can prevent the adhesion between alloy and oxide slag. Thus, this phenomenon is also the novel

approach of the pore-free alloy synthesis by combustion synthesis. The Co-based alloy and machining specimens which synthesized from LPCS technique are shown in Figure 2.19.

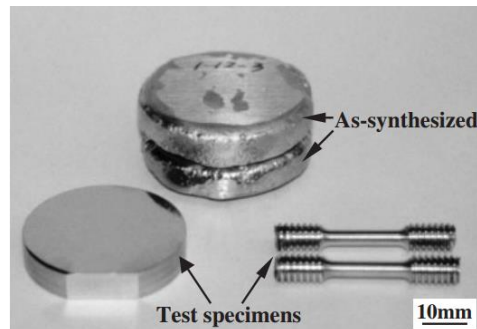


Figure 2.19. As-synthesized specimens and specimens prepared for hardness and tensile tests [92].

This research work can be summarized as follows;

1. Novel combustion synthesis of biocompatible Co-based alloys has been advanced by combustion phenomena.
2. High purity and pore-free implants can be produced only one step by synthesis method.
3. Self-purification and self-densification showed great commercial prospective for many different applications.

2.7.2 SHS-Casting of WSi_2 Intermetallic Compound

T. Chanadee et al. [21] synthesized WSi_2 intermetallic compound. The authors synthesized WSi_2 intermetallic compound by SHS process. The authors used WO_3 , Si, and Al as the reactant materials. In this research, the authors used quartz tube and graphite mold and varied the synthesizing pressure (0, 0.3, and 0.5 MPa) to investigate the formation mechanism and their variations and changes. The casting reaction is shown in Figure 2.20. The resulted product and microstructure are shown in Figure 2.21. The WSi_2 intermetallic compounds were synthesized by using SHS process and it was found that the used of quartz tube helped the phase separation of oxide and intermetallic product as well.

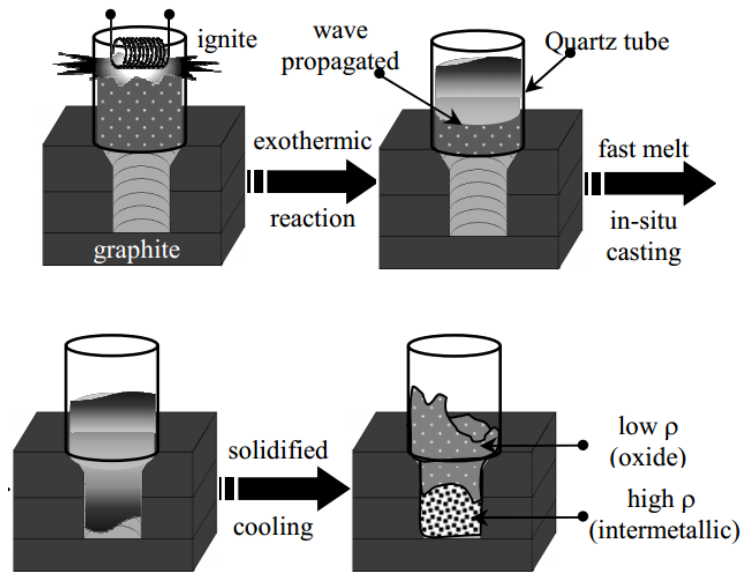


Figure 2.20. The illustration of the occurrences of the product during in-situ SHS-casting reaction [21].

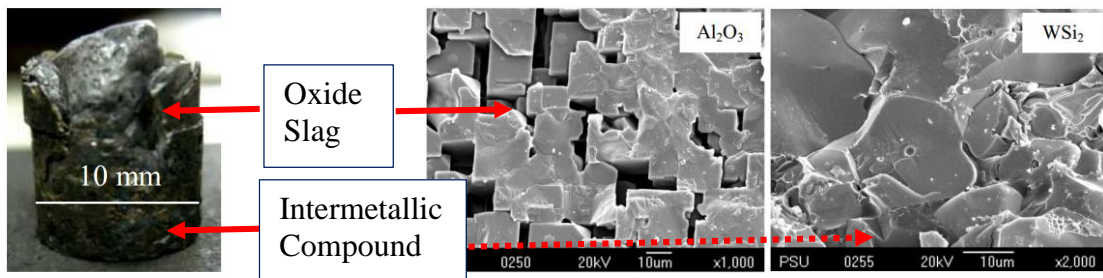


Figure 2.21. The macro and microstructure of the as-SHS product [21].

Figure 2.22 shows the XRD results of the intermetallic alloy and oxide slag. The intermetallic compound in Figure 2.22 (a) indicated all peaks are the WSi_2 tetragonal phase and the oxide slag Figure 2.22 (b) indicated that the major peaks are the Al_2O_3 and some residual phase as the WSi_2 intermetallic.

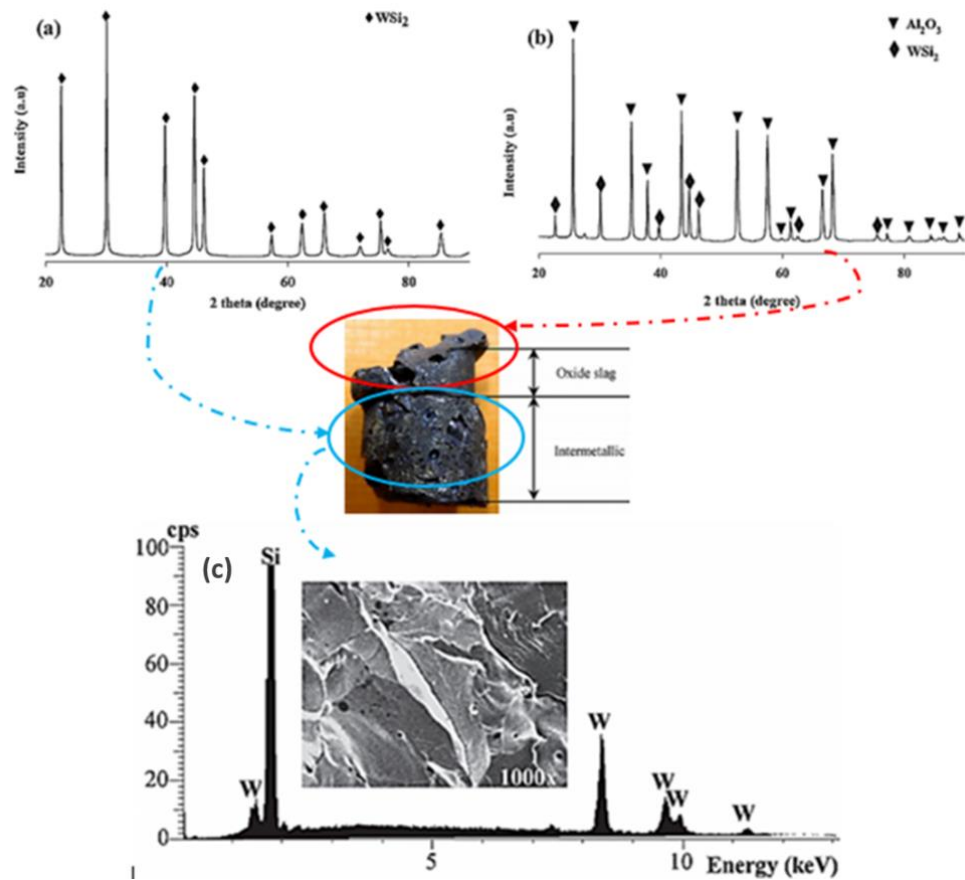


Figure. 2.22. XRD pattern of (a) intermetallic WSi_2 , (b) oxide slag (Al_2O_3 - WSi_2) and (c) EDX analysis of WSi_2 [21].

This research work can be summarized as follows;

1. The optimum condition of argon gas pressure is 0.5 MPa.
2. The quartz tube can be used as a substrate to reduce the heat lost during SHS reaction.
3. The phase separation of this research work can reduce the porosity of the intermetallic and dense product can be attained.

2.7.3 Investigation of Combustion Channel

The porous NiTi alloy implants synthesized using SHS and the combustion channel investigated by G. Tosun et al. [93]. In this study, the starting reactants were titanium and nickel powders and the powders were mixed and blended for 12 hr. The

authors used different compaction pressures (50, 75 and 100 MPa), preheating rate (30, 60 and 90 °C/min) and preheating temperature (200, 250 and 300 °C). Then, the effect of parameters on the NiTi product combustion channel characteristics was investigated. The results from the effect of cold compaction pressure, the effect of heating rate and the effect of preheating temperature are shown in Figure 2.23.

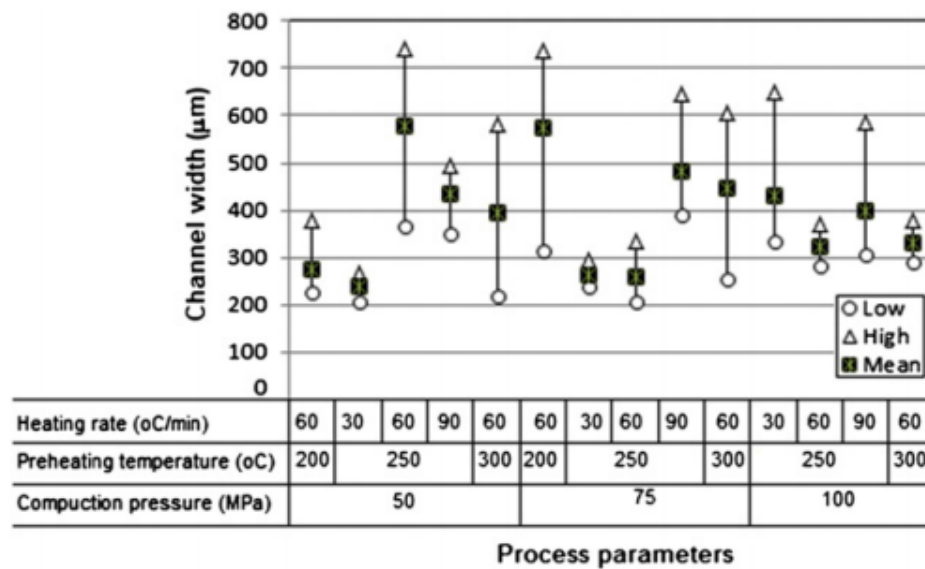


Figure 2.23. The effects of the synthesis parameters on the combustion channel width [93].

The cold compaction pressure affected the distance between the adjacent striations of the product samples are shown in Figure 2.24. When the compaction pressure was increased from 50 to 100 MPa, the combustion channel width also decreased.

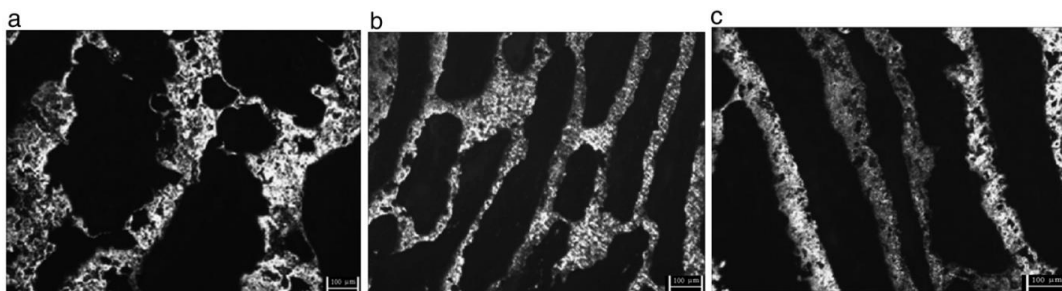


Figure 2.24. The effect of cold compaction pressure on the NiTi alloys produced at 250 °C preheating temperature and 60 °C/min heating rate, (a) 50 MPa, (b) 75 MPa, and (c) 100 MPa [93].

The preheating temperature of the green pellets affected the morphologies of the NiTi implant alloys. The obvious distribution microstructures were investigated as shown in Figure 2.25. The narrow combustion channel width obtained preheating temperature of 200 °C. When the preheating temperature was increased from 200 °C to 250 °C, the combustion channel width increased while the preheating temperature was increased from 250 °C to 300 °C, the distance between the adjacent striations decreased. The width of the channel contribution is related to that of the green compaction pressure. The combustion temperature and heat input increased when the preheating temperature increased. Therefore, wide and continuous combustion channels take place.

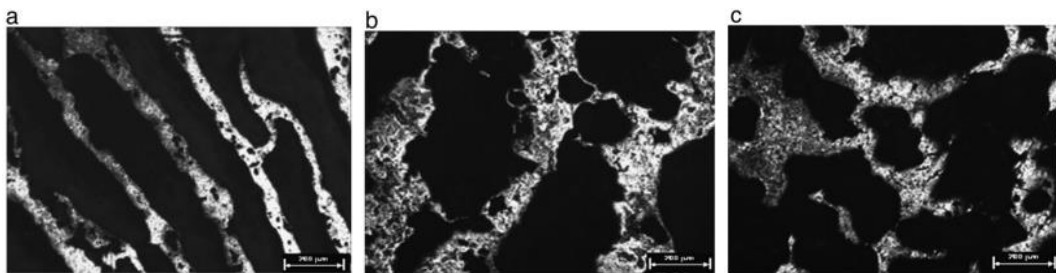


Figure 2.25. The effect of preheating temperature on the NiTi alloys produced at 50 MPa pressure, 60 °C/min heating rate, (a) 50 MPa, (b) 75 MPa, and (c) 100 MPa [93].

According to literature reviews, tungsten silicide can be synthesized by SHS process. And also, for higher density and purity alloy, it can use ambient gas pressure and green compaction pressure. Moreover, the use of quartz tube as a mold is expensive and the research work will be done by natural sand as a sand mold (SiO_2) in the SHS process. The SHS method can be used to produce WSi_2 intermetallic compound from two reactants systems with the benefits of energy saving as well as minimization of production time and cost. This research work used the scheelite (CaWO_4) minerals, calcium oxide (CaO) and tungsten oxide (WO_3) as a reactant material.

2.8 Characterization Techniques

The materials characterization is essential to determine the properties and applications of the product. Various characterization techniques such as X-ray diffraction (XRD), X-ray fluorescence (XRF), scanning electron microscopy (SEM), energy dispersive spectroscopy (EDS), and X-ray fluorescence (XRF) have been used to characterize the intermetallic alloy, oxide slag, scheelite mineral, natural sand and reactant powders of these research work.

2.8.1 X-ray Diffraction

X-ray powder diffraction (XRD) is an analytical technique used to give the information and identification of the crystalline, amorphous, and structure of the materials. In 1919, A. W. Hull revealed that every crystalline element has their own structures. He also mentioned that the same patterns will always appear for the same elements and the mixture of elements also produce their patterns independently of the others in terms of X-ray pattern [94]. Laue confirmed in 1937 that the X-ray diffraction technique can observe ten thousand times higher than that the microscope provided [95].

XRD is constructed on interference between the crystalline sample and the monochromatic X-rays. When X-rays strike a crystalline phase, a diffraction pattern is generated due to the interaction between the incident X-rays and the atomic structure of the solid. When a focused X-ray beam interacts with these planes of atoms, the beam undergoes various modifications like transmission, absorption, refraction, scattering, and diffraction. The diffracted beam can provide information about the d-spacing by applying Bragg's law given by equation 2.4,

$$n\lambda = 2d \sin \theta \quad (2.4)$$

Where, n = an integer,

λ = the incident wavelength,

d = the spacing between the planes in the atomic lattice, and

θ = the angle between the incident ray and the scattering planes.

“The principle of the schematic stretching” of X-ray diffraction based on Bragg's law is shown in Figure 2.26 [96].

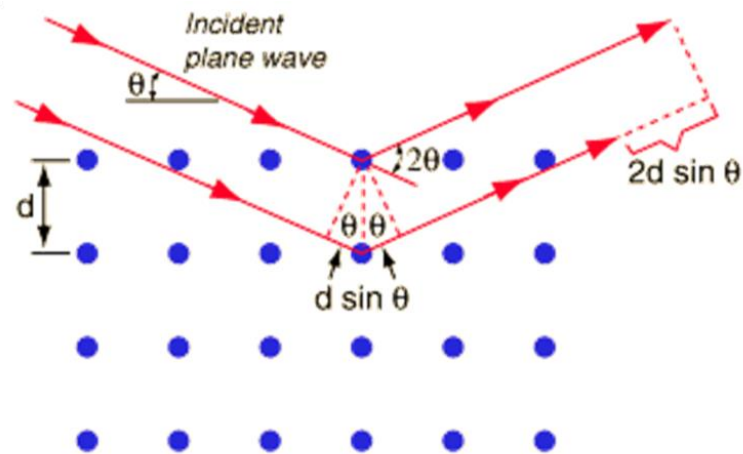


Figure 2.26. The principle of schematic stretching X-Ray diffraction [96].

2.8.1.1 Basic Principles of XRD

X-rays are produced normally by X-ray tubes, which is the main part of the X-ray diffractometer. X-ray tube contains a source of electrons and two metal electrodes in a vacuum tube. The high voltage maintained across these electrodes rapidly draws the electrons to the anode (the metal target). The metal targets commonly used in x-ray tubes are Cu, Co, and Mo, which emit characteristic X-ray wavelengths of 1.54 \AA and 0.8 \AA equivalent to the energies of 8 keV and 14 keV, respectively. X-rays are emitted when the electrons strike the anode. The schematics of the cross-section of the laboratory X-ray tubes is shown in Figure 2.27.

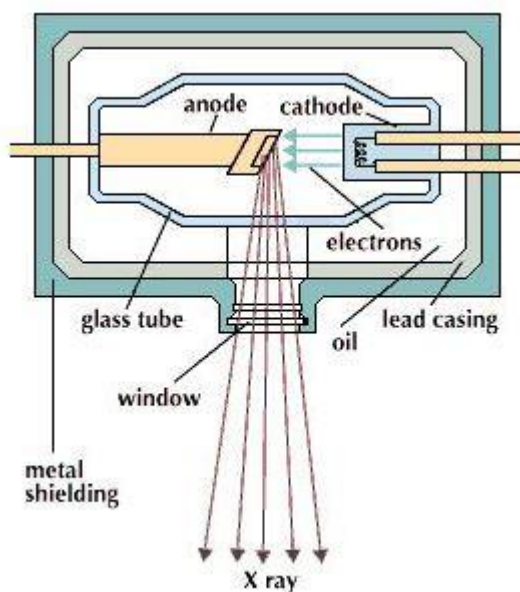


Figure 2.27. Schematics of the cross-section of the laboratory X-ray tubes [97].

The X-ray spectra generated by this technique produce a structural fingerprint of the unknown element. XRD is thus preferably appropriate for characterization and identification of polycrystalline phases and also used to investigate lattice parameters, atomic arrangement, and average particle sizes. Moreover, the areas under the peak are related to the amount of each phase present in the sample. Furthermore, the relative peak height is generally proportional to the number of grains in a favored orientation. The relative areas of the peak of respective elements constituted in a multicomponent materials is used to obtain a semi-quantitative analysis of materials [98]. Joint Committee on Powder Diffraction Standards (JCPDS), also presently known as International Center Diffraction Data (ICDD) is the association that preserves the database of inorganic and organic spectra. The JCPDS data requires to identify the existence of standard patterns. The database is available from ICDD direct or diffraction equipment manufacturers.

2.8.1.2 Limitation of XRD

Only crystallites having reflecting planes (h, k, l) matching to the specimen surface will give to the reflected intensities. Therefore, the analyze specimen must be crystalline. For mixed materials, such as alloy, mineral and oxide form of specimen,

detection limit is $\approx 2\%$ of specimen. It may be difficult to detect light atoms such as H, He, Be, and B by XRD. Cambridge file for organic single crystal data, JCPDS, and NBS crystal data are required to identify the existence of the standard pattern. XRD also has size limitations. It is much more accurate for measuring large crystalline structures more willingly than small crystalline structure. Small structures that are present only in trace amounts will often go undetected by XRD readings, which can result in skewed results. Furthermore, XRD also use harmful X-ray radiations.

In the present work, XRD patterns were recorded using, X'Pert MPD, PHILIPS, Netherlands. The Phillip X'Pert MPD Diffractometer is a versatile instrument that is designed to use in many X-ray data collection applications. Spectra were recorded at 30 mA and 40 kV, using Ni-filtered $\text{CuK}\alpha$ radiation (1.5418 \AA). The scan rate (2θ) was $3^\circ/\text{min}$ with a step size of 0.05. Figure 2.28 shows an example of a photograph of the powder X-ray diffractometer.

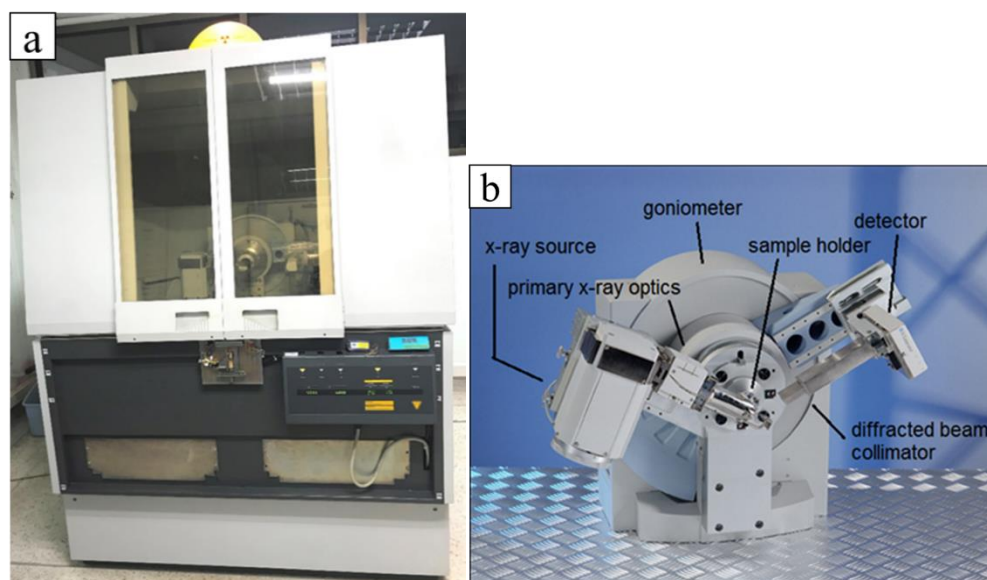


Figure 2.28. Photograph of (a) the powder X-ray diffractometer, and (b) the main components of the X-ray diffractometer assembly [99].

2.8.2 Scanning Electron Microscopy

Scanning electron microscopy (SEM) is a technique to examine topography and surface morphology of materials. The SEM is an apparatus that generates a highly

magnified image by electrons instead of light to form an image. Many types of signals are produced when the electron beam hits on the surface of the specimen. An SEM image is formed by focusing electron beam that scans over the surface area of a specimen.

2.10.2.1. Basic Principle of SEM

A schematic diagram of the major components of the typical SEM is shown in Figure 2.29. The typical SEM apparatus includes a heated filament as a source of the electron gun, specimen chamber which contains holder and stage, condenser lenses, objective lenses, amplifier, aperture and electron detector, etc. The electron gun produced the electron beams at the top of the microscope. The electron beam travels a vertical route through the microscope, which is held within a vacuum chamber. The electron beam emitted from an electron gun is condensed to a fine probe for surface scanning.

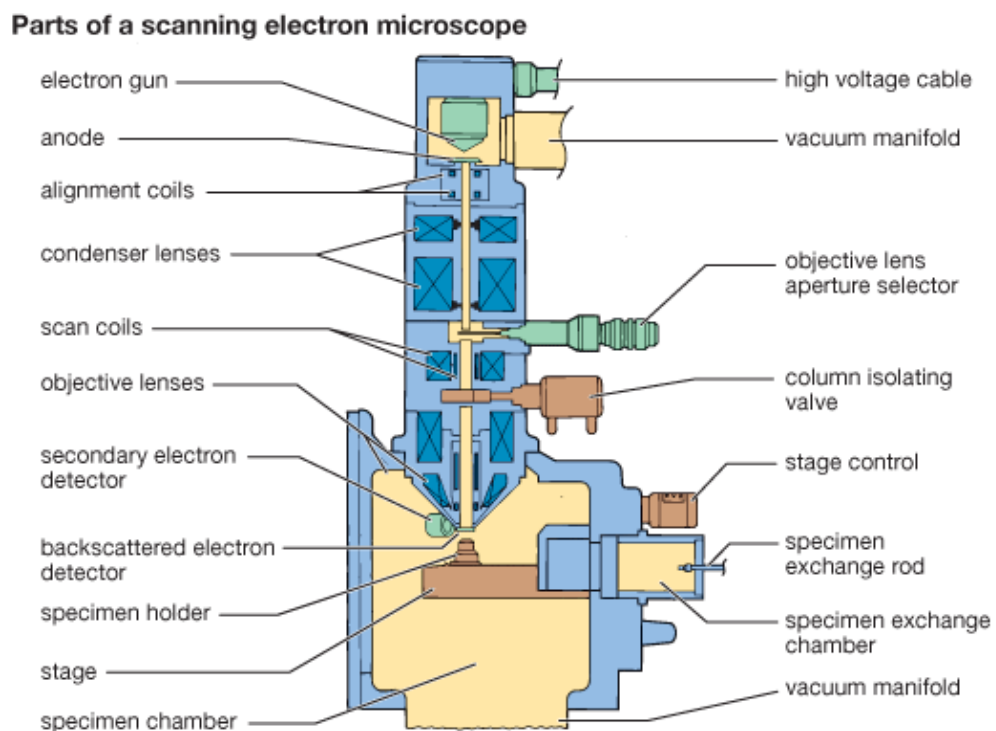


Figure 2.29. Schematic of the major components of a typical scanning electron microscope [100].

The electron beam moves through electromagnetic fields of the magnetic lenses, which focus the beam down towards the specimen. Once the beam impinges the specimen, electrons, and X-rays are generated from the sample. Once the signals are emitted, detectors collect these X-rays and any of these can be displayed as an image. Secondary electrons (SE) and backscattered electrons (BSE) are the most often used signals in SEM. Some electron is scattered inelastically due to the ejection of loosely bound electrons from the specimen. Secondary electrons are formed through inelastic scattering. Surface topography and morphology of the specimen are analyzed by SE images. In different, back-scattered electrons are generated from the specimen by elastic scattering. Since the intensity of the BE signal is strongly related to the atomic number (Z), therefore, BSE images can provide evidence about the distribution of dissimilar elements in the specimen. Types of signals generated by the collision of electrons with a specimen are shown in Figure 2.30. Example of the different images between SE and BSE is shown in Figure 2.31.

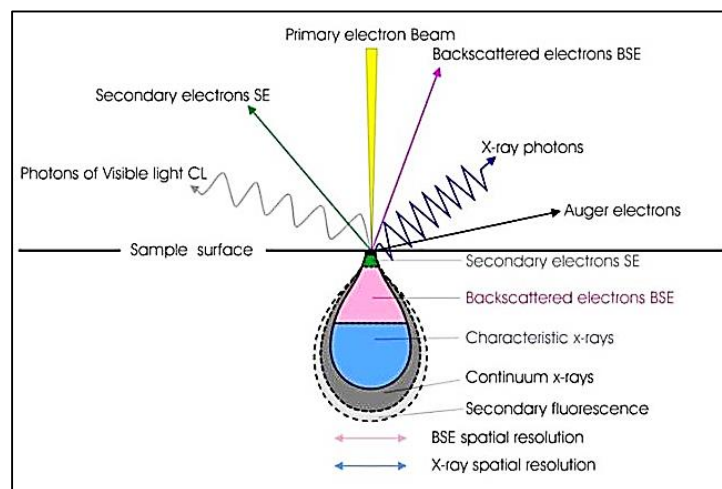


Figure 2.30. Types of signals generated by the collision of electrons with a specimen [100].

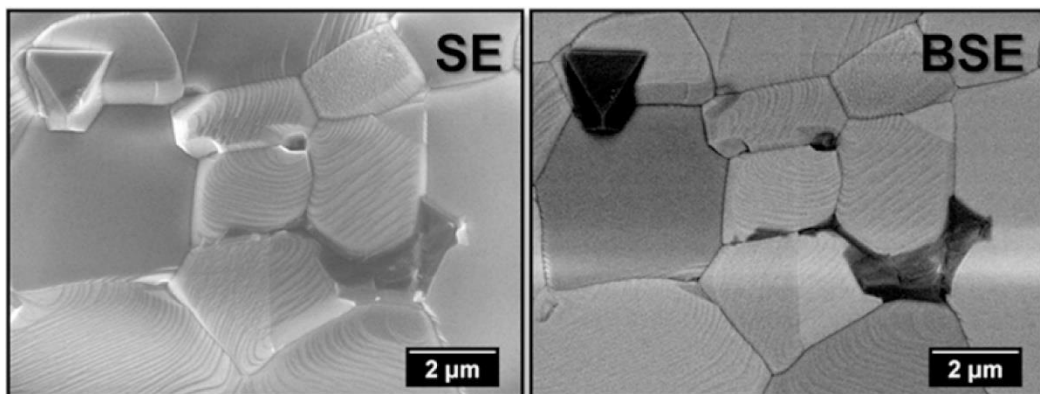


Figure 2.31. SEM images of triangular precipitates at SnMnNBo sample (a) SE image, and (b) BSE image [101].

When the electron beam ejected the inner shell electron, an electron from higher energy levels falls to lower energy levels causing into the emission of Auger electrons, Auger electrons are used to get information of the chemical composition of the specimen, which is called an Auger electron spectroscopy (AES). In the process, the emission of high energy-photons are also produced which is known as X-ray photons. This is normally used for the compositional analysis of the materials, which is known as X-ray energy dispersive analysis (EDX or EDS).

2.8.2.2 Limitation of SEM

SEM cannot show the internal details of the sample and also cannot obtain the highest resolution. Some sample need to be coated with a conductive layer. EDS (EDX) detector on SEM cannot detect very light elements (e.g. H, He, and Li), and many instruments cannot detect elements with atomic numbers less than 11 (Na).

In the present study, morphologies and elemental analysis of resulting products were observed by a scanning electron microscope (SEM, Quanta 400, FEI, USA), coupled with an energy dispersive X-ray spectrometer (EDX, ISIS 300, Oxford, England). Figure 2.32 shows a photograph of the scanning electron microscopy (SEM, Quanta 400, FEI, USA).

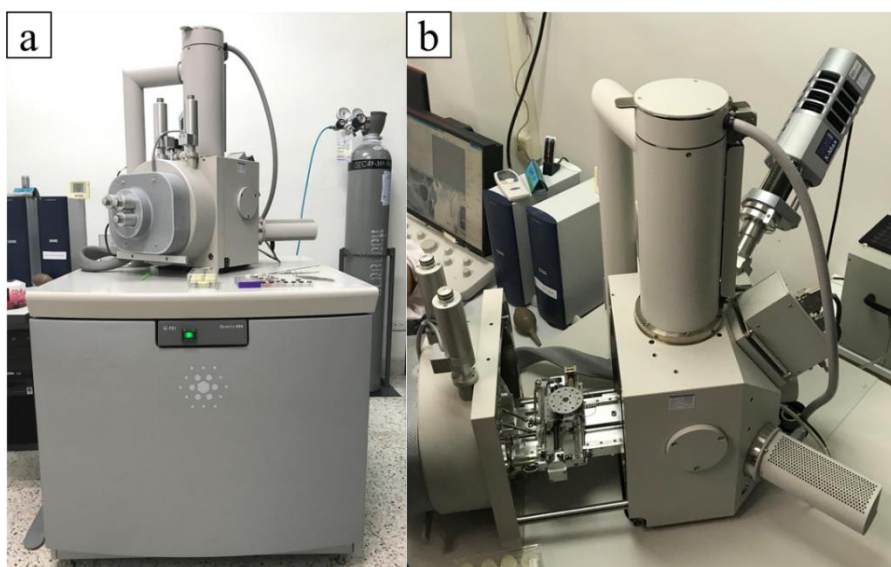


Figure 2.32. A photograph of (a) the scanning electron microscope, and (b) specimen holder and the vacuum chamber (SEM, Quanta 400, FEI, USA).

2.8.3 X-ray Spectroscopy

X-ray spectroscopy is a technique of using characteristic X-rays to identify elemental composition of the specimen. X-ray spectroscopy analyses the presence and quantities of chemical elements of the materials whereas X-ray diffraction analyses crystal structure of the materials. The characteristic X-rays are produced from atoms irradiated by the high-energy beam. The elemental composition is recognized both from the X-ray wavelength, as in X-ray wavelength dispersive spectroscopy (WDS), and from the X-ray energy, as in X-ray energy dispersive spectroscopy (EDS).

2.8.3.1 X-ray Energy Dispersive Spectrometer

X-ray energy dispersive spectroscopy (EDS, EDX or EDXS) is an analytical technique used to determine the composition of the elements in the specimen. Backscattered electron image in scanning electron microscope technique yields the different contrast images depending upon the different composition of the elements. The specific elemental composition and their relative proportions of the elements contained the specimen are classified by EDS technique. EDS detector accumulates the

signals of characteristic X-rays energies from elements in a specimen, therefore, it is faster than X-ray wavelength technique. The typical resolution of energy dispersion in EDS is about 150-200 eV.

2.8.3.2 Basic Principle of EDS Analysis

The high energy electron beams in an SEM is normally used to strike the materials, and X-rays are produced. The Si (Li), the most commonly used detector, used to detect the X-rays in an EDS system. The typical schematic of an energy dispersive spectrometer is shown in Figure 2.33.

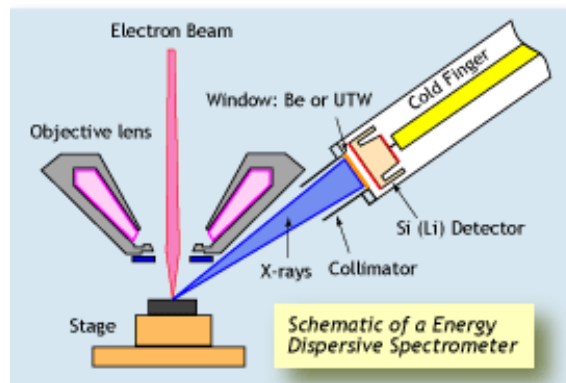


Figure 2.33. The typical schematic of an Energy Dispersive Spectrometer [102].

Characteristic X-rays is produced by excitation of an electron in the inner shell of an atom to escape from its original position making an electron-hole, another electron from the outer shell which has high energy jumps to the low energy shell to fill in that hole. X-rays are emitted by the difference energy between two energy levels, which are characteristics of elements existed in the specimen (there could be several characteristic wavelengths for each element). EDS is based on the detection of these characteristic X-rays. Due to the quantization of electron energy levels, the emitted characteristic X-ray energies for elements will normally be dissimilar from element to element with only a few spectral peaks overlapping. Its characterization capabilities are due in large part to the primary principle that each element of the periodic table has a unique electronic structure and, thus, a unique response to electromagnetic waves [103]. The illustration of the atomic model of the characteristic X-ray production is shown in Figure 2.34. The

penetration of the probe in EDS analysis is normally around 1-3 μm which show in Figure 2.35. All these waves and electrons are detected by corresponding detectors equipped with a specimen chamber, and then images and spectra can be obtained after signal processing.

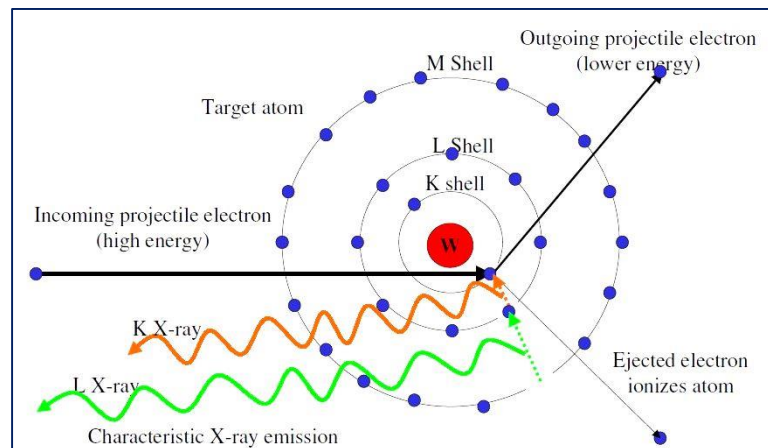


Figure 2.34. Illustration of the atomic model of the characteristic X-ray production [104].

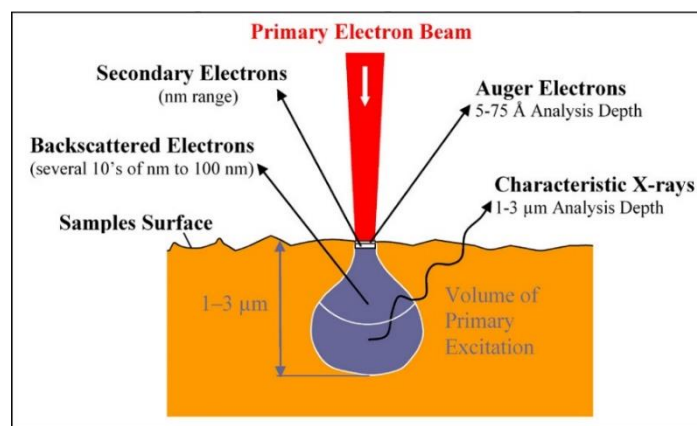


Figure 2.35. A schematic diagram of electron-matter interactions for SEM [105].

Quantitative elemental compositions of materials can be generated spot, line, and area maps of elements. The elemental map may be colored on the SE or BSE images. Figure 2.36 shows the elemental compositions of different materials obtained using EDS analysis as an example.

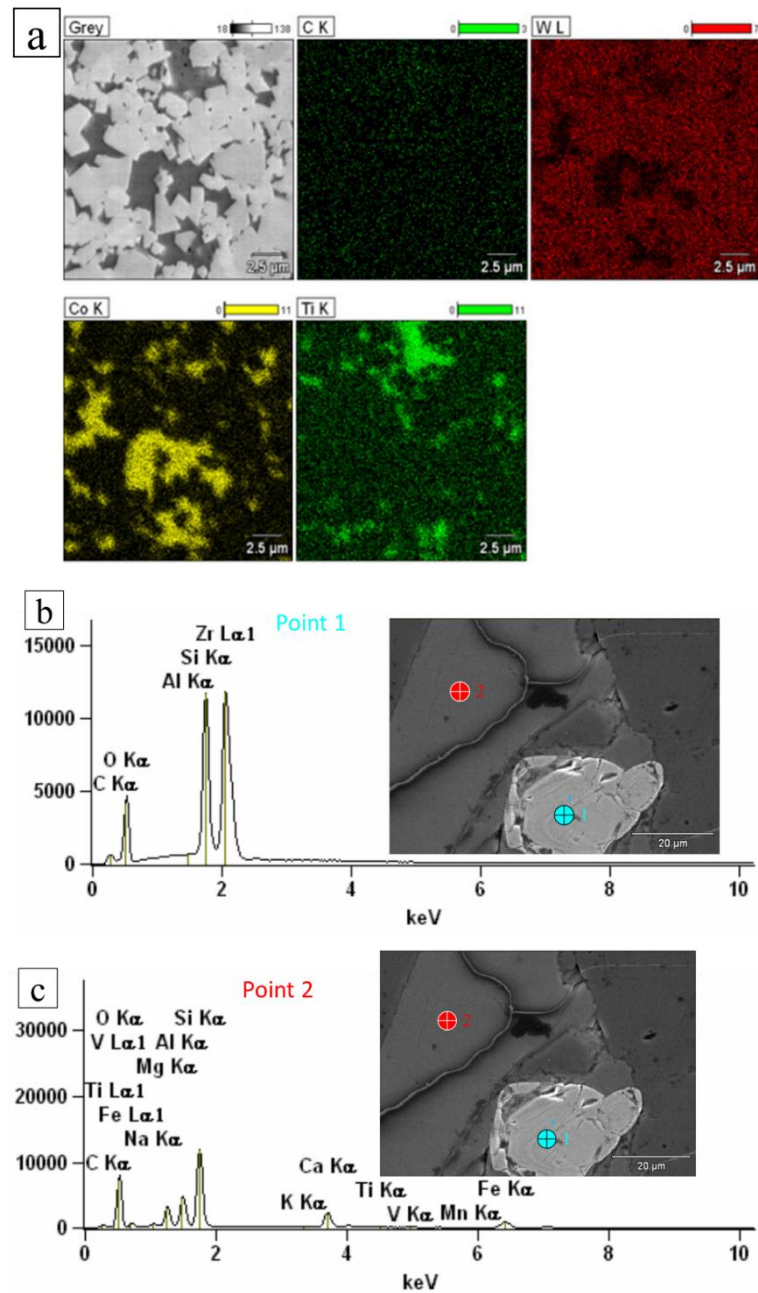


Figure 2.36. The elemental compositions analysis of (a) Mapping analysis of carbon, tungsten, cobalt, and titanium of the sinter obtained from a powder mixture of WC-Co +1wt.% TiC, SEM, EDS [106], and (b,c) localized elemental information of series of spots and generated spectra, Adopted from [100].

In the present study, morphologies and elemental analysis of resulting products were observed by a scanning electron microscope (SEM, Quanta 400, FEI, USA),

coupled with an energy dispersive X-ray spectrometer (EDX, ISIS 300, Oxford, England).

2.8.4 X-ray Fluorescence Spectrometer

X-ray fluorescence spectrometer (XRF) is an analytical technique to characterize the chemical composition of the materials. The materials can be solid, powder, liquid or another form. XRF technique is accurate, faster and normally needs only a minimum of sample preparation. XRF can be separated into two main techniques as energy dispersive X-ray technique (EDXRF) and wavelength dispersive X-ray technique (WDXRF). The elements that can be investigated and their detection levels mainly relate to the spectrometer system used. XRF instruments are capable of analyzing solid, liquid, and thin-film samples for both major and trace (ppm-level) components. The analysis is rapid and usually, sample preparation is minimal or not required at all.

2.8.4.1 Basic Principle of XRF Analysis

X-ray fluorescence analysis has its basis in the phenomenon that, when atoms in a material sample are excited by the primary X-radiation, electrons from the innermost shells are released; the resultant vacancies are then filled by electrons from the outer shells. XRF uses X-ray radiation to excite the emission of characteristic X-rays from sample atoms. The word “fluorescence” is used to distinguish the secondary X-ray emission of sample atoms from the primary X-rays irradiating the sample. XRF analyzes the chemical elements of a sample by detecting the characteristic X-rays emitted from the specimens after radiation by high-energy primary X-rays. Illustration of the generation of X-ray fluorescence radiation in the atomic model is shown in Figure 2.37.

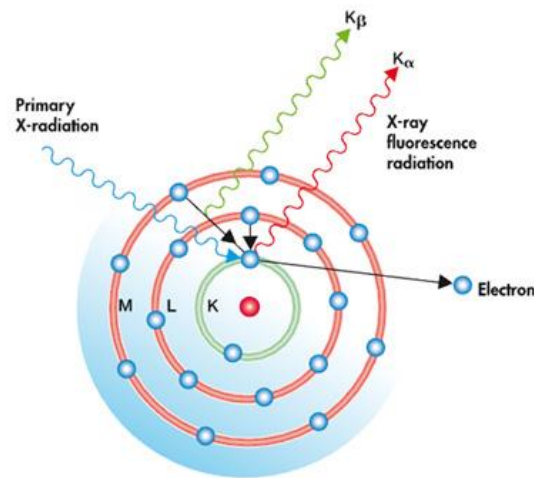


Figure 2.37. Illustration of the generation of X-ray fluorescence radiation in the atomic model [107].

The main difference between the (WDXRF) and (EDXRF) equipment is in the X-ray detection systems. WDXRF uses single crystal diffraction to detect characteristic wavelengths produced from the specimen. EDXRF uses a photon detector, typically a Si(Li) diode to separate the characteristic X-ray photons according to their energy. The two different X-ray detection systems are shown in Figure 2.38. However, EDXRF and WDXRF spectrometers have their own advantages, disadvantages, and limitations. Table 3.1 shows a comparison of the two techniques.

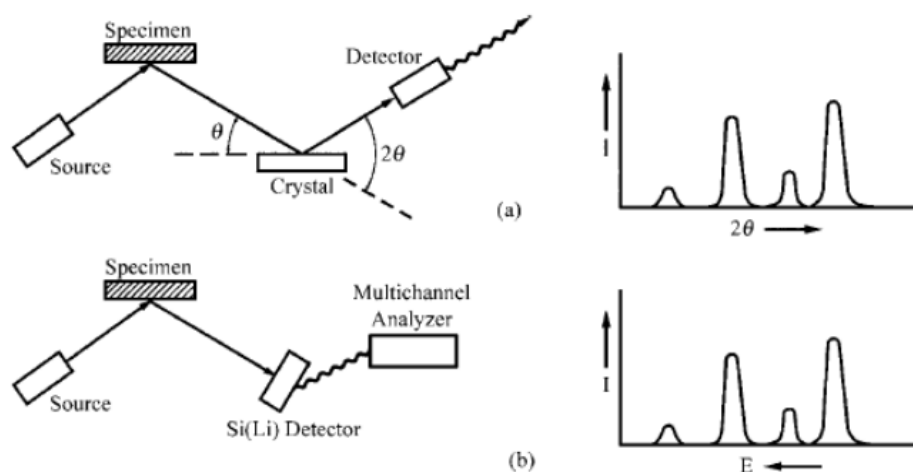
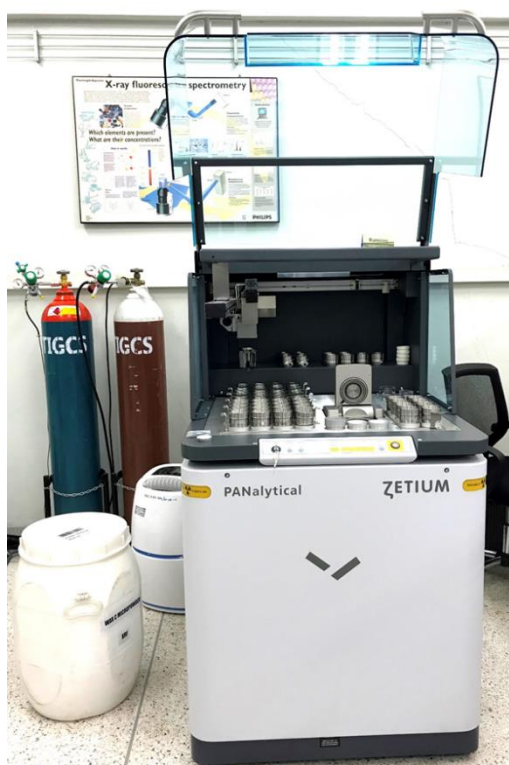


Figure 2.38. The different X-ray detection systems in (a) WDXRF, and (b) EDXRF [108].

Table 2.6. The comparison of the WDXRF and EDXRF techniques [109-111].

	WDXRF	EDXRF
Charges	Expansive	Inexpensive
Elemental Range	Be-U	Na-U
Resolution	Sensible for light elements	Less sensible for light elements
Detection	High detection limit (100 ppm)	Low detection limit (1000 ppm)
Measurement	Long analysis time	Fast analysis time
Power usage	200-4000 W	1000 W
Moving Part	Goniometer, crystal	-

**Figure 2.39.** A photograph of X-ray fluorescence spectrometer (XRF, PANalytical, Zetium, UK).

In the present study, elemental analysis of scheelite (CaWO_4) mineral and natural sand were observed by the X-ray fluorescence spectrometer, EDXRF technique,

(XRF, PANalytical, Zetium, UK). A digital photograph of the X-ray fluorescence spectrometer (XRF, PANalytical, Zetium, UK) is shown in Figure 2.39.

2.8.5 Density Measurement

2.8.5.1 True Density

Density is simply calculated as the ratio of mass to volume. For a regular shape e.g. cubic or prim, the volume of the bulk object can be readily measured by a ruler, because the substance in the bulk is closely packed. Archimedes' Principle is the determination of true density and accurate method for determining the volume of an irregularly shaped object, like a rock. The true density (ρ_t), is the volume of solid only and any closed pores within that are not open to the outside surface. The apparent weight of the specimens was measured during the specimens immersed in a liquid. The volume of the specimen decreases by an amount is equal to the weight of the volume of the liquid that it displaces.

The following calculations were assumed that assumed that 1 mL of water has mass almost equal to 1g under a normal room temperature (25-30 °C). The true density of the object is then expressed in Eq. 3.2.

$$\rho_t = \frac{m}{V_2 - V_1} \quad (3.2)$$

Where; ρ_t = True density (g/cm³)
 m = Weight or mass in air (g)
 V₂ = Volume of an object immersed in water (cm³)
 V₁ = Volume of water before object immerse (cm³)

2.8.5.2 Bulk Density and Apparent Porosity

The bulk density (B) is the density measurement including voids or pores within the sample (bulk volume). The apparent porosity (P) is the measurement of the pores percentages on the surface of the sample.

This test method is the measurement of bulk density (B), apparent porosity (P), and specific gravity of the desired sample by (ASTM C373-88-2006). It can determine the degree of maturation of a ceramic body, or the structural properties that may be required for a given application.

The test specimens were dried to get the constant mass by heating in an oven at 150°C , followed by cooling in a desiccator. The dry mass, D , was determined to the nearest 0.01 g.

The specimens placed in a pan of distilled water and boil for 5 h, taking care that the specimens are covered with water at all times. The cotton rope was used to separate the specimens from the bottom and sides of the pan and from each other. After the 5-h boiled, the specimens were allowed to soak for an additional 24 h. After impregnation, the test specimens were determined the mass, S , to the nearest 0.01 g of each specimen while suspended in water.

After the determination of the suspended mass, all specimens were blotted lightly with a moistened cotton cloth to remove all excess water from the surface. Then, the saturated mass, M , was determined to the nearest 0.01 g.

The following calculations were assumed that assumed that 1 mL of water has a mass almost equal to 1g under a normal room temperature ($25\text{-}30^{\circ}\text{C}$). The exterior volume, V , in cubic centimeters, was calculated by Eq. 3.3.

$$V=M-S \quad (3.3)$$

The apparent porosity, P , was calculated by Eq. 3.4.

$$P=\left[\frac{M-D}{V}\right]\times 100\% \quad (3.4)$$

The bulk density, B , in grams per cubic centimeter, was calculated by Eq. 3.5.

$$B=\frac{D}{V} \quad (3.5)$$

Where; V = the exterior volume (cm^3)

M= the saturated mass (g)

S= the mass while suspended in water (g)

P= the apparent porosity (%)

D= the dry mass (g)

B= the bulk density (g/cm³)

Chapter 3

Research Methodology

The methodology of this research work was divided into three main parts. The first one is to find the optimum conditions for the synthesis of the aluminothermic reaction of tungsten silicide (WSi_2) intermetallic from two different raw materials. The second one is to analyze the mechanism of phase separation between the sand mold and oxide slag. The last one is to produce tungsten silicide ($WSi_2-W_3Si_5$) intermetallic alloys via magnesiothermic reduction reaction.

3.1 Raw Materials

The raw materials and chemicals used in the experiment are shown in Table 3.1 and 3.2. The morphological characterization of SEM images of the as-received reactant powders is shown in Figure 3.1.

Table 3.1. Chemical composition, particle size and sources of raw materials.

Raw Material	Chemical Composition Mass Fraction (%wt)	Particle Size (μm)	Source
Scheelite Mineral CaWO ₄	13.369-CaO 84.098-WO ₃	~300	Chiang Mai Mining Co., Ltd., Thailand
Tungsten Oxide WO ₃	99.90	29.44	Fluka analytical, USA
Calcium Oxide CaO	97.00	13.47	Himedia Laboratories, India
Silicon (lump) Si	98.50	7.37	Sigma-aldrich, USA
Aluminium Al	99.00	22.42	Himedia laboratories, India
Magnesium Mg	99.00	-	Riedel-deHaen,
Silica Sand (SiO ₂ -Quartz)	97.16	~200	Hat Kaew area, Singhanakorn district

Table 3.2. List of chemicals used in the experiment.

Chemical	Composition	Source
Sodium silicate Na_2SiO	d= 1.5 g/ml	Fisher Scientific, UK
Ethanol $\text{C}_2\text{H}_5\text{OH}$	Absolute (AR)	RCI Labscan, Thailand

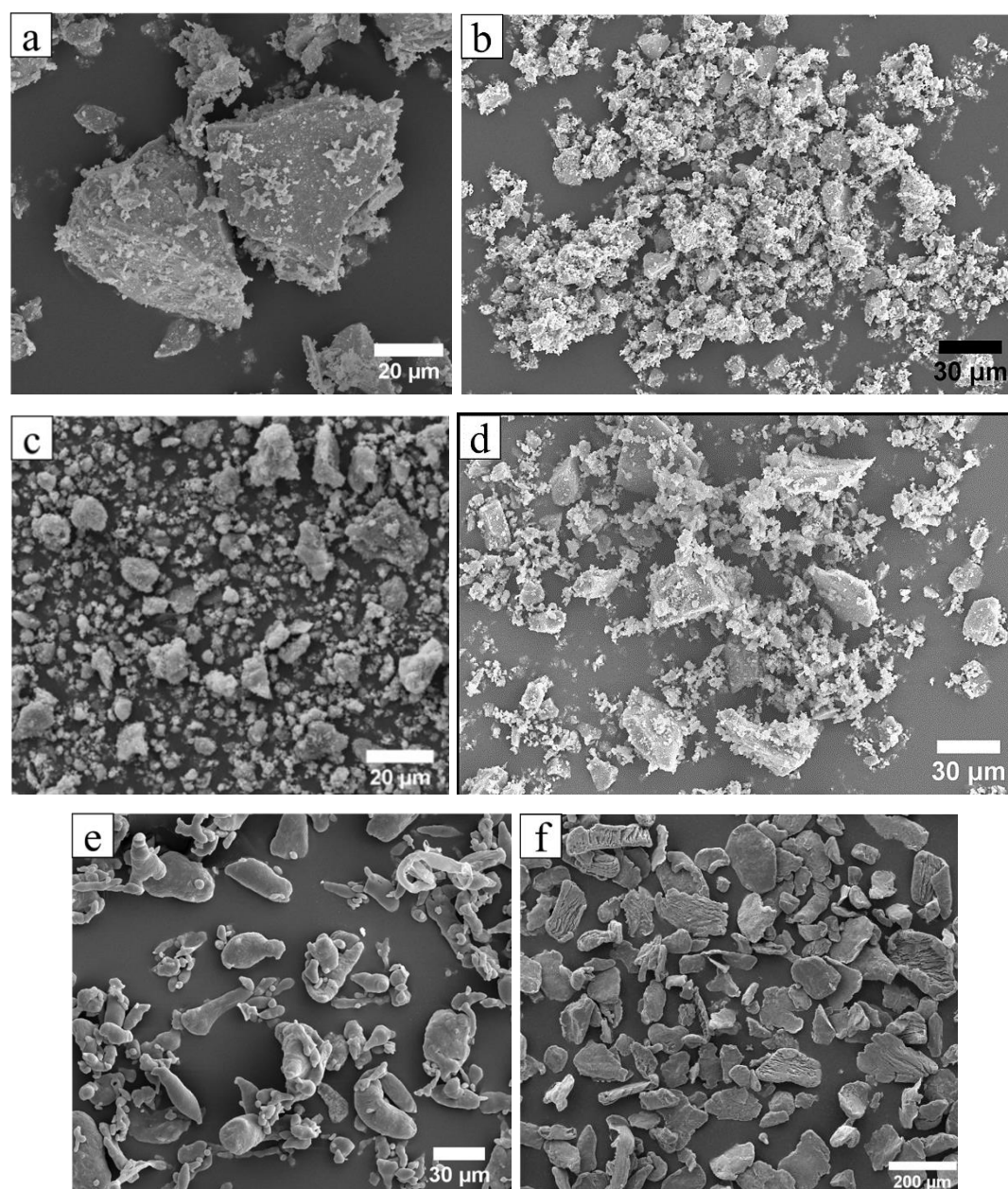


Figure 3.1. Morphologies of the reactant powders used in the experiment (a) CaWO_4 , (b) WO_3 , (c) CaO , (d) Si , (e) Al and (f) Mg .

3.2 Equipment and Tools

The equipment and tools used in the experiment were listed in Table 3.3. It was also listed their models and types of the equipment.

Table 3.3. The list of equipment models and types for the experiment.

Equipment/Tool	Type	Model
Planetary Ball Mill	Retsh	PM 100/200
Electronic Balance	OHAUS, NJ	PA-214
Steel Mold and Die (25.4 mm ϕ)	-	-
Steel Mold and Die (36 mm ϕ)	-	-
Hydraulic Pressing Machine	Huat Seng	1939-15T
SHS Reactor	By Dr. Sutham Niyomwas	-
Oven	Memmert	UNE-400
Laser Particle Size Analyzer (LPSA)	Beckman Coulter	LS 230
Mounting Machine	Struers	CitoPress-1
Polishing Machine	Pace Technologies	NANO 2000T
X-ray Fluorescence Energy Dispersive Spectrometer (XRF)	PANalytical,	Zetium
X-ray Diffractometer (XRD)	Phillips	X' Pert MPD
Scanning Electron Microscopy (SEM)	FEI	Quanta 400
Energy-dispersive X-ray spectroscopy (EDX)	Oxford	ISIS 300
Vibratory sieve shaker	Fritsch	Analysette 3 Pro
Specimen cutting machine	K.V	K.V-Cut 20
Vicker Micro Hardness Tester	Matsuzawa	MMT-X7B

3.3 Experimental Procedure

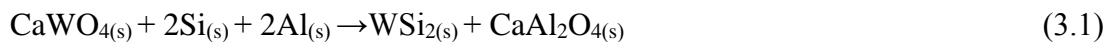
3.3.1 Preliminary Synthesis of the Tungsten Silicide Intermetallic Alloy

The procedure is theoretically approached to the synthesis and then follow the experiment to synthesis W-Si base intermetallic alloy. There are three types of reactant systems in this experiment work;

1. CaWO₄-Si-Al reactant system,
2. CaO-WO₃-Si-Al reactant system, and
3. WO₃-Si-Mg reactant system.

3.3.1.1 CaWO₄-Si-Al Reactant System

This reactant system is the combination of Scheelite Mineral (CaWO₄), Chiang Mai Mining Co., Ltd., Thailand, Silicon lump (Si) and Aluminium powder (Al). The theoretical mole balance and the chemical equation are shown in Eq. (3.1).



Firstly, the mole ratio and weight ratio of the reaction calculated from the chemical equation and their proportion is shown in Table 3.4. The proportion of this result is based on the assuming of WO₃ 100 %wt in CaWO₄ but the actual weight percentage of the WO₃ in CaWO₄ by XRF result is 84.098 % wt as shown in Table 3.5. The actual net weight also calculated by their wt% in CaWO₄ and listed in Table 3.4.

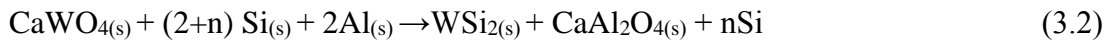
Table 3.4. The ratio of the reactants used in Eq. 3.1.

	Reactants		
	CaWO ₄	Si	Al
Mole Ratio	1	2	2
Weight Ratio	5.34	1.04	1
Net Weight of 25 g	18.08	3.53	3.39
Net Weight of 25 g by actual WO ₃ wt%	17.31	3.53	3.39

Table 3.5. The XRF result of scheelite (CaWO_4) minerals.

Compound	Mass Fraction or (%wt)
WO_3	84.09
CaO	13.37
TiO_2	0.06
Cr_2O_3	0.03
Fe_2O_3	0.06
Rb_2O	0.02
ZrO_2	2.33
PdO	0.04

Moreover, the optimum WSi_2 weight percentage can get by adding the amount of ($n=0.5$) mole of Si in Eq. (3.2). The calculated mole ratio, weight ratio, and net weight ratio are shown in Table 3.6.

**Table 3.6.** The ratio of the reactants used in Eq. (3.2).

	Reactants		
	CaWO_4	Si	Al
Mole Ratio	1	2.5	2
Weight Ratio	5.34	1.30	1
Net Weight of 25 g	17.47	4.26	3.27
Net Weight of 25 g by actual WO_3 wt%	16.72	4.26	3.27

3.3.1.2 CaO- WO_3 -Si-Al Reactant System

This reactant system is the combination of commercial calcium oxide (CaO), tungsten oxide (WO_3), silicon lump (Si) and aluminum powder (Al). The theoretical mole balance and the chemical equation are shown in Eq. 3.3. The mole ratio and weight

ratio of the reaction are calculated from the chemical equation and their proportion is shown in Table 3.7.

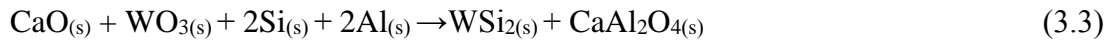


Table 3.7. The ratio of the reactants used in Eq. (3.3).

	Reactants			
	CaO	WO ₃	Si	Al
Mole Ratio	1	1	2	2
Weight Ratio	1.04	4.29	1.04	1
Net Weight of 25 g	3.52	14.56	3.53	3.39

3.3.1.3 WO₃-Si-Mg Reactant System

This reactant system is the combination of Tungsten Oxide (WO₃), Silicon lump (Si) and Magnesium powder (Mg) as a fuel. The theoretical mole balance and the chemical equation are shown in Eq.(3.4). The mole ratio and weight ratio of the reaction are calculated from the chemical equation and their proportion is shown in Table 3.8.

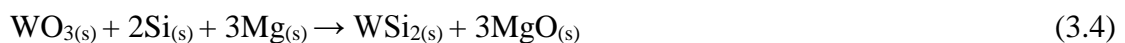


Table 3.8. The ratio of the reactants used in Eq. (3.4).

	Reactants		
	WO ₃	Si	Mg
Mole Ratio	1	2	3
Weight Ratio	3.18	0.77	1
Net Weight of 25 g	16.06	3.89	5.05

3.4 Preparing the Green Pellet

The particle size of the raw scheelite- CaWO_4 ($\sim 300 \mu\text{m}$) and calcium oxide combined with tungsten oxide- $(\text{CaO}+\text{WO}_3, \sim 45 \mu\text{m})$ were reduced by a laboratory-scale planetary ball mill (Fritsch GMBH. Pulverisette-6, Germany) at a rotational speed of 250 rpm for various milling times (0.5, 2, 4, and 8 hr). The milled products were analyzed by LPSA (laser particle size analyzer, LS230, COULTER, USA) and the sizes obtained are listed in Table 3.9.

Table 3.9. Properties of the milled reactant powders.

High Energy Milling Time (hr)	The particle size of CaWO_4 (μm)	The particle size of $\text{CaO}+\text{WO}_3$ (μm)
0.5	40.09	5.69
2	12.03	5.08
4	5.71	5.01
8	4.12	4.53

The raw materials were weighed according to stoichiometric requirements of the reaction formulas (3.1), (3.2), (3.3) and (3.4) with a net weight of 25 g, respectively. Then, the reactants powders were mixed in a jar of zirconia balls (ZrO_2) at room temperature for 2 hr. The obtained mixture was uniaxially pressed (Huat Seng-1939-15T, Thailand) to 25.4 mm diameter and about 20 mm height cylindrical pellets at 0.5 MPa with green density in the range of 50-60% compared with theoretical density as shown in Figure 3.2.

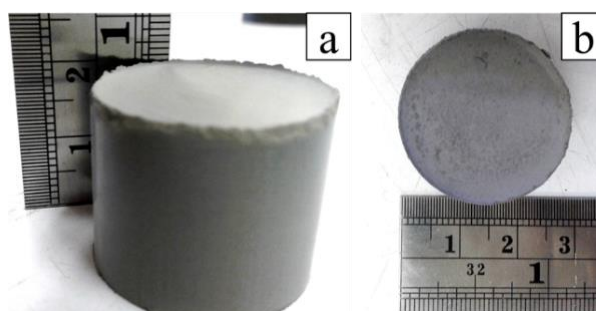


Figure 3.2. Digital photographs of green pellet sample before SHS (a) side view and (b) top view.

3.5 Preparing the Graphite Mold

In their early studies, the authors T. Chanadee et al. and S. Niyomwas et al. described the formation of tungsten intermetallic compounds (WSi_2 , W_2B) by SHS [16]. They described that the used of graphite plate can reduce the rapid loss of heat during synthesis and also enforce phase separation between compounds by varying the different density.

There are three types of graphite plate with 70 x 70 x 10 mm square for SHS process and is shown in Figure 3.3. The first graphite plate is 40 ° angle with a diameter of 25.4 mm and a hole in the middle with a diameter of 15 mm. The second plate is with a hole at the centered with a diameter of 15 mm. The last plate is only a square graphite plate without a hole.

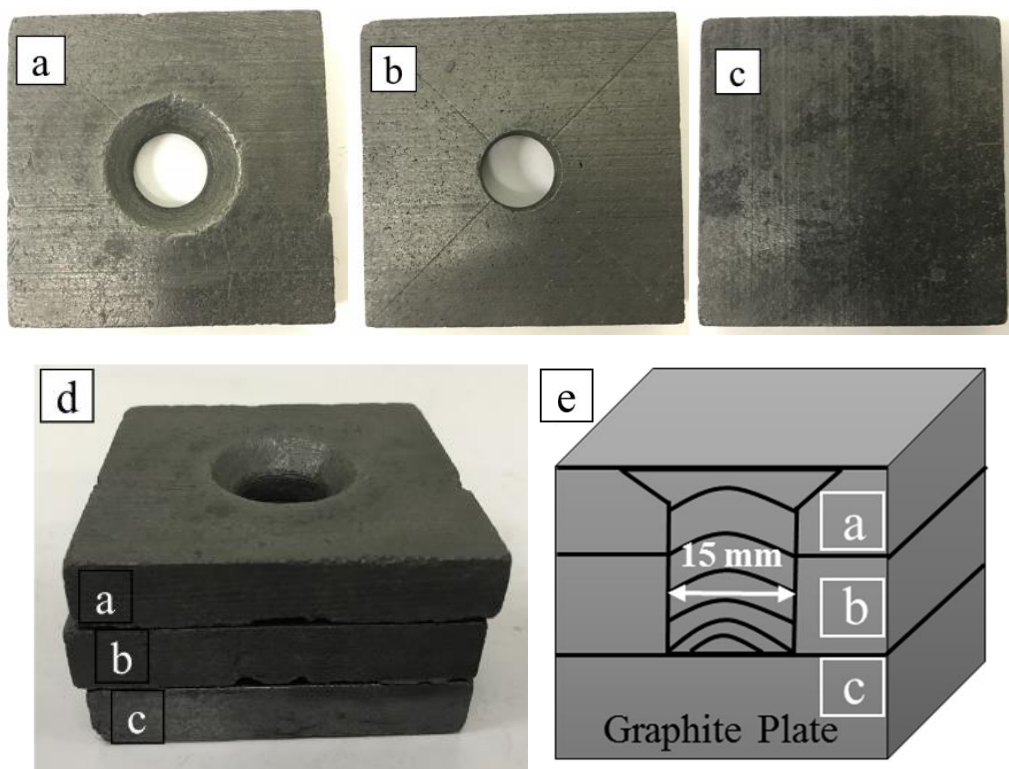


Figure 3.3. Digital photograph of the design of graphite molds used in experiment (a), piece 1 (b), piece 2, (c) piece 3, (d) the stacked condition of all pieces, and an illustration of a cross-section of (d).

3.6 Preparing the Sand Mold

By researching relevant research, the authors T. Chanadee et al. described the phase separation of an oxide ceramic and intermetallic compounds on using quartz tube mold, and effects of Ar pressure assist in high densification combustion synthesis [16]. It was found that the use of quartz tube can make compatible bonding with scintillation oxide slag or by-product SiO_2 . Compatibility and bonding can be able to trap the scale slag and oxide phase out from the metal compound.

However, the cost of the quartz pipe is quite high. Therefore, there is need to substitute relevant materials and efficiency equivalent to the quartz tube. The equivalent nature and plentiful of SiO_2 in naturally is sand. The naturally sand is available in various sources and the main element is SiO_2 . The natural sand was prepared and fabricated as a mold to apply instead of the quartz tube.

Table 3.10. XRF results of natural sand.

Elements	Mass Fraction (wt%)
SiO_2	97.16
Na_2O	1.44
Fe_2O_3	0.53
Al_2O_3	0.21
Trace elements	Balance

Firstly, the natural sand was collected from Hat Kaew area, Singhanakorn district, Songkhla province. Then, it will be examined by X-ray composition by XRF technique and detailed is shown in Table 3.10.



Figure 3.4. Vibratory sieve shaker.

Natural sand is sieved by vibratory sieve shaker as shown in Figure 3.4 and measured particle size in the range of about 100 μm . Then the resulted sand is dried in the oven at 80 $^{\circ}\text{C}$ for overnight. Then the sand 40 g is mixed with 10 ml of Na_2SiO_3 solution (4:1 volume ratio) as a binder and the mixture was put into a hollow cylindrical steel mold. The steel mold and die were uniaxially pressed (Huat Seng-1939-15T, Thailand) at 5 MPa to form 10 mm thick, 26 mm diameter, and about 25 mm height hollow tube. The resulted sand mold was fired in the normal atmosphere with temperature at 200 $^{\circ}\text{C}$ for 24 hours and the fired sand mold is shown in Figure 3.5.

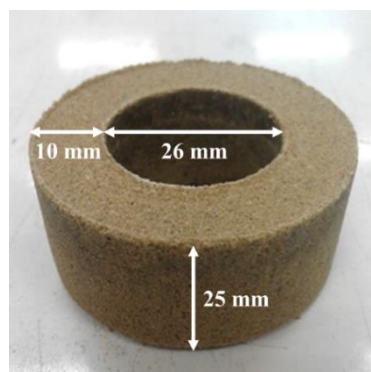


Figure 3.5. Hollow sand mold after firing at 200 $^{\circ}\text{C}$ for 24 hours.

3.7 Synthesis of Tungsten Silicide Intermetallic without Sand Mold

The graphite plates in section 3.5 were set in order by plate 3 to 1 which is shown in Figure 3.4. The cylindrical pellet for all reaction in (3.1), (3.2), (3.3) and (3.4) was placed on three stacked graphite plates which are shown in Figure 3.6. Then, the cylindrical pellet and graphite plates were transferred to the SHS reactor and placed on a movable graphite plate which is inside the SHS reactor. The SHS reactor was evacuated to the reduced pressure level of 70 mmHg for 5 min and then filled with Argon gas up to a pressure of 0.5 MPa. To ensure an inert atmosphere inside the SHS reactor for the actual reactions during synthesis, the evacuated and filled with Argon gas process was repeated at least twice.

The experimental setup is schematically presented in Figure 3.7. It consisted of an SHS reaction chamber which is connected with a vacuum pump and argon gas tank to control the atmosphere of the reactor. The SHS reactor inserted moveable tungsten

filament (W) and connected to a power source through a current controller, which provides the energy required for igniting the reaction. The sample is heated locally on the top surface by a tungsten filament. During SHS reaction, the heat liberates simultaneously by self-propagated the sample and combustion front travels another side of the sample. When the SHS reaction finished, the pressure inside the reactor is released along with the dust into the trapping system which put into the water as a bubble. Then, the product was allowed to cool to room temperature and then taken out of the reactor.

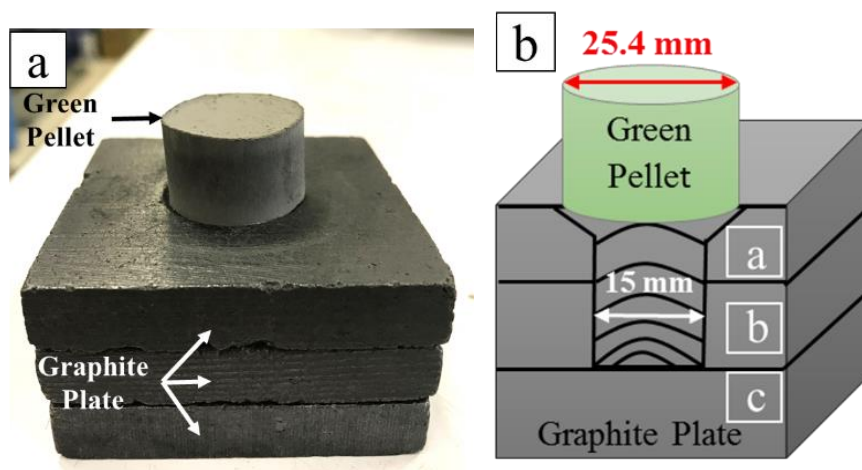


Figure 3.6. Preparing of the sample on top of stacked graphite plates without sand mold (a) digital photograph, and (b) illustration of a cross-section of (a).

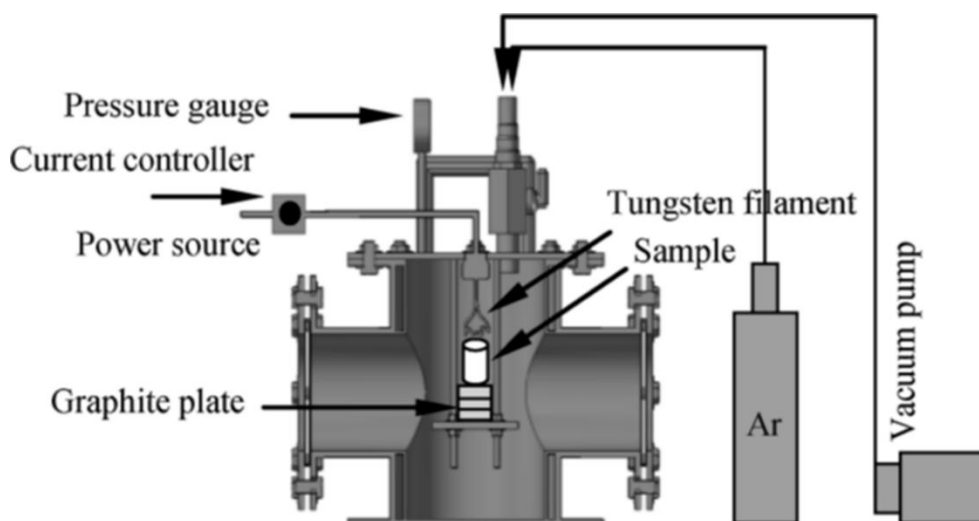


Figure 3.7. A schematic of the experimental setup without sand mold [7].

3.7.1 A Study on the Influence of SHS on the Reduction of Heat Loss during the Shear Process

Although the intermetallic alloy produced by SHS process, the as-SHS product contained a large amount of impurity from oxide slag. In the real situation, when SHS reaction occurs, the reaction is subjected to a heat loss from the sample through the reaction front. Moreover, the rapid loss of heat results in incomplete the reactions. In other words, the product does not have enough time to complete the formation. Another effect is the splash of the sample caused by the release of pressure inside the reactor during the reaction. It also results in less substance synthesized products, as well.

3.8 Synthesis of Tungsten Silicide Intermetallic with Sand Mold

Once the sand mold has been prepared, before the SHS reaction, the cylindrical pellets will be placed on three layers of graphite and covered with prepared sand mold as shown in Figure 3.8. Then proceed as the same in section 3.7 and the experimental set up is shown in Figure 3.9.

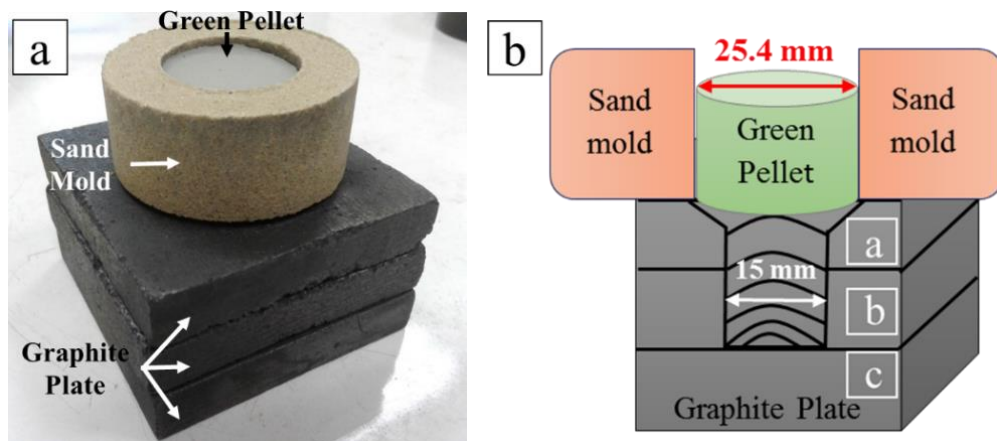


Figure 3.8. Preparing of the sample on top of stacked graphite plates with sand mold (a) digital photograph, and (b) illustration of a cross-section of (a).

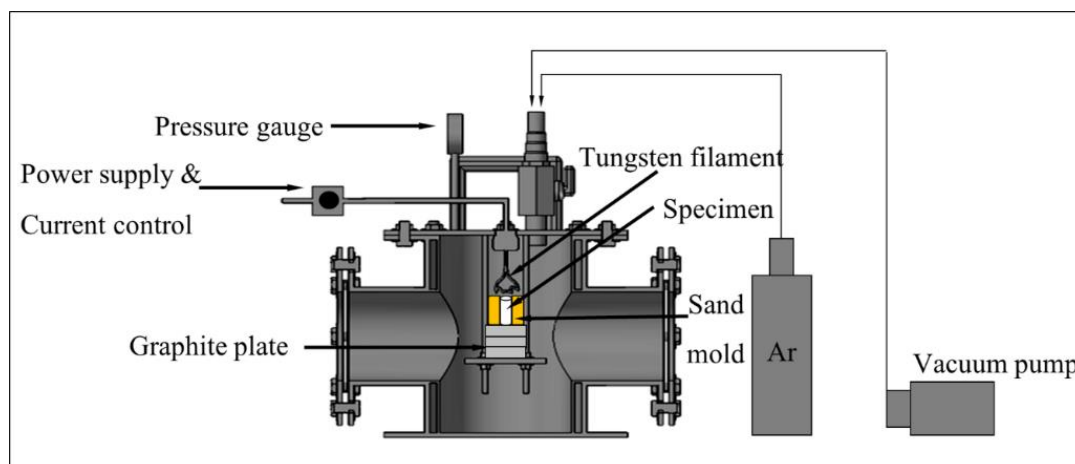


Figure 3.9. A schematic of the experimental setup with sand mold [19].

3.9 Characterization Methods

3.9.1 X-ray Fluorescence Spectrometer

The chemical composition of the as-received scheelite mineral and natural sand were identified by X-ray fluorescence spectrometer (XRF, PANalytical, Zetium, UK).

3.9.2 X-ray Diffraction

The phases and crystalline structures of resulting products were identified by powder X-ray diffraction (XRD, X'Pert MPD, PHILIPS, the Netherlands). Spectra were recorded at 30 mA and 40 kV, using Ni-filtered Cu-K α radiation, $\lambda=1.54 \text{ \AA}$. The scan rate (2θ) was $3^\circ/\text{min}$ with a step size of 0.05.

3.9.3 Scanning Electron Microscope

Morphologies and elemental analysis of resulting products were observed by a scanning electron microscope (SEM, Quanta 400, FEI, USA), coupled with an energy dispersive X-ray spectrometer (EDX, ISIS 300, Oxford, England).

3.10 Semi-quantitative Analysis Method

Determining the weight percentage of the amount of compound of each phase were analyzed by the semi-quantitative method. The semi-quantitative method is based on the calculation of the XRD pattern of the individual compounds. The equation is shown in Eq. (3.5).

$$R_x = \frac{A_x}{A_x + A_y + A_z} \times 100\% \quad (3.5)$$

Where;

- R_x = the amount of the compound x
- R_y = the amount of the compound y
- R_z = the amount of the compound z
- A_x = the area under the graph of the compound x
- A_y = the area under the graph of the compound y
- A_z = the area under the graph of the compound z

3.11 Density Testing Method

The true density of the SHS products was measured by Archimedes' Principle and the bulk density and apparent porosity of the SHS products was measured by ASTM C373-88 standard [112]. Three representative test specimens were selected which are no cracks, sharp edges or corners.

3.12 Microstructure Examination

The specimens were prepared by metallurgical sample preparation methods for the study of the microstructure. The steps for specimen preparation were sectioning and cutting, mounting, rough polishing, final polishing, etching, microscopic analysis, and hardness testing [113, 114].

The specimens were sectioned by cutting machine (K.V.CUT-20) at 400 rpm to get the flat surface. The resulted specimens were mounted by (thermosets–phenolic)

which is encapsulating the specimens into a compression mounting compound. The specimens and phenolic were put into the compression mounting machine to form (12.7 mm height x 25.4 mm diameter) cylinder samples. The curing time is 5 min under 150 °-165 °C molding temperature and 21-28 MPa molding pressure.

The mounted samples were polished by metallurgical polishing machine. Silicon carbide (SiC) abrasives were used for planar grinding the surface of the specimens. The grit was sorted from rough numbers to sequential numbers. The rotary plate was rotated at 300-350 rpm. High napped polishing pads were used for final polishing step at a rotation speed of around 400 rpm, using a 1 µm diamond suspension. Then, specimens were cleaned with water and ethanol to remove grease and then dried with drier. The finished specimens were characterized by SEM and EDX.

3.13 Micro Hardness Testing

Microhardness of specimens was determined by Vicker micro hardness tester (High Wood, HWDM-3) under test load at 0.5 kgf (4.905 N) with 10 seconds soaking time. Vickers hardness number (HV) is calculated by dividing the applied load in kilogram-force by the surface area of the indentation and is express in Eq. (3.10). All values were got by pressing 3 points on each specimen.

$$\text{Vicker Hardness Number} = \frac{0.1891F}{d^2} \text{ MPa} \quad (3.10)$$

Where; F= the applied force - 0.5 kgf (4.905 N)
d= the mean value of the distance between the two diagonals of the indentation (mm)

Chapter 4

Results and Discussion

4.1 Two Reactant Systems for Self-Propagating High-Temperature Synthesis of Tungsten Silicide

In this study, tungsten silicide (WSi_2) intermetallic was synthesized by SHS from two alternative reactant powders, namely from scheelite mineral ($CaWO_4$) and from pure oxide ($CaO-WO_3$) reacted with Si and Al. The objectives of this research were three folds; (i) comparison of purity of as-SHS WSi_2 intermetallic from the two alternative raw materials, (ii) investigation of the effects of sand mold on phase separation of the oxide slag, and (iii) determining optimal combustion synthesis conditions for high yield of dense WSi_2 intermetallic by control of Si proportion in the reactant system. Also, the product microstructures, phase compositions, density, and microhardness were investigated.

4.1.1 Particle Size of Reactants

The raw materials powders of $CaWO_4$ and $CaO + WO_3$ were grinded with a high-energy milling machine. A laboratory-scale planetary ball mill at a rotational speed of 250 rpm was used in this work for various milling times (0.5, 2, 4, and 8 hr). The milled products were analyzed by laser particle size analyzer (LPSA) and the mean value of the size obtained are listed in Table 4.1.

Table 4.1. Properties of the milled reactant powders.

High Energy Milling (HEM) Time (hr)	The mean particle size of $CaWO_4$ (μm)	The mean particle size of $CaO+WO_3$ (μm)
0.5	40.09	5.69
2	12.03	5.08
4	5.71	5.01
8	4.12	4.53

4.1.2 Thermodynamic Analysis

Initially, the thermodynamic feasibility of the synthesis process was examined. The Gibbs energy minimization method was used to calculate the equilibrium concentrations of stable species produced by the SHS process. The evolution of each species was estimated for the temperature range of 0–4500 °C under reducing atmosphere conditions. The total Gibbs energy of the system is expressed in Eq. (4.1). The calculated n_i minimizes G subject to mass balance constraints.

$$G = \sum n_i (g_i^0 + RT \ln P_i) + \sum n_i g_i^0 + \sum n_i (g_i^0 + RT \ln P x_i + RT \ln \gamma_i) \quad (4.1)$$

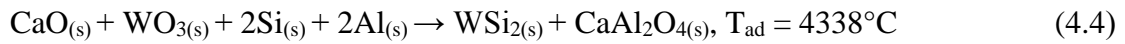
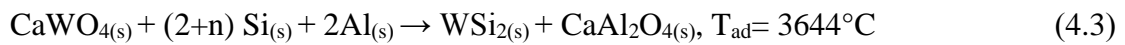
Where; G = the total Gibbs energy of the system,
 g_i^0 = the standard molar energy,
 P = the partial pressure,
 x = the molar fraction,
 γ = the activity coefficient, and
 i = the species.

The enthalpy of the reaction was used to calculate the adiabatic temperature (T_{ad}) of the SHS reaction. The adiabatic temperature (T_{ad}) is the maximum theoretical temperature that the reactants can reach, and it is determined from Eq. (4.2). This equation applies to phase changes occurring between the initial temperature and T_{ad} .

$$\Delta H = \int_{298}^{T_m} C_{p, \text{solid}} dT + \Delta H_f + \int_{T_m}^{T_{ad}} C_{p, \text{liquid}} dT \quad (4.2)$$

Where; ΔH = the reaction enthalpy,
 T_m = the melting temperature,
 C_p = the specific heat capacity,
 ΔH_f = the enthalpy of transformation, and
 T_{ad} = the adiabatic temperature.

It has been accepted that self-sustained combustion is feasible when the adiabatic temperature of reaction exceeds 1800°C [70, 71, 80]. The calculated T_{ad} for the overall reactions in Eq. (4.3) and (4.4) are 3644°C and 4338°C, and these are clearly higher than 1800°C, so the reactions can support self-sustained combustion. The adiabatic temperatures and equilibrium compositions were calculated for the reactions Eqs. (4.3) and (4.4) using the HSC[®] program, based on Gibbs energy minimization [115].



Here, n is the amount of added mole ratio of Si for scheelite reactant system.

4.1.2.1 Thermal Analysis for CaWO₄-Si-Al reactant System

The adiabatic temperatures and equilibrium compositions result for CaWO₄-Si Al system are shown in Figure 4.1, with the expected products WSi₂ and the oxide phases of CaAl₂O₄ and Al₂O₃. The intermetallic phase of WSi₂ formed about 1500°C and the oxide phase of CaAl₂O₄ formed about 2000°C when the amount of reactants were decreased.

In this aluminothermic SHS reaction, CaWO₄, Si, and Al may have interacted to form some possible elements, compounds, and gases as presented in the following possible intermediate chemical reactions in Eq. (4.5) to (4.11), respectively. The thermodynamic calculation in the relation between temperature and theoretical Gibbs energy (ΔG) performed using HSC[®] chemistry program, illustrated in Figure 4.2.

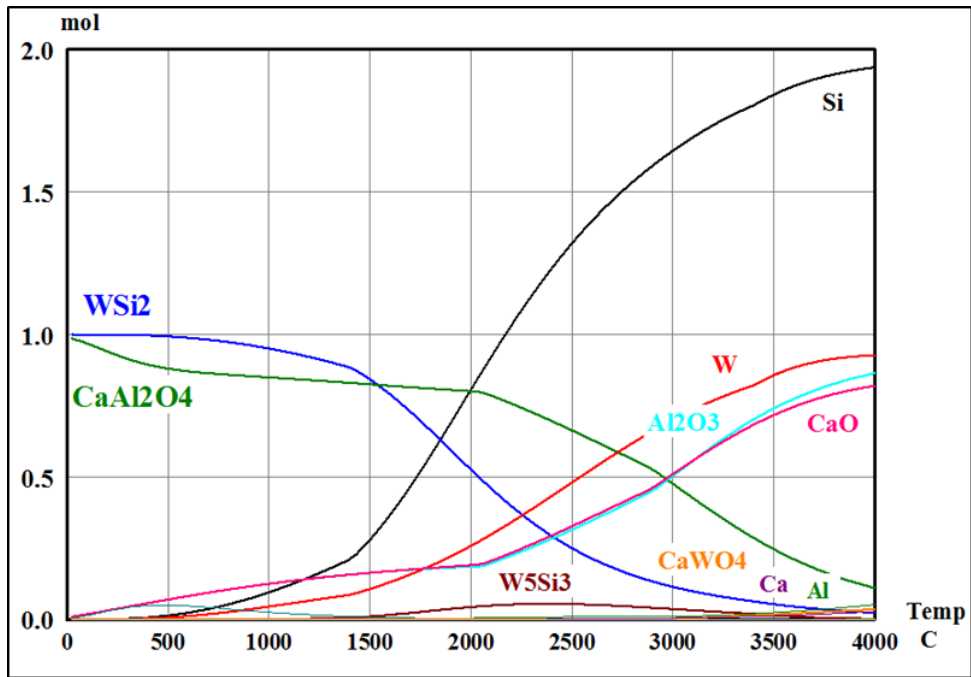


Figure 4.1. Equilibrium compositions of CaWO_4 -Si-Al reactant systems in inert Ar atmosphere.

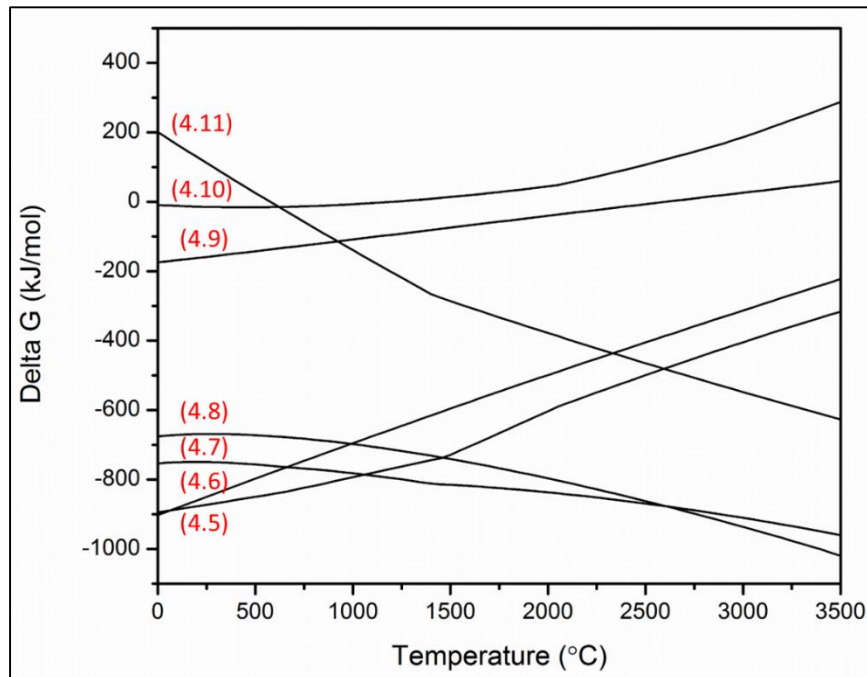
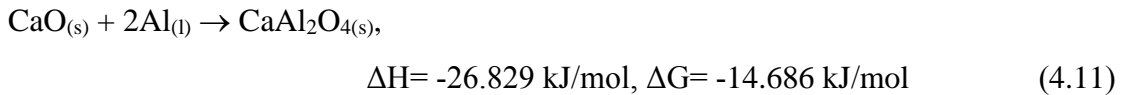
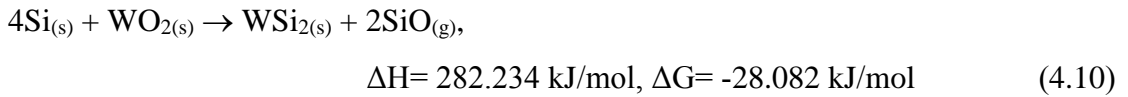
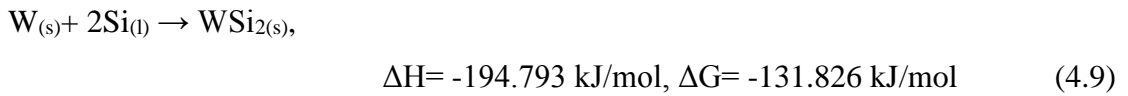
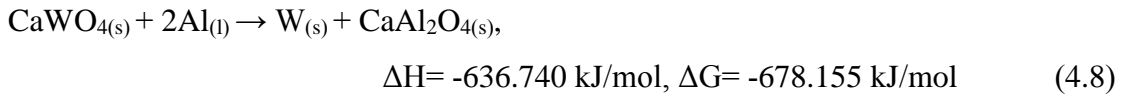
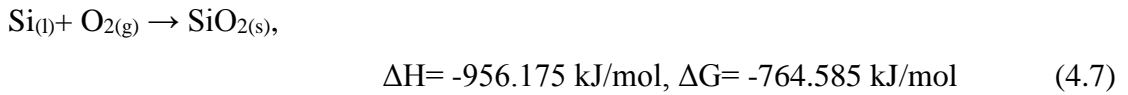
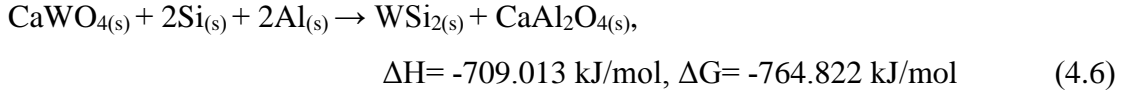
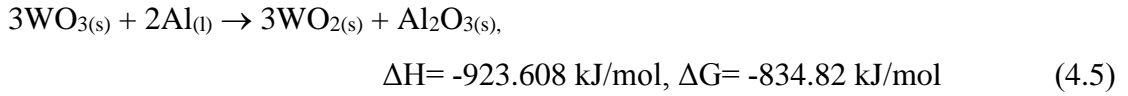


Figure 4.2. The relation between temperature and Gibbs energy of reactions under Argon gas atmosphere for CaWO_4 -Si-Al reactant system at a temperature range from 0 to 3500 °C.



During SHS reaction, all the reactants were in the solid state. When the reaction temperature reached the ignition temperature (T_{ig}) of Al (660°C), the CaWO₄ and Si were first surrounded by melted Al. Then, the reduction reaction of CaO, WO₃, and CaWO₄ with Al occurred as mentioned in Eqs. (4.5), (4.8) and (4.11) and hence formed Al₂O₃ and CaAl₂O₄. Some melted Si reacted with O₂ and formed SiO₂ phase in Eq. (4.7). The possible reaction for the intermetallic phase of WSi₂ was formed in the stage of reaction Eq. (4.9) and (4.10).

4.1.2.2 Thermal Analysis for CaO-WO₃-Si-Al reactant System

The adiabatic temperatures and equilibrium compositions result for CaO-WO₃-Si Al system are shown in Figure 4.3. It can be seen in Figure 4.3, the expected products WSi₂ with the oxide phases of CaAl₂O₄ and Al₂O₃. The intermetallic phase of WSi₂ formed at about 4000°C and the oxide phase of CaAl₂O₄ formed at about 1500°C when the amount of reactants were decreased.

In this aluminothermic SHS reaction, CaO, WO₃, Si, and Al may have interacted to form some possible elements, compounds, and gases as presented in the following

possible intermediate chemical reactions in Eq. (4.12) to (4.16), respectively. The thermodynamic calculation in the relation between temperature and theoretical Gibbs energy (ΔG) performed using HSC[®] chemistry program, illustrated in Figure 4.4.

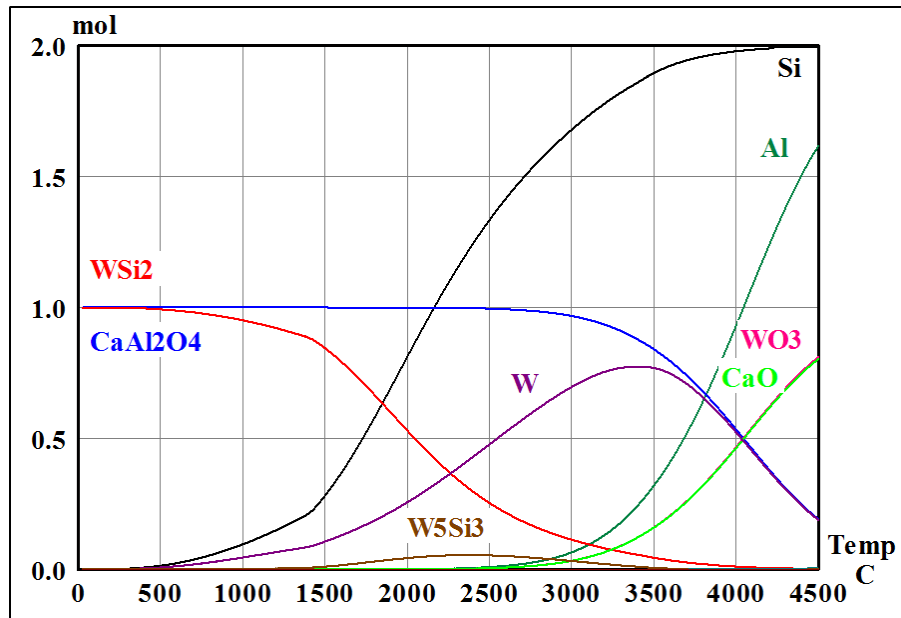


Figure 4.3. Equilibrium compositions of CaO-WO₃-Si-Al reactant systems in inert Ar atmosphere.

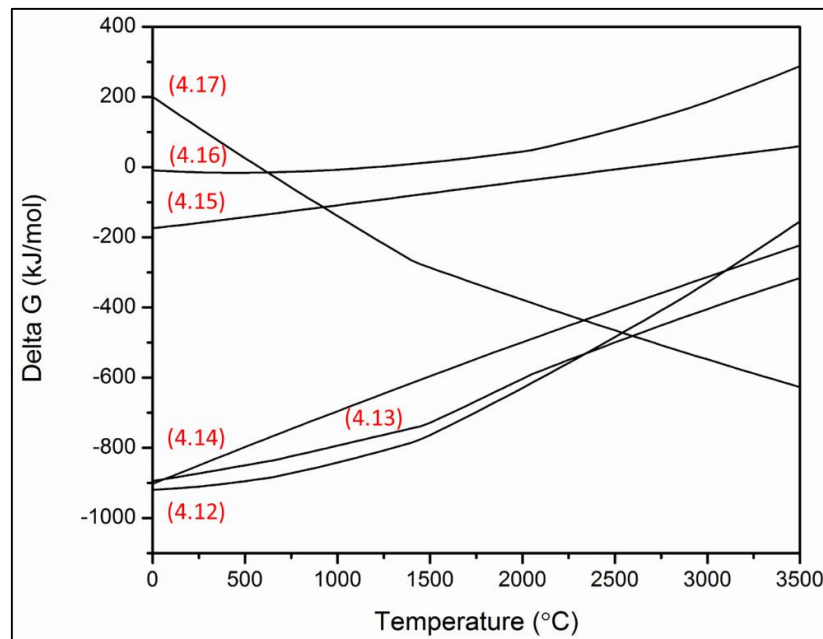
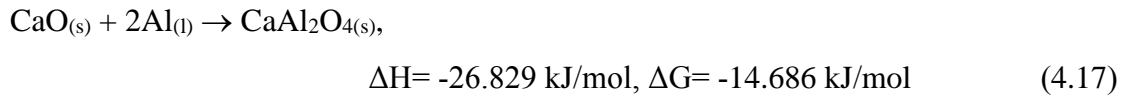
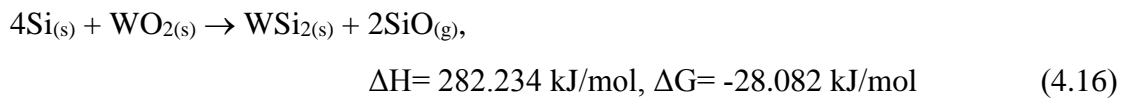
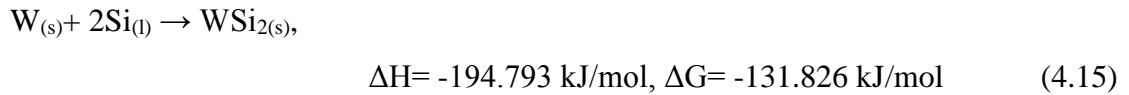
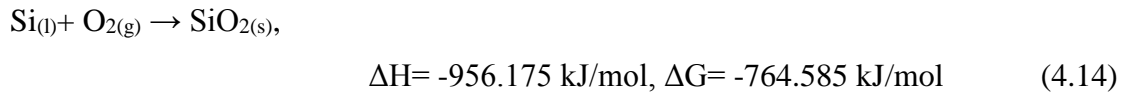
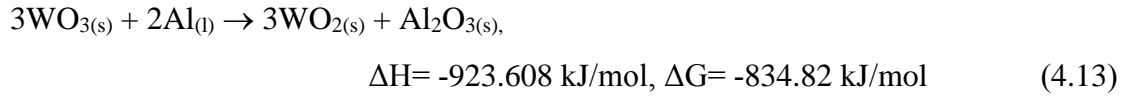
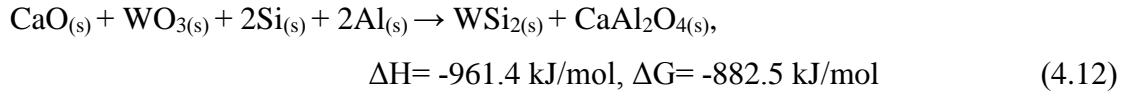


Figure 4.4. The relation between temperature and Gibbs energy of reactions under Argon gas atmosphere for CaO-WO₃-Si-Al reactant system at a temperature range from 0 to 3500 °C.



As mentioned in section 4.1.2.1, all the reactants were in a solid state when the ignition is started. When the reaction temperature reached the ignition temperature (T_{ig}) of Al (660°C), the CaO, WO_3 , and Si were first surrounded by melted Al. Then, the reduction reaction of CaO and WO_3 with Al were occurred as shown in Eq (4.13) and (4.17) and hence formed Al_2O_3 and CaAl_2O_4 . Some melted Si reacted with O_2 and formed SiO_2 phase in Eq. (4.14). The possible reaction for the intermetallic phase of WSi_2 has formed in the stage of reaction Eq. (4.15) and (4.16).

4.1.3 Characterization of the Intermetallic Product

4.1.3.1 Characterization of the CaWO_4 -Si-Al Reactant System

Phase compositions of the products from the reactions (4.3) was analyzed by XRD. Figure 4.5 shows the XRD patterns of the products from the reactions of CaWO_4 -Si-Al mixture high-energy milled for various times. The peaks indicate the presence of a major WSi_2 phase (JCPDF No. 01-074-1149) and minor residual phases of pure W (JCPDF No. 03-065-6453), Si (JCPDF No. 00-027-1402), Al (JCPDF No. 01-071-4624), and an intermediate phase of CaSi_2 . The CaSi_2 (JCPDF No. 00-047-1518) intermediate phase was trapped by the rapid cooling and solidification. The high-energy

milling decreased particle size of the CaWO_4 used, but this had only small effects on XRD patterns of the products. The comparative phase compositions of the as-synthesized products for both systems were calculated by a semi-quantitative method [116, 117] which mentioned in section 3.10.

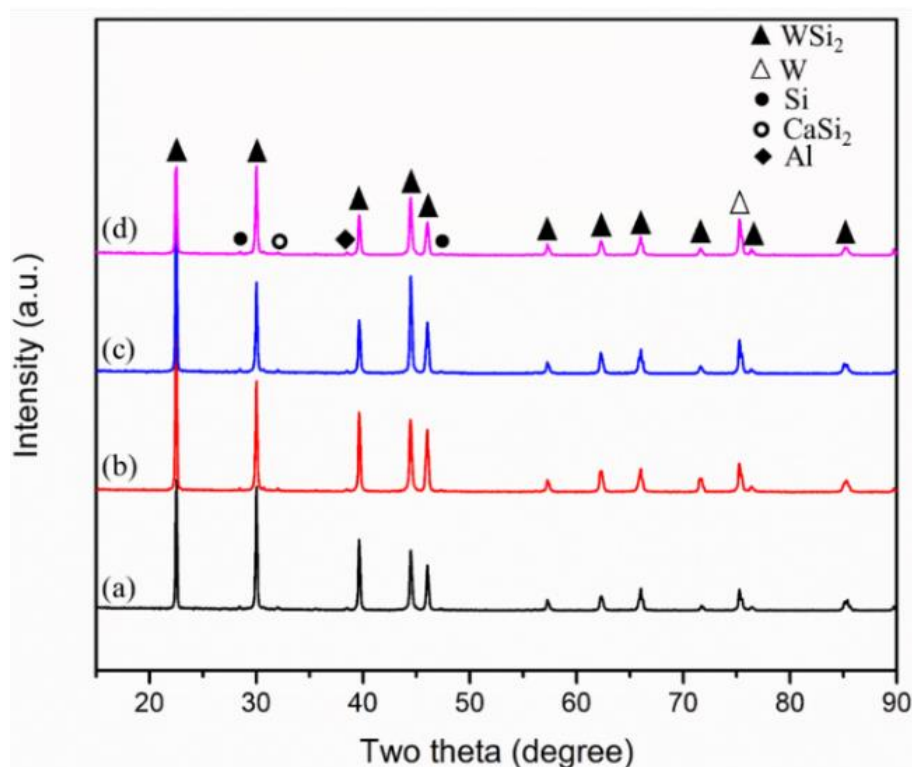


Figure 4.5. XRD patterns of WSi_2 intermetallic products from CaWO_4 -Si-Al reactant system obtained with the milling times (a) 0.5, (b) 2, (c) 4, and (d) 8 hr.

Table 4.2. Semi-quantitative analysis results from XRD results of (CaWO_4 -Si-Al) reactant system with ($n = 0$) Si mole.

Si used (mole) (2+n)	High-Energy Milling Time (hr)	Semi-quantitative measurement Wt (%)				
		WSi_2	W	Si	Al	CaSi_2
n = 0	0.5	95.55	2.83	0.56	0.38	0.27
n = 0	2	95.42	3.72	0.33	0.39	0.23
n = 0	4	94.07	4.16	0.89	0.42	0.17
n = 0	8	92.37	6.43	0.31	0.41	0.48

The weight percentages result from the semi-quantitative analysis is listed in Table 4.2. The weight percentages from this semi-quantitative analysis show that WSi_2 content decreased from 95.55% through 95.42% and 94.07% to 92.37% as milling time increased from 0.5 through 2 and 4 to 8 hr. It can be seen that when the weight percentages of WSi_2 decreased, the weight percentages of W in the system increased. It can be supposed that the lack of Si in the system to react with free W.

To compensate the reaction balance more towards WSi_2 , 0.5 mole Si level was used with Eq. (4.3) to react with the free W, and Figure 4.6 shows the XRD results. The semi-quantitative results for this conditions are listed in Table 4.3. While free W at $(2\theta) 75.2^\circ$ is seen for all conditions in Figure 4.5, that peak is missing in Figure 4.6 indicated completed reaction with the excess Si. The WSi_2 mass fractions, according to XRD semi-quantitative analysis, increased to 97.46%, 98.94%, 98.24% and 98.38%, respectively.

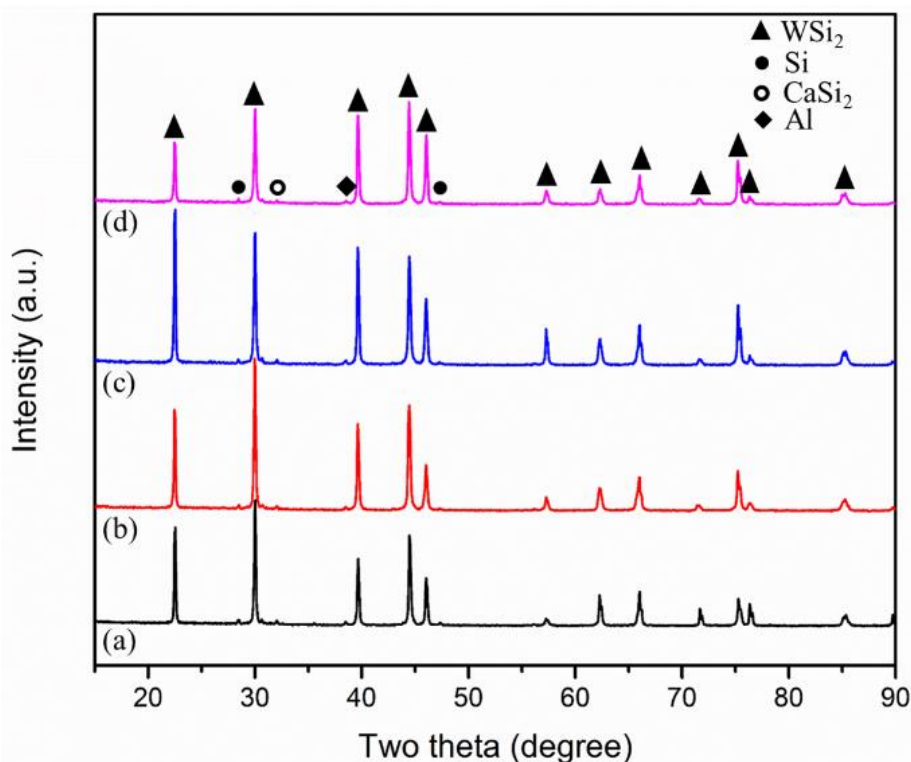


Figure 4.6. XRD patterns of WSi_2 intermetallic products from CaWO_4 -Si-Al reactant system with ($n=0.5$) moles Si obtained with the milling times (a) 0.5, (b) 2, (c) 4, and (d) 8 hr.

Table 4.3. Semi-quantitative analysis results from XRD results of (CaWO₄-Si-Al) reactant system with excess (n = 0.5) Si mole.

Si used (mole) (2+n)	High-Energy Milling Time (hr)	Semi-quantitative measurement Wt (%)					
		WSi ₂	W	Si	Al	CaSi ₂	SiO ₂
n = 0.5	0.5	97.46	0	1.09	0.50	0.44	0.51
n = 0.5	2	98.94	0	0.40	0.32	0.33	0.33
n = 0.5	4	98.24	0	0.31	0.53	0.45	0.46
n = 0.5	8	98.38	0	0.77	0.57	0.28	0.23

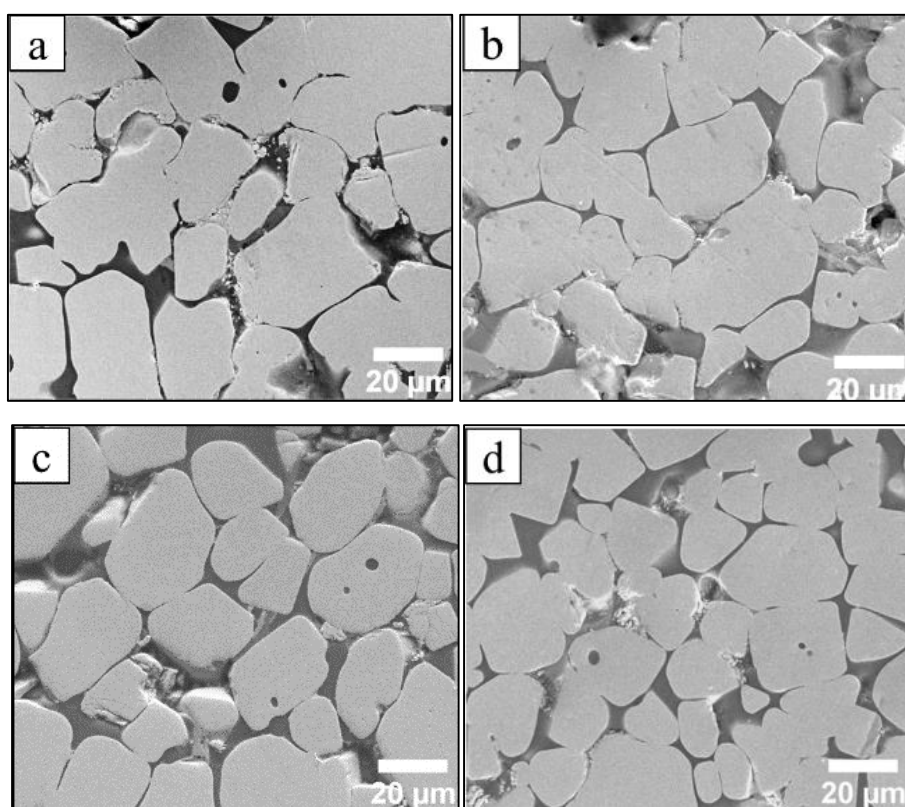


Figure 4.7. SEM microphotographs of WSi₂ intermetallic products from CaWO₄-Si-Al reactant system obtained with the milling times (a) 0.5, (b) 2, (c) 4, and (d) 8 hr.

Morphologies of the products were analyzed by SEM coupled with EDX. Figure 4.7 shows the cross-sectional microstructures of WSi₂ grains and boundaries from CaWO₄-Si-Al reactant system. The product had a continuous distribution of WSi₂

intermetallic grains, whose size decreased with high-energy milling time; and some holes which oxide phases of Al, W, Si and Ca were trapped by the rapid cooling and solidification. Phases were confirmed from EDX spectra as seen in Figure 4.8. The EDX mapping showed that the grains had distributed W and Si, while the pores between grain boundaries had some oxide phases of Al and Ca.

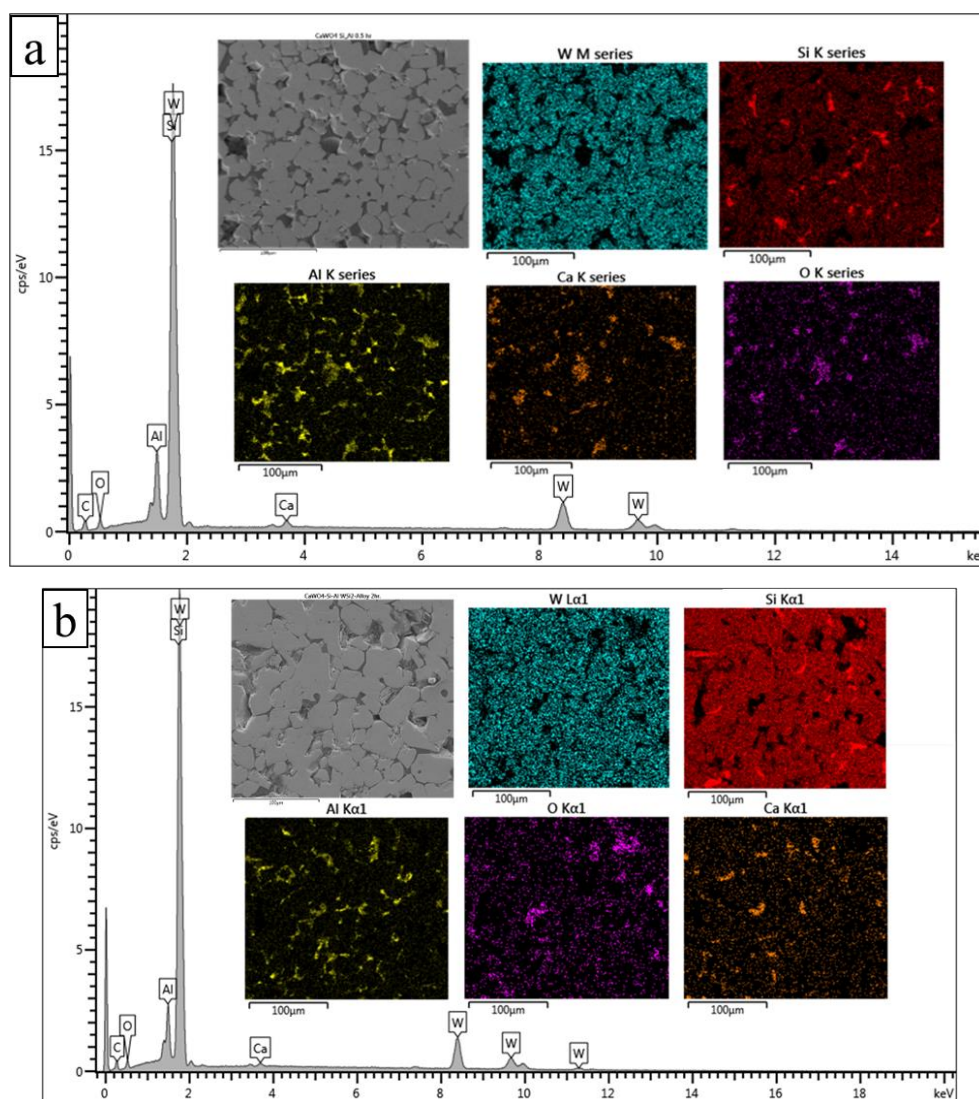


Figure 4.8. EDX analysis of WSi_2 intermetallic products from $CaWO_4$ -Si-Al reactant system obtained with the milling times (a) 0.5, (b) 2, (c) 4, and (d) 8 hr.

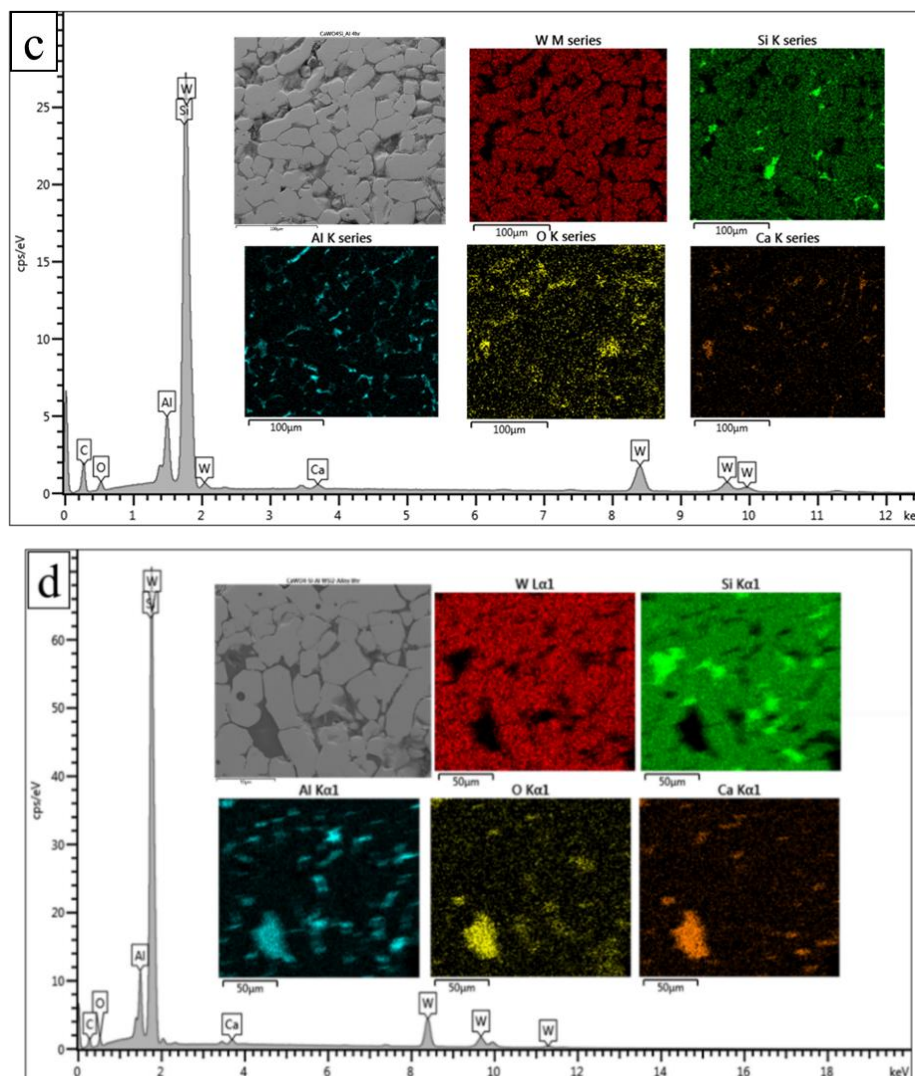


Figure 4.8. (cont.) EDX analysis of WSi_2 intermetallic products from $CaWO_4$ -Si-Al reactant system obtained with the milling times (a) 0.5, (b) 2, (c) 4, and (d) 8 hr.

4.1.3.2 Characterization of the CaO - WO_3 -Si-Al Reactant System

Figure 4.9 shows the XRD pattern of the products from the reactions of the CaO - WO_3 -Si-Al mixture. The peaks indicate the presence of a major WSi_2 phase (JCPDF No. 01-074-1149) and very small minor residual pure Ca (JCPDF No. 01-071-4107) present only in Figure 4.9(a). The weight percentages result from the semi-quantitative analysis is listed in Table 4.4. The XRD peaks by semi-quantitative analysis showed the mass fractions of WSi_2 as 99.7%, 99.9%, 99.9% and 99.9% for the varied high-energy milling times 0.5, 2, 4 and 8 hr. Moreover, the reaction for WSi_2

intermetallics was completed for this system and there is no need to add an excess amount of Si for this reactant system. However, the cross-sectional microstructures of WSi_2 grains and boundaries from $\text{CaO-WO}_3\text{-Si-Al}$ reactant system appeared similar except for the decreased grain size with increased milling time, see Figure 4.10. Moreover, the grains were more homogeneous and compact than those from $\text{CaWO}_4\text{-Si-Al}$ reactant system.

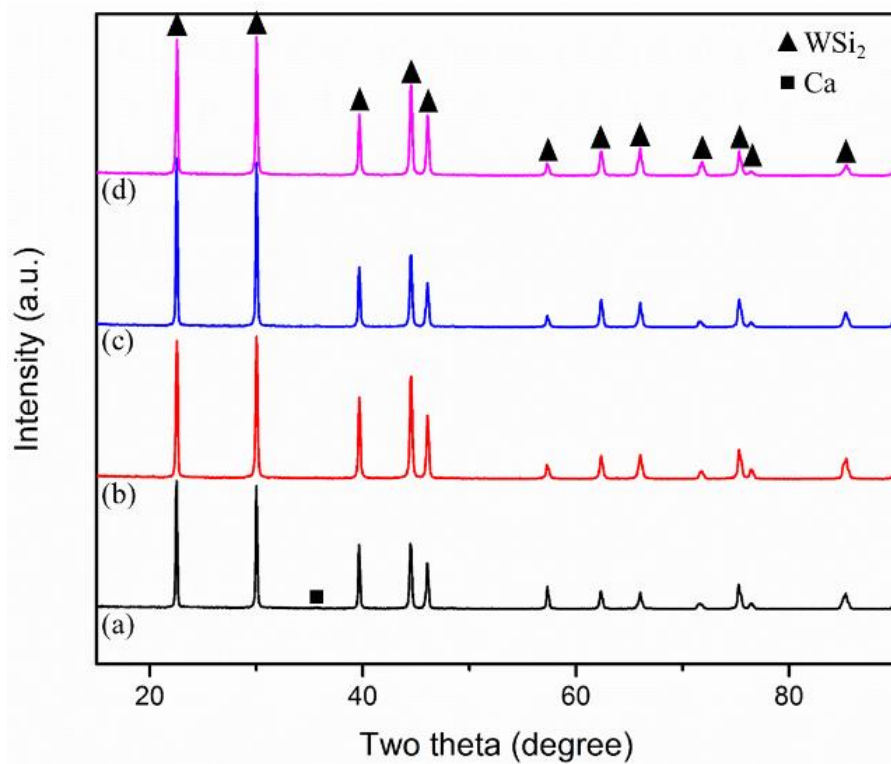


Figure 4.9. XRD patterns of WSi_2 intermetallic products from $\text{CaO-WO}_3\text{-Si-Al}$ reactant system obtained with the milling times (a) 0.5, (b) 2, (c) 4, and (d) 8 hr.

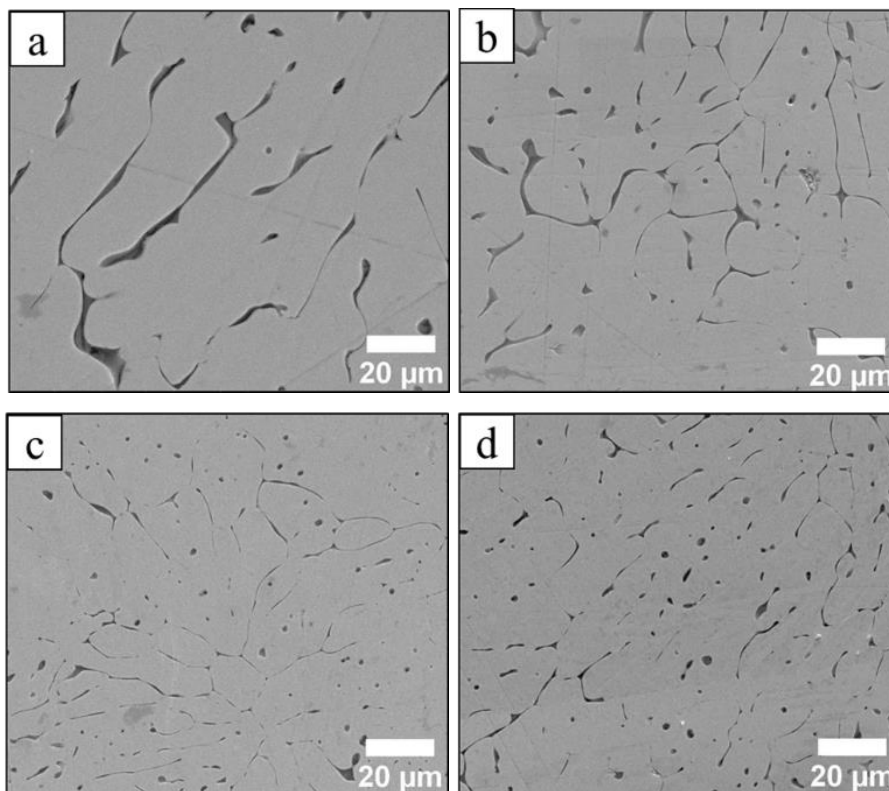


Figure 4.10. SEM microphotographs of WSi_2 intermetallic products from CaO- WO_3 -Si-Al reactant system obtained with the milling times (a) 0.5, (b) 2, (c) 4, and (d) 8 hr.

Table 4.4. Semi-quantitative analysis results from XRD results of (CaO- WO_3 -Si-Al) reactant system.

High-Energy Milling Time (hr)	Semi-quantitative measurement Wt (%)			
	WSi_2	W	Si	Ca
0.5	99.70	0	0	2.83
2	99.90	0	0	0.10
4	99.90	0	0	0.10
8	99.90	0	0	0.10

4.1.4 Mechanical Properties of the WSi_2 Intermetallic

The mechanical properties of the intermetallic for all conditions were investigated such as density, bulk density, apparent porosity, micro-hardness, and combustion wave, respectively.

4.1.4.1 Combustion Front Velocity of the WSi_2 Intermetallic

The different high energy milling time and combustion wave velocity are illustrated in Figure 4.11. It is evident that the relation between particle size of the green pellet and the combustion wave velocity. The combustion wave traveled faster when the particle size of the green pellet was smaller for (a) $CaWO_4$ -Si-Al reactant system [6, 71, 118]. The wave velocity dramatically decreased from 0.5 hr to 4 hr and increased again at 8 hr high energy milling time in the CaO- WO_3 -Si-Al reactant system.

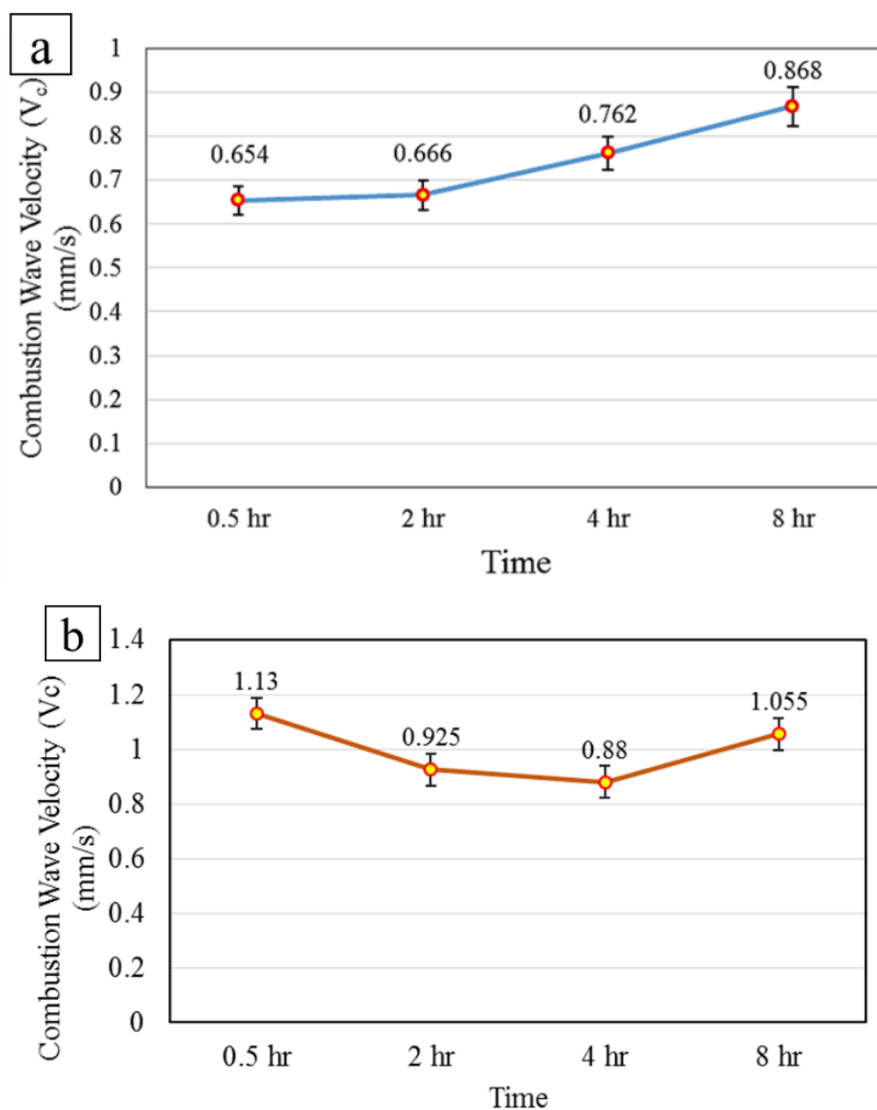


Figure 4.11. The effect of high energy milling time on the combustion wave velocity of the green pellet (a) $CaWO_4$ -Si-Al reactant system, and (b) CaO- WO_3 -Si-Al reactant system.

4.1.4.2 True Density of the WSi_2 Intermetallic

Figure 4.12 shows the calculated true density results of the WSi_2 intermetallic synthesized in different high energy milling time for two reactant systems. The maximum true density of 8.75 g/cm^3 was obtained in 8 hr for $CaWO_4$ -Si-Al reactant system. Based on the SEM results, combustion wave velocity and some literature [77, 119], the high combustion wave can reduce the inclusions and porosities during synthesis. It is one approach to obtain the dense of intermetallic in combustion synthesis. As a result, the density of the WSi_2 intermetallic increased when the milling time is increased for both systems. Moreover, the density values for CaO- WO_3 -Si-Al reactant system were more stable than $CaWO_4$ -Si-Al reactant system and all were higher than 7.2 g/cm^3 .

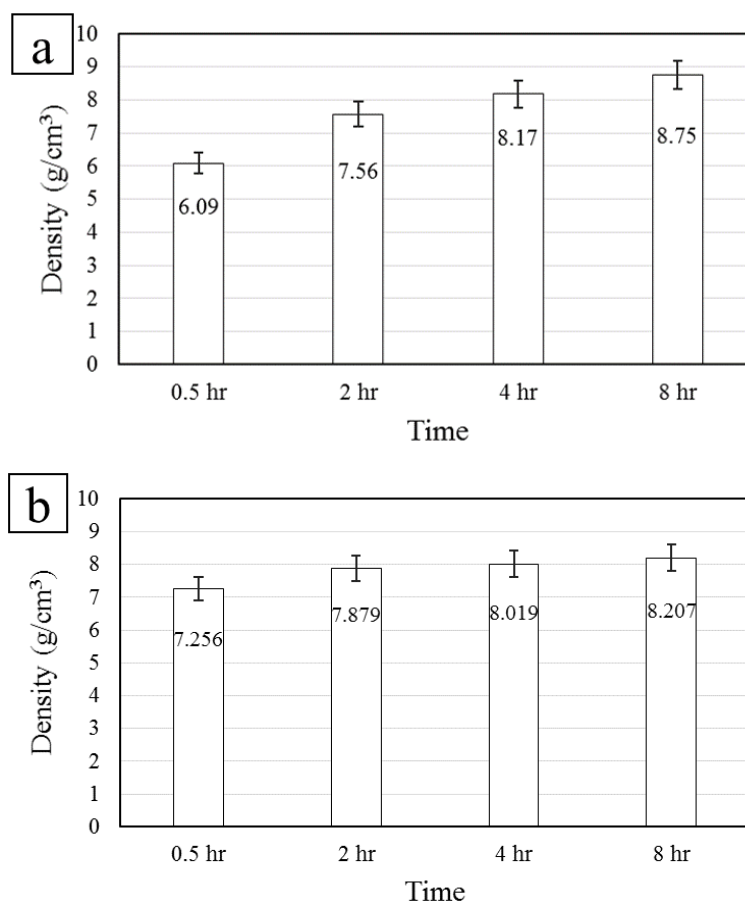


Figure 4.12. The effect of high energy milling time on the true density of the WSi_2 intermetallic (a) $CaWO_4$ -Si-Al reactant system, and (b) CaO- WO_3 -Si-Al reactant system.

4.1.4.3 Bulk Density of the WSi₂ Intermetallic

The calculated bulk density results of each product from two reactant systems are shown in Figure 4.13 (a, b). The bulk density decreased from 1.267 through 1.209 and 1.184 to 0.989 g/cm³ as milling time increased from 0.5 through 2 and 4 to 8 hr for CaWO₄-Si-Al reactant system. The bulk density decreased from 1.205 through 1.187 to 1.164 and increased again to 1.176 g/cm³ for CaO-WO₃-Si-Al reactant system.

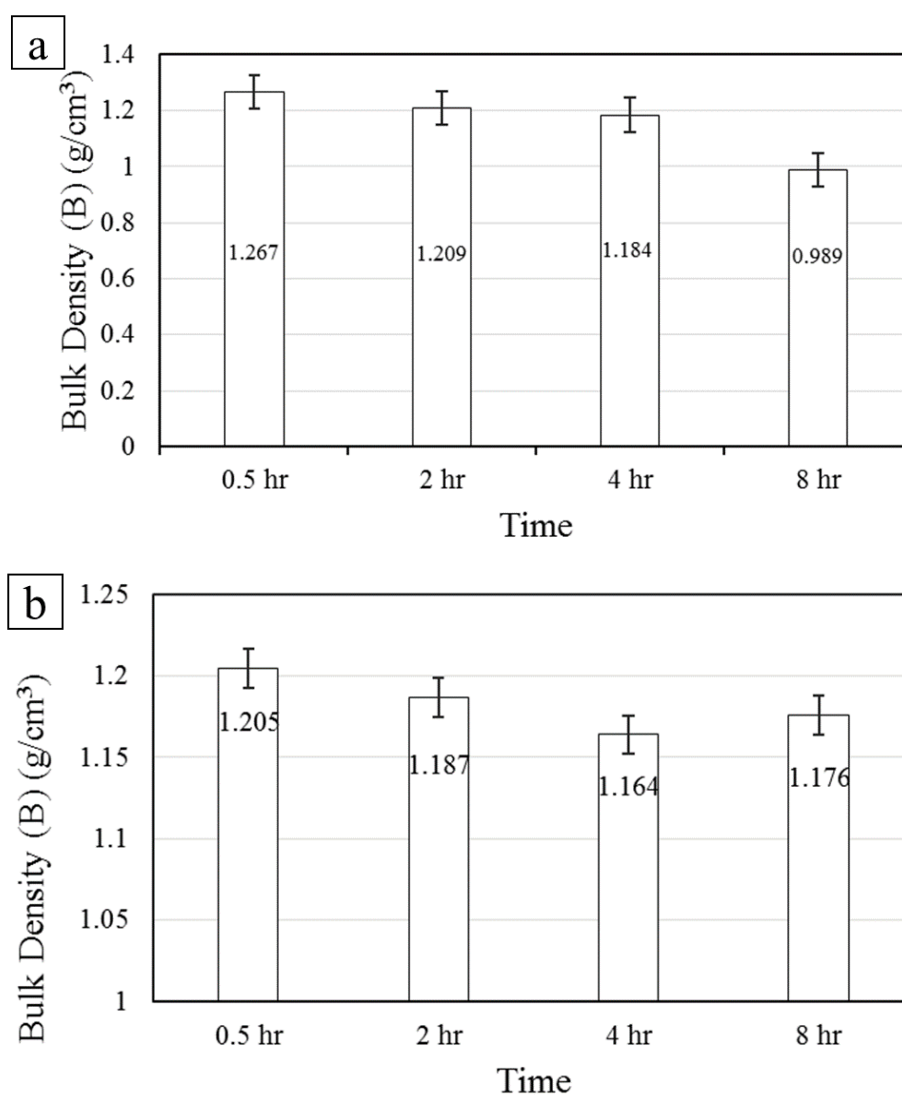


Figure 4.13. The effect of high energy milling time on the bulk density of the WSi₂ intermetallic (a) CaWO₄-Si-Al reactant system, and (b) CaO-WO₃-Si-Al reactant system.

4.1.4.4 Apparent Porosity of the WSi₂ Intermetallic

The calculated apparent porosity percentage results also decreased from 2.547% through 2.397% and 1.216% to 0.843% as milling time increased from 0.5 through 2 and 4 to 8 hr for CaWO₄-Si-Al reactant system. Figure 4.14 shows that the intermetallic product for 8 hr milling can get the fewer pores on the surface of the product for two systems. Comparing the results between two systems, the results for 0.5 hr and 2 hr have almost the same but the results for 4 hr and 8 hr were altered. The highest density and lowest apparent porosity percentage can get at 8 hr milling time for CaWO₄-Si-Al reactant system.

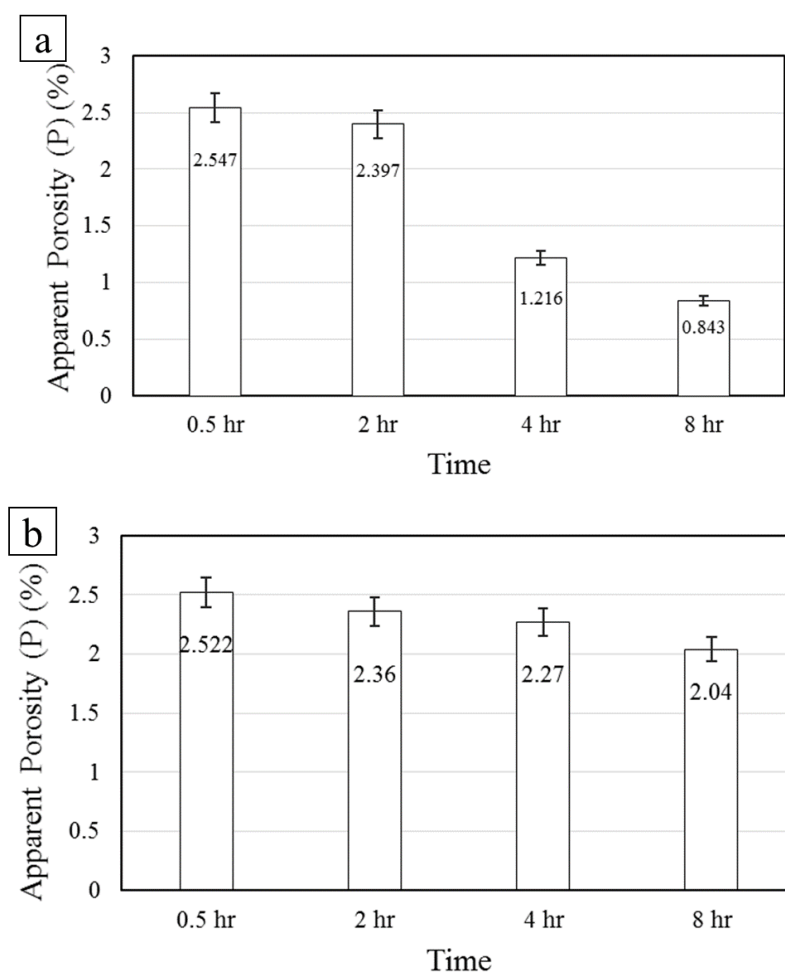


Figure 4.14. The effect of high energy milling time on the apparent porosity percentage of the WSi₂ intermetallic (a) CaWO₄-Si-Al reactant system, and (b) CaO-WO₃-Si-Al reactant system.

4.1.4.5 Micro-Vickers Hardness of the WSi_2 Intermetallic

The average micro-Vickers hardness results for both systems are illustrated in Figure 4.15 (a, b, and c). The products synthesized from CaWO_4 -Si-Al reactant system were softer than the products synthesized using CaO-WO_3 -Si-Al reactant system. It can be seen clearly in Figure 4.15 (a, c), the hardness values are increased when the amount of Si increased. However, the highest hardness for CaWO_4 -Si-Al reactant system is lesser than the one products form CaO-WO_3 -Si-Al reactant system. Indeed, the hardness values were related to their purity percentages and microstructural results. As mentioned above, the most compact microstructure in SEM result had the highest hardness of about 923 HV. Moreover, the dense and compact sample can get more hardness value. The tested properties for both reactant systems are listed in Table 4.5 and 4.6.

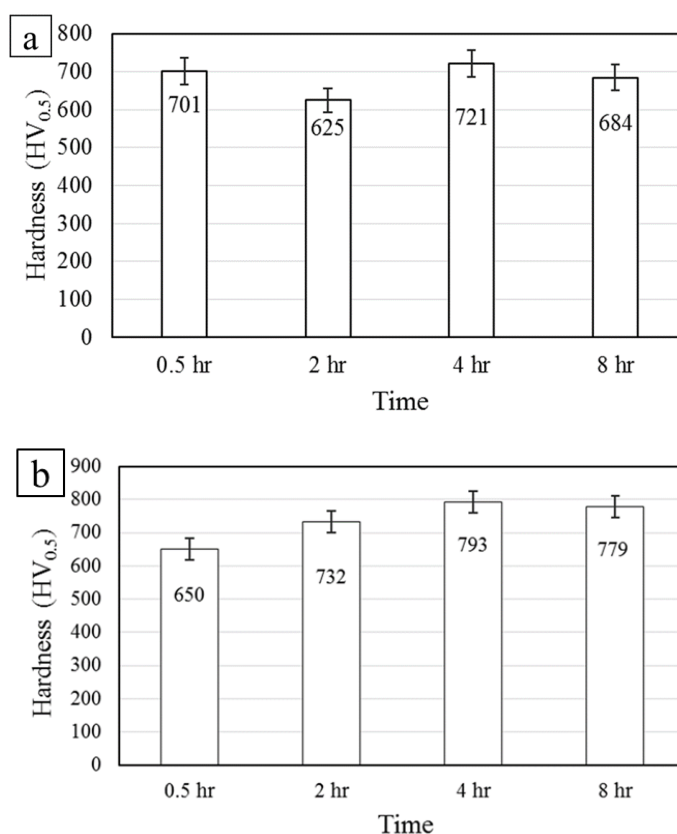


Figure 4.15. The effect of high energy milling time on micro-Vicker hardness values of the WSi_2 intermetallic (a) CaWO_4 -Si-Al reactant system (2+0) mole Si, and (b) (2+0.5) mole Si, and (c) CaO-WO_3 -Si-Al reactant system.

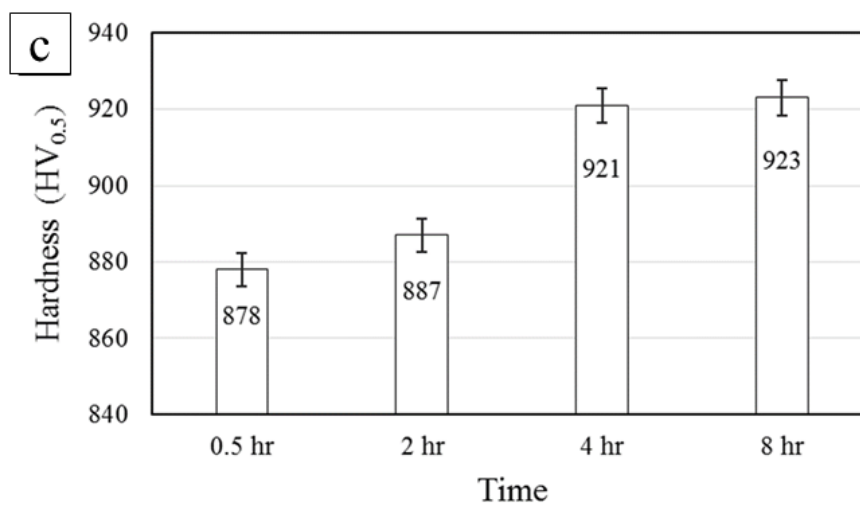


Figure 4.15. (cont.) The effect of high energy milling time on micro-Vicker hardness values of the WSi_2 intermetallic (a) CaWO_4 -Si-Al reactant system (2+0) mole Si, and (b) (2+0.5) mole Si, and (c) CaO-WO_3 -Si-Al reactant system.

Table 4.5. Properties for CaWO_4 -Si-Al reactant systems.

CaWO ₄ -Si-Al reactant system (n=0) Si	High Energy Milling Time (hr)			
	0.5	2	4	8
Combustion Wave (mm/s)	0.65	0.67	0.76	0.87
Density (g/cm ³)	6.09	7.56	8.17	8.75
Bulk Density (g/cm ³)	1.27	1.21	1.18	0.99
Apparent Porosity (%)	2.55	2.39	1.22	0.84
Micro-Vicker Hardness (HV _{0.5})	701	625	721	684

Table 4.6. Properties for CaO-WO₃-Si-Al reactant systems.

CaO-WO ₃ -Si-Al reactant system	High Energy Milling Time (hr)			
	0.5	2	4	8
Combustion Wave (mm/s)	1.13	0.925	0.88	1.055
Density (g/cm ³)	7.26	7.88	8.02	8.21
Bulk Density (g/cm ³)	1.21	1.19	1.16	1.17
Apparent Porosity (%)	2.52	2.36	2.27	2.04
Micro-Vicker Hardness (HV _{0.5})	878	887	921	923

4.1.5 Characterization of the Sand Mold and Oxide Slag

It was found that the use of sand mold promoted phase separation of the oxide and intermetallic product. This is due to the formation of spinel solid solution between the sand mold surface (SiO₂) and the oxide product (CaAl₂O₄). The intermetallic phases are completely separated and the heavier WSi₂ intermetallic settles to the bottom while the lighter oxide slag CaAl₂O₄ rises to the top in the graphite mold, as shown in Figure 4.16. Two types of oxide slag configuration were observed along the sand mold walls and cap that enclosed the intermetallic ingot. The photograph of the sand mold after the reaction was shown in Figure 4.17. It is confirmed that the sand mold tapped a large amount of oxide slag along the mold wall. Moreover, the new phase (white color) between the oxide slag and sand mold wall can be seen clearly in Figure 4.17. The phases were confirmed by XRD and EDX, as shown in Figures 4.18 and 4.19.

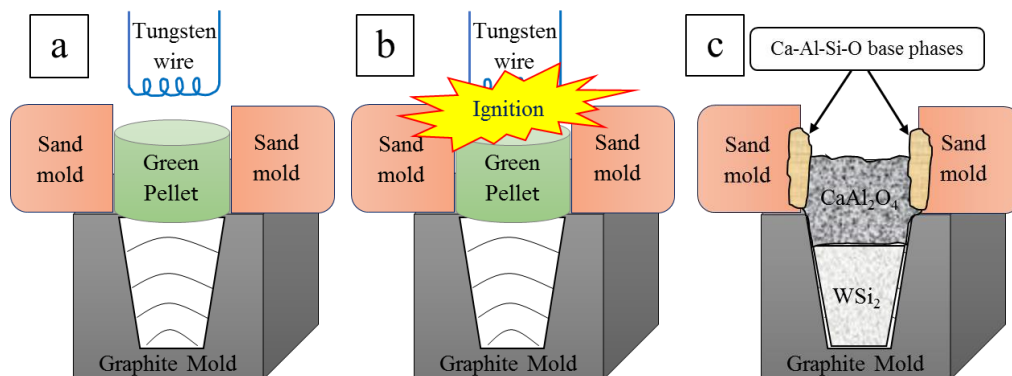


Figure 4.16. The stages in SHS-reaction based processing of a reactant: (a) with prepared reagent pellet, (b) ignition, and (c) showing the phase formed between oxide slag and sand mold.

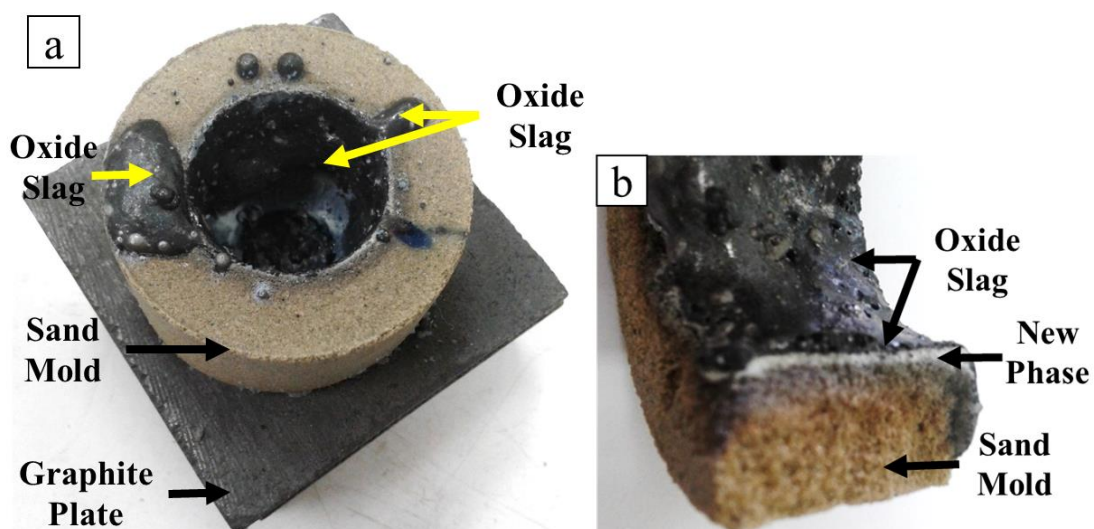


Figure 4.17. The digital photograph of the sand mold after SHS-reaction (a) showing the oxide slag trapped on the sand mold wall, and (b) cross-section view of the sand mold.

The XRD patterns for the SHS combustion products between oxide slag and sand mold are shown in Figure 4.18. As in the cross-section view insert of the sand mold in Figure 4.18, the phase between the sand mold and oxide slag was characterized 2 mm from outer sand mold wall and next 3 mm over 2 mm. The XRD results of Figure 4.18 (b) show major peaks for quartz (SiO_2 , JCPDF No.01-085-0794) and a mixture of potassium aluminum silicate (KAlSi_3O_8 , JCPDF No. 01-084-0708) and sodium calcium

aluminum silicate ($(\text{Na}_{0.84}\text{Ca}_{0.16})\text{Al}_{1.16}\text{Si}_{2.84}\text{O}_8$, JCPDF No. 01-076-0927). The mixture was formed by reactions between sand mold wall and oxide slag during combustion synthesis. Figure 4.18 presents EDX point analysis of the cross-section view of the sand mold wall. As the major phase, SiO_2 was observed at point 1 in Figure 4.19 (a) with some Al, Ca, W, K and C also observed at points 2, 3 and 4. This suggests diffusion of some trace Al, Ca and W into the mold, and some inclusions of C and K from the natural sand. Sodium silicate likely acted as a binding agent, as Na was detected in the sand mold (Figure 4.19 (b,c)). Oxide slag point 5 in Figure 4.19 (e) showed CaAl_2O_4 with some W and Si trapped during synthesis. According to these results, the sand mold reacted to some extent with the oxide slag and formed a new Ca-Al-Si-O based phase.

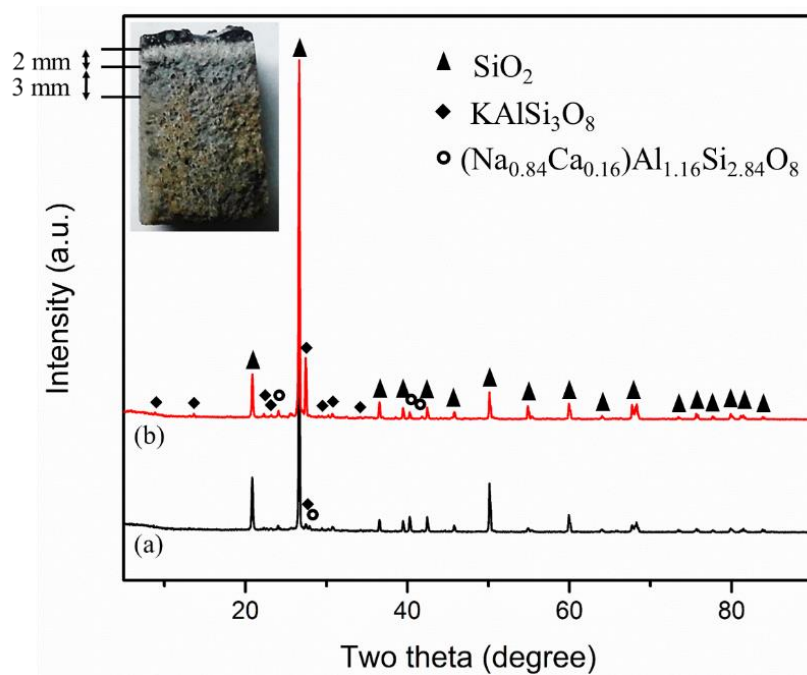


Figure 4.18. XRD results between sand mold wall and oxide slag (a) 3 mm and (b) 2 mm from the mold wall. The insert shows a cross-section of the sand mold.

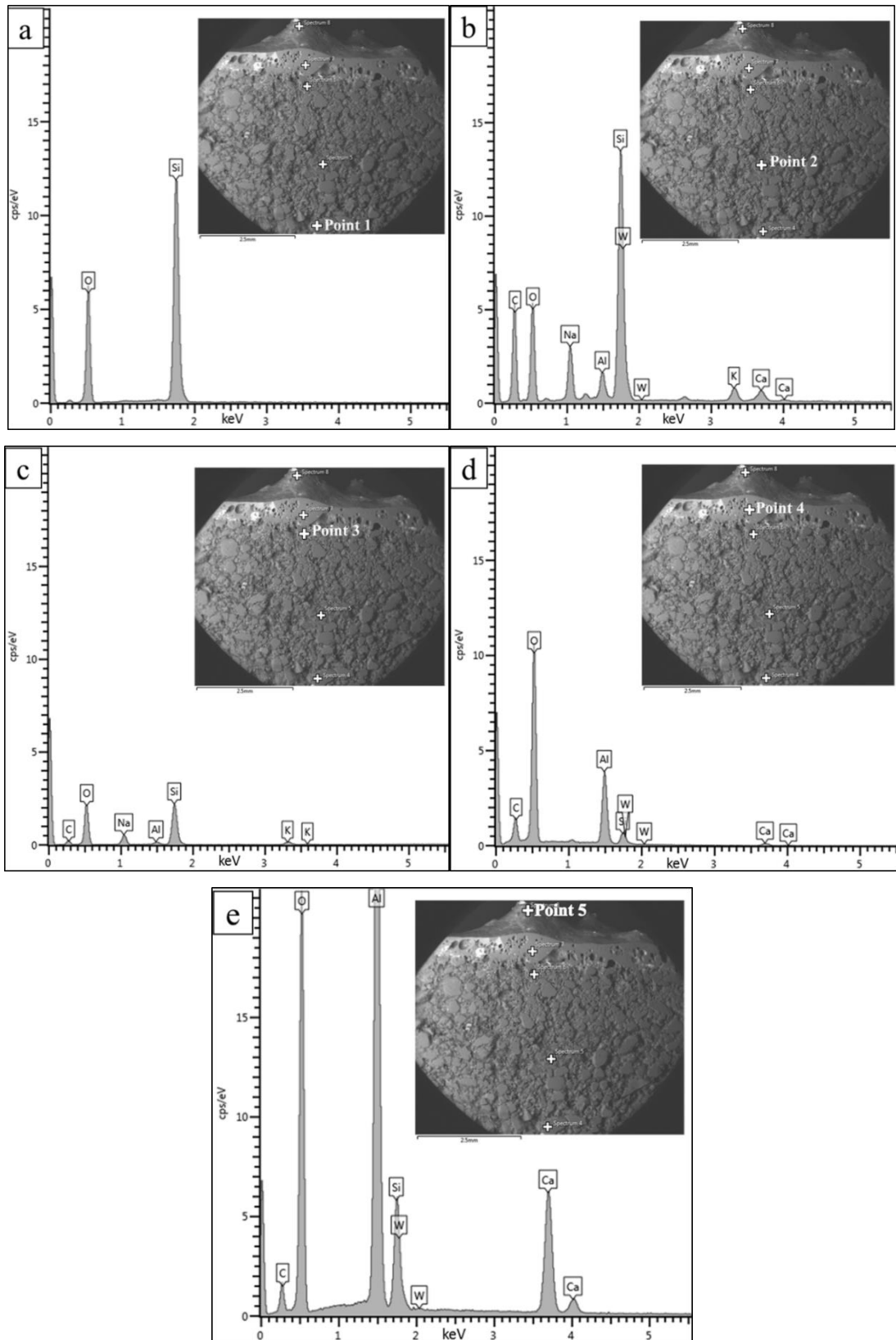


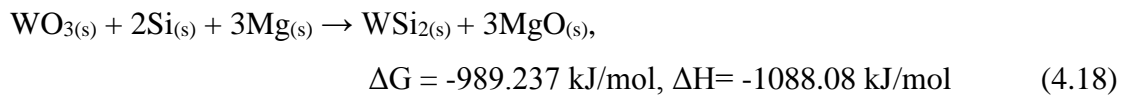
Figure 4.19. EDX analysis of select cross-section points including the sand mold wall: points (a) 1, (b) 2, (c) 3, (d) 4, and (e) 5.

4.2 Synthesis of Tungsten Silicide Intermetallic Alloy by Magnesiothermic Reduction Reaction

The scope of this study is concerned with the thermodynamic modeling of magnesiothermic reduction of W from WO_3 and follow the reaction with Si. This was done to determine the equilibrium temperature and compositions of the reaction products under the adiabatic condition as functions of the composition and initial temperature of raw materials. Moreover, the phase composition, microstructure, and density of SHS products fabricated by this process were also characterized.

4.2.1 Thermal Analysis

The exothermic chemical reaction expresses in Eq. (4.18) and the stoichiometric molar ratio ($\text{WO}_3\text{-2Si-3Mg}$) was chosen as the starting composition. The reactant powders were weighted according to the reaction Eq. (4.18).



The calculated adiabatic temperature (T_{ad}) of the SHS process for Eq. (4.18) is 3913.7°C. The calculated equilibrium concentration of stable species produced by SHS reaction is shown in Figure 4.20. The calculated adiabatic combustion temperature (T_{ad}) of the reaction system is higher than 1800°C and it is higher than the acceptable temperature to start the self-sustain combustion.

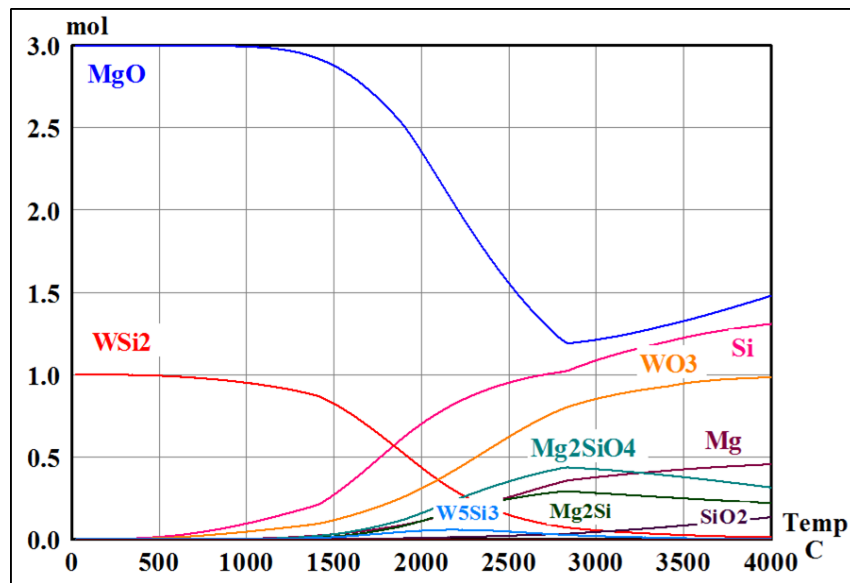


Figure 4.20. Equilibrium composition of WO_3 -Si-Mg reactant system in Argon gas atmosphere.

4.2.2 Intermetallic Product Characterization

The photograph of the SHS-product after synthesis shows in Figure 4.21(a). It can be seen that two phases were solid form and separated easily. The illustration of reaction mechanism and phase separation during SHS reaction is shown in Fig. 4.21(b). During SHS reaction, combustion wave self-propagated through the sample. The exact position where the combustion wave stops is called the extinction front which moves the opposite end of the sample. The heavy intermetallic alloy (WSi_2 - W_5Si_3) was located at the bottom and the lighter oxide slag (Mg_2SiO_4) was floated to the top due to the different density and surface tension.

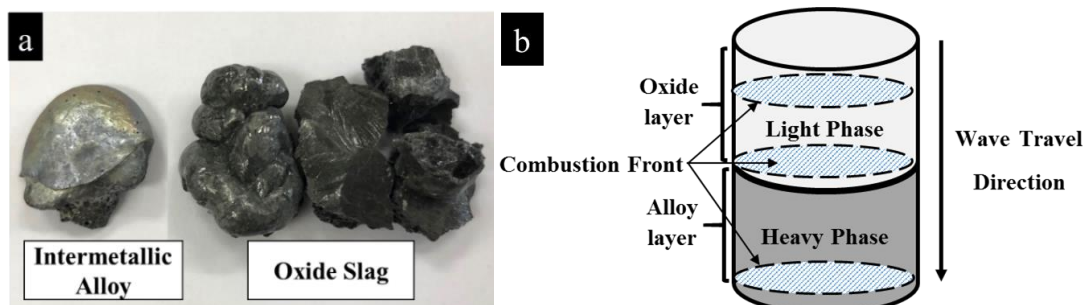


Figure 4.21. As-synthesized SHS-product (a) Digital photograph and (b) illustration of combustion wave travel and phase separation during combustion.

The calculated density (ρ) by Archimedes' Principle of the intermetallic alloy and oxide slag was 8.97 g/cm^3 (96.42% for WSi_2 and 73.5% for W_5Si_3 theoretical density) and 2.45 g/cm^3 (76.3% theoretical density), respectively. The bulk density of the products were observed by ASTM C 373- 88. The calculated bulk density (B) for intermetallic alloy and oxide slag were 1.17 and 1.69 g/cm^3 , respectively. These values represented the average of measurement on 3 samples.

The average micro-Vickers hardness test, randomly tested 10 points on the surface of the polished sample, for this system are illustrated in Figure 4.22. All hardness values are higher than 1200 HV and the highest one is 1566 HV, the average hardness value is about 1420 HV. Moreover, the hardness values for magnesiothermic reactant system is higher than all the products form aluminothermic reactant system. As mentioned above, the hardness values were related to their purity percentages and microstructural results.

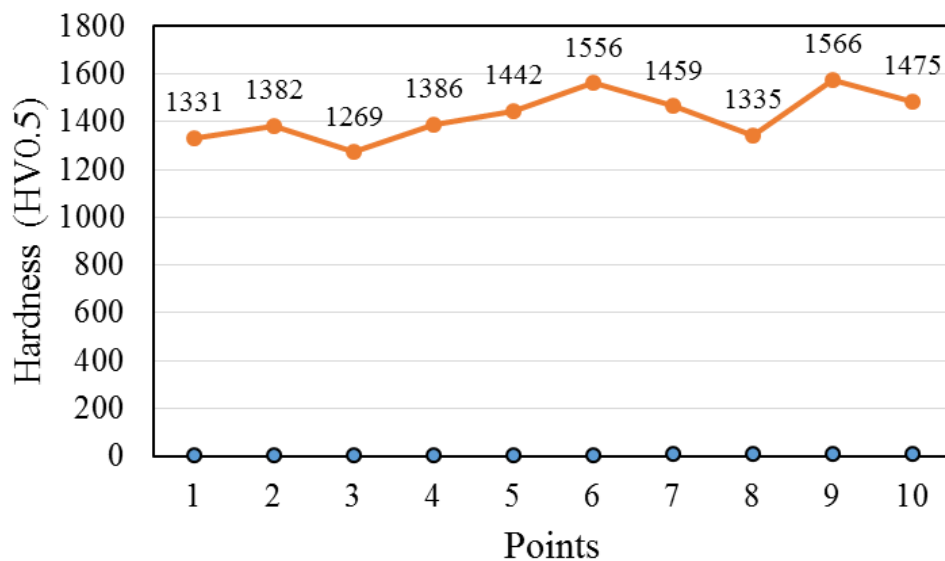


Figure 4.22. Micro hardness values spreading for ten points on the surface of the intermetallic alloy.

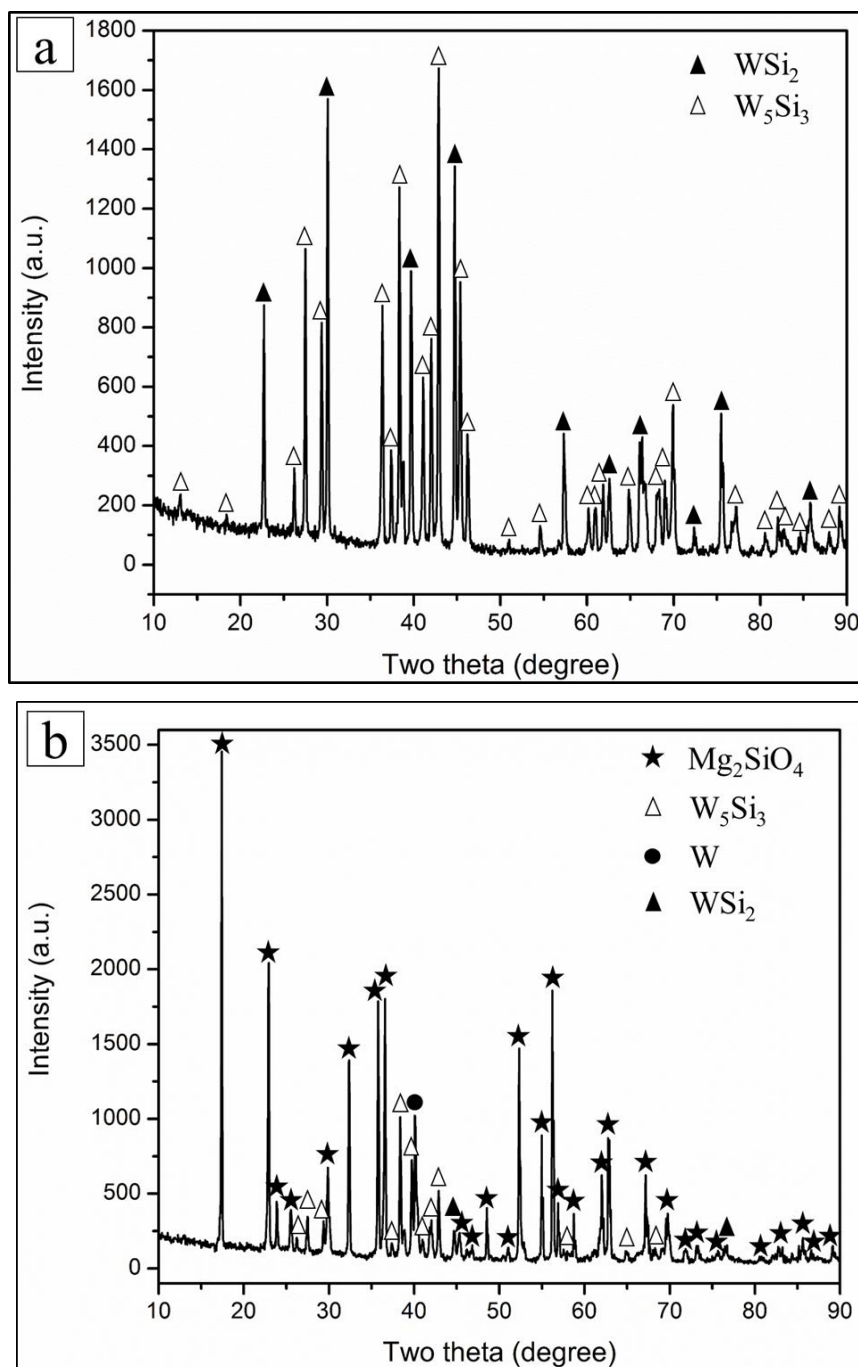


Figure 4.23. XRD results of SHS product of (a) intermetallic alloy and (b) oxide slag.

Figure 4.23 shows an XRD pattern of as-synthesized product. XRD results in Figure 4.23(a) show the two major peaks of WSi_2 and W_5Si_3 . It can be seen that the SHS reaction was completed because free Mg, Si and intermediate phase of Mg_2SiO_4 peaks did not appear for an intermetallic alloy of as-synthesized product. It was noticed that the magnesiothermic reaction process successfully synthesized of WSi_2 - W_5Si_3

intermetallic alloy and also promoted the phase separation between alloy and oxide slag of the product. The major phase in oxide slag is Mg_2SiO_4 while W_5Si_3 , W, and WSi_2 remained as minor phases in Figure 4.23(b).

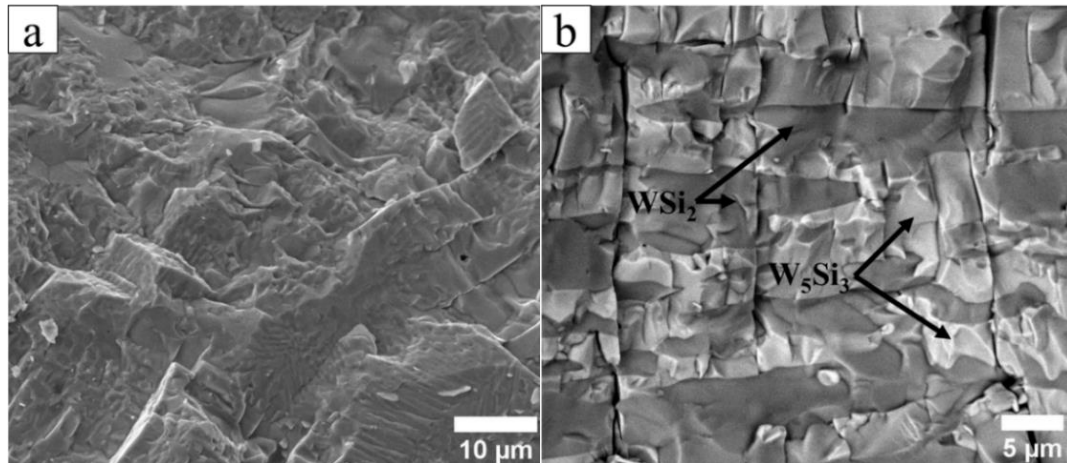


Figure 4.24. SEM microphotograph of the as-SHS crack surface of intermetallic alloy (a) SE and (b) BSE images (WSi_2 dark gray, W_5Si_3 light gray).

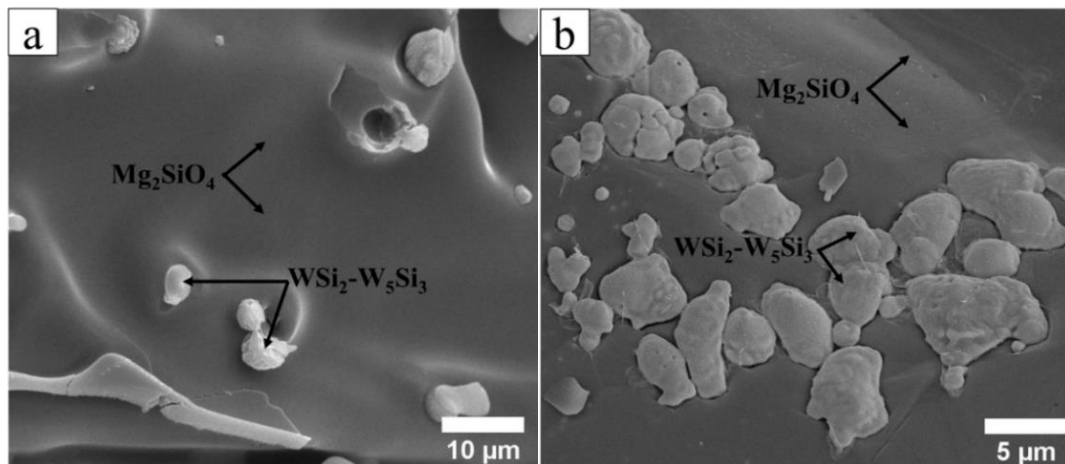


Figure 4.25. SEM secondary electron images of the as-SHS crack surface of oxide slag (a) Mg_2SiO_4 area (dark gray) and (b) WSi_2 - W_5Si_3 area (light gray).

The SEM microstructure of the SHS product crack surface of intermetallic alloy and oxide slag is shown in Figure 4.24 and 4.25. Secondary electron (SE) image in Fig. 4.24 (a) shows a cracking surface of the continuous intermetallic matrix phase. From the XRD pattern of alloy condition, it suggested that the layers were W-Si based alloy.

Two difference phases as shown in the backscattered electron (BSE) image in Figure 4.24(b), dark gray phase WSi_2 and light gray phase W_5Si_3 , were well distinguished on the BSE image [120, 121]. In Figure 4.25, it is clearly seen as two different phases which dark gray background of Mg_2SiO_4 and small light gray particles (WSi_2 - W_5Si_3) which is trapped by rapid cooling rate located along on the Mg_2SiO_4 background.

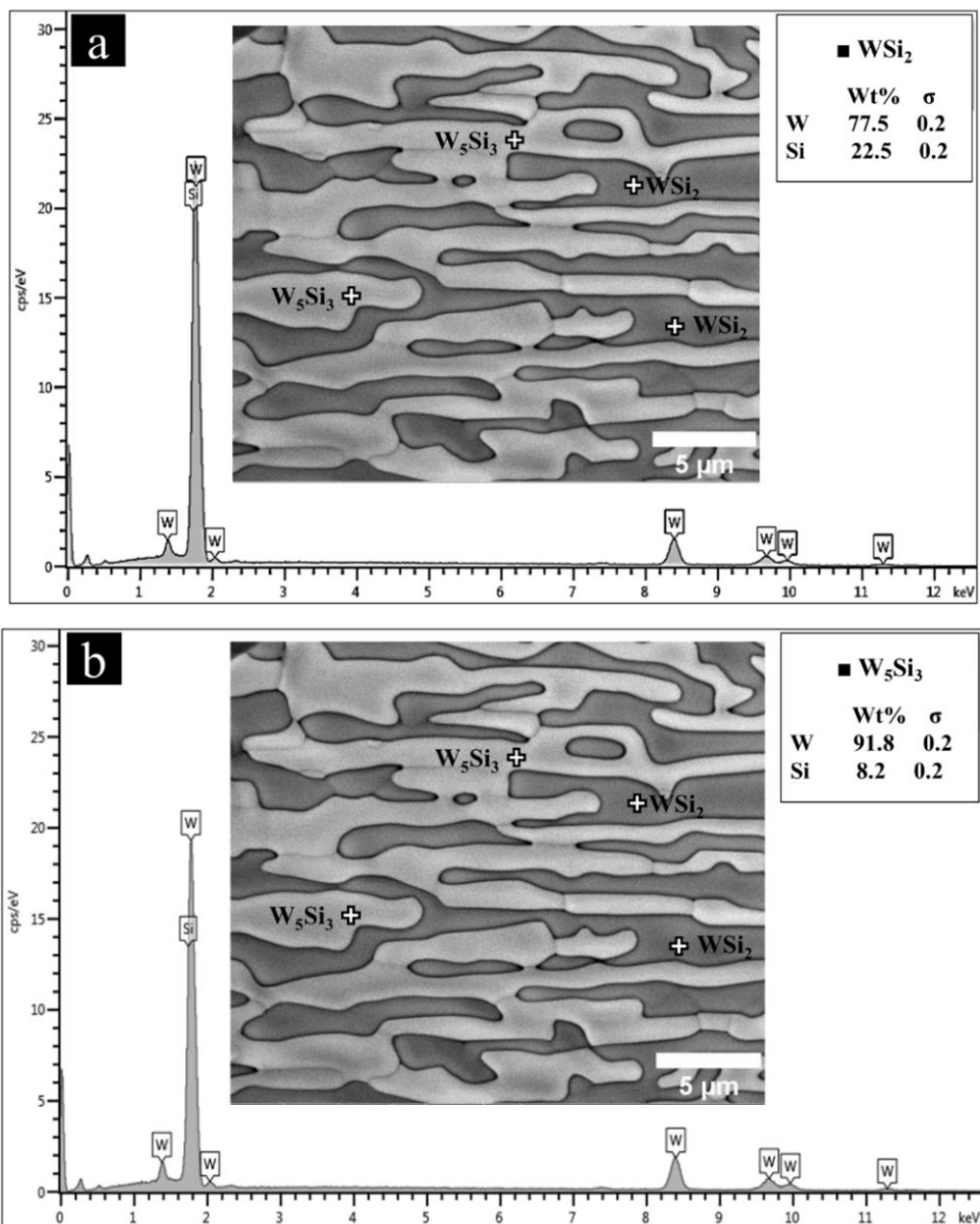


Figure 4.26. EDX point analysis of as-SHS cross-section of intermetallic alloy (a) WSi_2 dark gray phase and (b) W_5Si_3 light gray phase area.

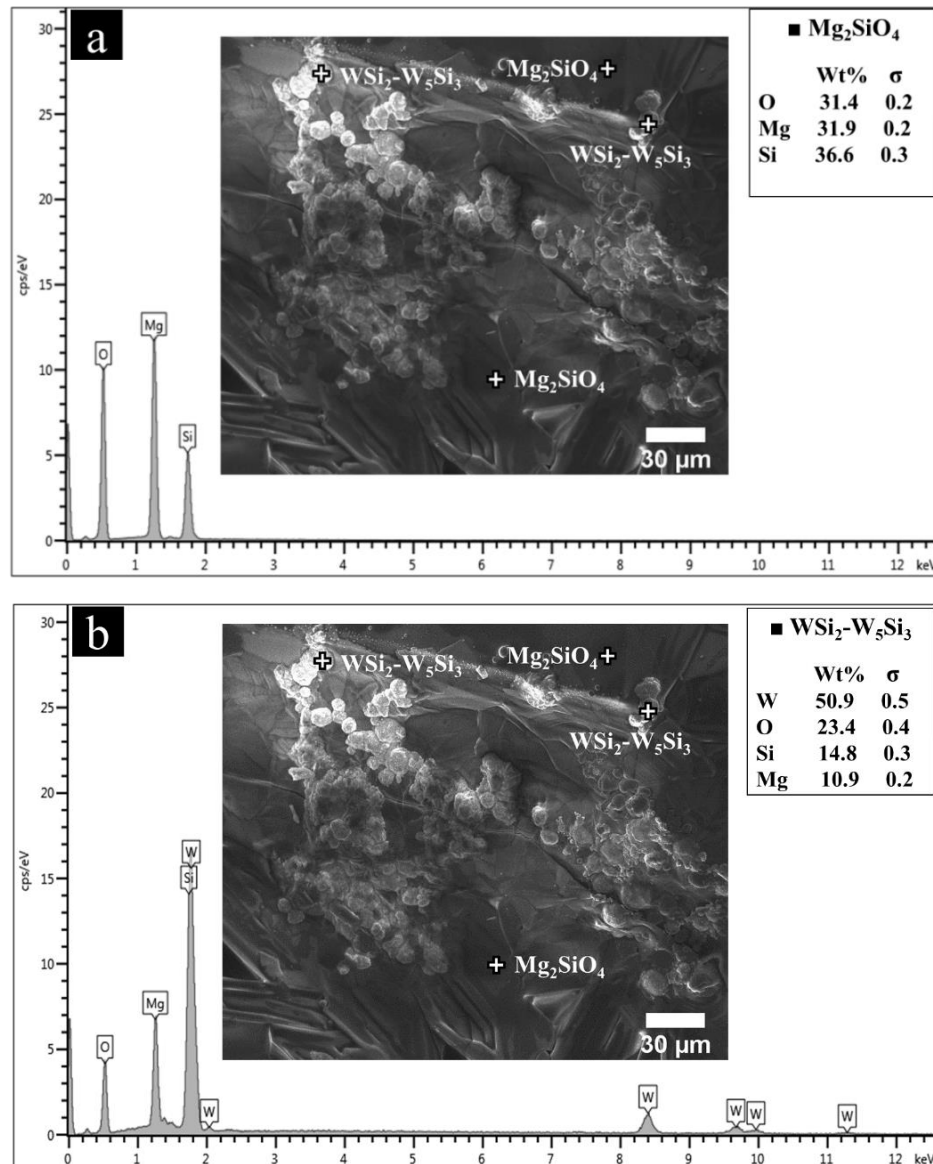


Figure 4.27. EDX point analysis of the as-SHS crack surface of oxide slag (a) Mg_2SiO_4 dark gray background and (b) $WSi_2-W_5Si_3$ light gray particles area.

The phase confirmation for intermetallic alloy and oxide slag were performed by the EDX point analysis on cross-section for intermetallic alloy and crack surface for slag as can be seen in Figure 4.26 and 4.27. To obtain such result there have measured dark and light phases in 4 points on intermetallic alloy and dark background and light particles in 4 points on oxide slag. It can be seen clearly in Figure 4.26, there is no voids or holes around the grain and the two phases were homogeneously distributed

Chapter 5

Conclusions and Suggestion

5.1 Conclusions

In the first part of this research work, tungsten silicide (WSi_2) intermetallic was successfully prepared via SHS with aluminothermic reaction from two reactant systems using scheelite ($\text{CaWO}_4\text{-Si-Al}$) and pure oxide ($\text{CaO-WO}_3\text{-Si-Al}$). The equilibrium compositions of the reactions were calculated by standard Gibbs energy minimization.

According to the experimental results, intermetallic WSi_2 was successfully synthesized with both systems. Using pure oxide ($\text{CaO-WO}_3\text{-Si-Al}$) reactant gave a higher yield of WSi_2 than with scheelite mineral ($\text{CaWO}_4\text{-Si-Al}$), and the yield was optimized by increasing the proportion of Si in the ($\text{CaWO}_4\text{-Si-Al}$) reactant system.

SEM and EDX results showed that high-energy milling of the raw materials did not significantly affect the grain morphology of WSi_2 intermetallic but remarkably decreased the mass fraction of WSi_2 . The use of CaWO_4 (Scheelite) mineral gave nearly similar results as with using the pure oxides (CaO and WO_3) in SHS process to synthesize WSi_2 . Moreover, it was found that the use of a sand mold helped phase separation of the oxide slag and the intermetallic product as well as reducing the liquid eruption.

For the second part, the W-Si based intermetallic alloys ($\text{WSi}_2\text{-W}_5\text{Si}_3$) was also successfully synthesized from ($\text{WO}_3\text{-Si-Mg}$) magnesiothermic reduction reaction via SHS. The SHS product was a high mass fraction and had only tungsten silicide ($\text{WSi}_2\text{-W}_5\text{Si}_3$) two phases in alloy form. Moreover, it can be proposed that the magnesiothermic reaction process also promotes the phase separation between alloy and oxide slag of the product. The intermetallic alloy has 8.97 g/cm^3 approximately 96.42% for WSi_2 and 73.5% for W_5Si_3 of theoretical density. However, it is important to notice that the magnesiothermic reaction can produce a dense and homogeneous contribution of WSi_2 and W_5Si_3 intermetallic alloy in the as-SHS product.

5.2 Suggestion

The high energy milling time suitable for the synthesis of WSi_2 intermetallic from scheelite mineral is (2 hr and 4 hr) with excess Si (0.5 moles), while the appropriate milling time from pure oxide is 4 hr; longer milling times were not necessary. In addition, the suitable molar ratio for the synthesis of WSi_2 intermetallic by SHS for both systems are (1:2.5:2-CaWO₄ : Si: Al) and (1:1:2:2-CaO: WO₃ : Si: Al). However, the higher density, purity and hardness values can get with pure oxide system.

The sand mold can be used in place of more costly types of the mold such as quartz mold. and can be reduced the rate of heat loss from the reaction line during synthesis. This shows the potential of raw materials from nature.

For the production of mixed WSi_2 and W_5Si_3 intermetallic alloy with homogeneous and layer by layer, distribution can be synthesized from (WO₃-Si-Mg) magnesiothermic reduction system. The resulted intermetallic alloy (WSi_2 , W_5Si_3) mechanical properties are higher than those of the properties of WSi_2 intermetallic which synthesized from aluminothermic reduction system.

The higher yield of dense WSi_2 intermetallic and WSi_2 - W_5Si_3 intermetallic alloy obtained by this method might be further improved by better tuning of the self-propagating high-temperature synthesis casting (SHS-casting) process.

References

- [1] U. Ramamurty, A. S. Kim, S. Suresh, and J. J. Petrovic, "Micromechanisms of creep-fatigue crack growth in a silicide-matrix composite with SiC particles," *J. Am. Ceram. Soc.*, vol. 76, no. 8, pp. 1953–1964, 1993.
- [2] I. J. Shon, D. H. Rho, H. C. Kim, and Z. A. Munir, "Dense WSi₂ and WSi₂–20 vol.% ZrO₂ composite synthesized by pressure-assisted field-activated combustion," *J. Alloys Compd.*, vol. 322, pp. 120–126, 2001.
- [3] T. Chanadee, S. Niyomwas, and J. Wannasin, "Novel synthesis of tungsten alloys from metal oxide by self propagating high-temperature synthesis reaction," *Procedia Eng.*, vol. 32, pp. 628–634, 2012.
- [4] A. G. Merzhanov, "Combustion processes that synthesize materials," *J. Mater. Process. Technol.*, vol. 56, no. 1–4, pp. 222–241, 1996.
- [5] D. M. Shah, D. Berczik, D. L. Anton, and R. Hecht, "Appraisal of other silicides as structural materials," *Mater. Sci. Eng. A*, vol. 155, no. 1–2, pp. 45–57, 1992.
- [6] X. Huang, Z. Zhao, L. Zhang, and J. Wu, "The effects of ultra-high-gravity field on phase transformation and microstructure evolution of the TiC-TiB₂ ceramic fabricated by combustion synthesis," *Int. J. Refract. Met. Hard Mater.*, vol. 43, pp. 1–6, 2014.
- [7] L. J. Kecskes, T. Kottke, and A. Niiler, "Microstructural properties of combustion synthesized and dynamically consolidated titanium boride and titanium carbide," *J. Am. Ceram. Soc.*, vol. 73, no. 5, pp. 1274–1282, 1990.
- [8] K. Monogarov, A. Pivkina, N. Muravyev, D. Meerov, and D. Dilhan, "Combustion of micro and nanothermites under elevating pressure," *Phys. Procedia*, vol. 72, pp. 362–365, 2015.
- [9] T. Chanadee, "Experimental studies on self-propagating high-temperature synthesis of Si-SiC composite from reactants of SiO₂ derived from corn cob ash/C/Mg," *J. Aust. Ceram. Soc.*, vol. 53, pp. 245–252, 2017.
- [10] S. Singarothai, M. Khanghamano, and V. Rachphet, "The fabrication of Fe-W-mullite-based composite coatings inside a steel pipe by centrifugal-SHS process," *J. Aust. Ceram. Soc.*, vol. 4, pp. 343–350, 2017.

- [11] P. Mossino, "Some aspects in self-propagating high-temperature synthesis," *Ceram. Int.*, vol. 30, no. 3, pp. 311–332, 2004.
- [12] S. Niyomwas, "Synthesis and characterization of silicon-silicon carbide composites from rice husk ash via self-propagating high temperature synthesis," *J. Met. Mater. Miner.*, vol. 19, no. 2, pp. 21–25, 2009.
- [13] J. J. Moore and H. J. Feng, "Combustion synthesis of advanced materials: Part I. Reaction parameters," *Prog. Mater. Sci.*, vol. 39, no. 94, pp. 243–273, 1995.
- [14] S. Niyomwas, "Preparation of aluminum reinforced with $\text{TiB}_2\text{-Al}_2\text{O}_3\text{-Fe}_x\text{Al}_y$ composites derived from natural ilmenite," *Int. J. Self-Propag. High-Temp Synth.*, vol. 19, no. 2, pp. 150–156, 2010.
- [15] A. A. Hambardzumyan, S. L. Kharatyan, H. L. Khachatryan, and J. A. Puszynski, "Synthesis of $\text{WSi}_2\text{-SiC}$ composite under the thermally activated combustion mode," *Int. J. Refract. Met. Hard Mater.*, vol. 28, no. 5, pp. 605–609, 2010.
- [16] J. Yang, P. La, W. Liu, and Y. Hao, "Microstructure and properties of $\text{Fe}_3\text{Al-Fe}_3\text{AlC}_{0.5}$ composites prepared by self-propagating high temperature synthesis casting," *Mater. Sci. Eng. A*, vol. 382, no. 1–2, pp. 8–14, 2004.
- [17] C. L. Yeh and W. S. Hsu, "Preparation of MoB and MoB-MoSi_2 composites by combustion synthesis in SHS mode," *J. Alloys Compd.*, vol. 440, no. 1–2, pp. 193–198, 2007.
- [18] T. Tsuchida and T. Kakuta, "MA-SHS of NbC and NbB_2 in air from the Nb/B/C powder mixtures," *J. Eur. Ceram. Soc.*, vol. 27, no. 2–3, pp. 527–530, 2007.
- [19] T. Chanadee, J. Wannasin, and S. Niyomwas, "Synthesis of WSi_2 and W_2B intermetallic compound by in-situ self propagating high-temperature synthesis reaction," *J. Ceram. Soc. Japan*, vol. 1226, pp. 0–5, 2014.
- [20] L. de Barros, A. P. M. Pinheiro, J. da E. Câmara, and K. Iha, "Qualification of magnesium/Teflon/Viton pyrotechnic composition used in rocket motors ignition system," *J. Aerosp. Technol. Manag.*, vol. 8, no. 2, pp. 130–136, 2016.
- [21] T. Chanadee, S. Niyomwas, and J. Wannasin, "Effect of Ar gas pressure on phase separation of tungsten silicides intermetallic compound in-situ self propagating high temperature synthesis-casting process," *Adv. Mater. Res.*, vol. 626, pp. 143–146, 2013.

- [22] P. Pujalte, R. Arpón, and F. Coloma, “Synthesis of a (WSi_2 , W_5Si_3)-SiC composite using the reaction between WC and Si,” 1999.
- [23] S. Yadav and K. T. Ramesh, “The mechanical properties of tungsten-based composites at very high strain rates,” *Mater. Sci. Engng A*, vol. 203, no. 95, pp. 140–153, 1995.
- [24] A. Bose, R. Sadangi, and R. M. German, “A review on alloying in tungsten heavy alloys,” *Supplemental Proceedings*, pp. 453–465, 2012.
- [25] Plansee, “Tungsten heavy metal.” [Online]. Available: <https://www.plansee.com/en/materials/tungstenheavymetal.html>. [Accessed: 07-Jun-2018].
- [26] International tungsten industry association (ITIA), “Tungsten applications.” [Online]. Available: <https://www.azom.com/article.aspx>. [Accessed: 07-Jun-2018].
- [27] E. Lassner and W.-D. Schubert, “Tungsten Properties”, *Chemistry, Technology of the Element, Alloys, and Chemical Compounds*, 1999.
- [28] D. L. Perry and S. L. Phillips, “Handbook of Inorganic Compounds,” pp. 127–128, 1995.
- [29] S. Roy and A. Paul, “Diffusion in tungsten silicides,” *Intermetallics*, vol. 37, pp. 83–87, 2013.
- [30] P. Villars and K. Cenzual, Eds., “ W_3Si_2 (W_5Si_3) Crystal Structure: Datasheet from ‘Pauling File Multinaries Edition–2012’ in Springer Materials (https://materials.springer.com/isp/crystallographic/docs/sd_0532963).” [Online]. Available: https://materials.springer.com/isp/crystallographic/docs/sd_0532963.
- [31] V. Y. Petrishchev and V. I. Nizhenko, “Investigation of liquid-phase sintering in W–Sn–Si pseudoalloys,” *Powder Metall. Met. Ceram.*, vol. 40, no. 7, pp. 398–404, 2001.
- [32] T. America, “FX₁₀₅Si₃N₄ ceramic grade,” in *IOP Conf. Series: Materials Science and Engineering*, pp. 347, 2018.
- [33] Y. Muraoka, M. Yoshinaka, K. Hirota, and O. Yamaguchi, “Hot isostatic pressing of composite powder in the system ZrO₂-WSi₂; Part1: microstructure and mechanical properties,” vol. 2, pp. 30–35, 1995.

- [34] F. Chen, J. Xu, Y. Liu, and L. Cai, "In situ reactive spark plasma sintering of $WSi_2/MoSi_2$ composites," *Ceram. Int.*, vol. 42, no. 9, pp. 11165–11169, 2016.
- [35] N. Petermann *et al.*, "Microwave plasma synthesis of Si/Ge and Si/ WSi_2 nanoparticles for thermoelectric applications," *J. Phys. D. Appl. Phys.*, vol. 48, no. 31, pp. 1-10, 2015.
- [36] R. Madar and C. Bernard, "Chemical vapor deposition of refractory metals disilicides : a review," *J. Phys. Colloq.*, vol. 50 (C5), pp. C5-479-C5-497, 1989.
- [37] B. S. Ong, K. L. Pey, C. Y. Ong, C. S. Tan, D. A. Antoniadis, and E. A. Fitzgerald, "Comparison between chemical vapor deposited and physical vapor deposited WSi_2 metal gate for InGaAs n-metal-oxide-semiconductor field-effect transistors," *Appl. Phys. Lett.*, vol. 98, no. 18, pp. 12-18, 2011.
- [38] T. Kato, *Geology of Ore Deposits*. Interperiodica Pub., 1937.
- [39] B. J. Skinner, "The System of Mineralogy of James Dwight Dana and Edward Salisbury Dana.," *Science (80)*, vol. 139, no. 3557, pp. 821–1155, 1963.
- [40] H. K. Worner and R. W. Mitchell, *Minerals of Broken Hill*. Australian Mining & Smelting Ltd, 1983.
- [41] A. P. Sabina, "Rocks and minerals for the collector: Bay of Fundy, New Brunswick and Nova Scotia; South Shore, Nova Scotia," 2015.
- [42] D. J. Kontak, P. K. Smith, and P. H. Reynolds, "Geology and $^{40}Ar/^{39}Ar$ geochronology of the Beaver Dam gold deposit, Meguma Terrane, Nova Scotia, Canada; evidence for mineralization at 370 Ma," *Econ. Geol.*, vol. 88, no. 1, pp. 139–170, 1993.
- [43] J. Dostal, D. J. Kontak, and A. K. Chatterjee, "Trace element geochemistry of scheelite and rutile from metaturbidite-hosted quartz vein gold deposits, Meguma Terrane, Nova Scotia, Canada: Genetic implications," *Mineral. Petrol.*, vol. 97, no. 1–2, pp. 95–109, 2009.
- [44] F. Pirajno and P. N. Bentley, "Greisen-related scheelite, gold and sulphide mineralisation at kirwans hili and bateman creek, reefton district, westland, new zealand," *New Zeal. J. Geol. Geophys.*, vol. 28, no. 1, pp. 97–109, 1985.
- [45] R. G. Dickinson, "The crystal structures of wulfenite and scheelite.," *J. Am. Chem. Soc.*, vol. 42, no. 1, pp. 85–93, 1920.
- [46] J. R. Smyth, S. D. Jacobsen, and R. M. Hazen, "Comparative crystal chemistry

- of dense oxide minerals,” *Rev. Mineral. Geochemistry*, vol. 41, no. 1, pp. 157–186, 2000.
- [47] S. N. Achary, S. J. Patwe, P. S. R. Krishna, A. B. Sindhe, and A. K. Tyagi, “Crystal structure analysis of Scheelite and Zircon type thorium germanates: A neutron diffraction study,” *J. Alloys Compd.*, vol. 438, no. 1–2, pp. 274–278, 2007.
- [48] “Cooking with lime heat, fireless cooking in medieval, renaissance and victorian times.” [Online]. Available: <http://www.oldandinteresting.com/fireless-cooking-with-quicklime.aspx>. [Accessed: 10-Jun-2018].
- [49] S. S. Zumdahl, *Chemical principles*. Houghton Mifflin, 2009.
- [50] “Calcium Oxide, Thousand Lights, Chennai, ID: 16051594130.” [Online]. Available: <https://www.indiamart.com/proddetail/calcium-oxide-16051594130.html>. [Accessed: 10-Jun-2018].
- [51] “CaO-Calcium oxide Polymer.” [Online]. Available: <http://www.chemtube3d.com/gallery/structurepages/cao-poly.html>. [Accessed: 10-Jun-2018].
- [52] Shakhasiri, “Lime: Calcium Oxide,” *Chem.* vol. 103, pp. 1–2, 2000.
- [53] Usgs, *Minerals Yearbook*, 2007.
- [54] A. Varma, A. S. Rogachev, A. S. Mukasyan, and S. Hwang, *Combustion Synthesis of Advanced Materials: Principles and Applications*, vol. 24, 1998.
- [55] R. Mart, “Chapter 3: Synthesis,” pp. 69–97, 2010.
- [56] E. A. Levashov, A. S. Mukasyan, A. S. Rogachev, and D. V Shtansky, “Self-propagating high-temperature synthesis of advanced materials and coatings,” *Int. Mater. Rev.*, vol. 62, no. 4, pp. 203–239, 2017.
- [57] M. M. Pacheco, “Self-sustained high-temperature reactions: initiation, propagation and synthesis,” 2007.
- [58] S. Niyomwas, “Synthesis and characterization of TiC and TiC-Al₂O₃ composite from wood dust by self-propagating high-temperature synthesis,” *Energy Procedia*, vol. 9, pp. 522–531, 2011.
- [59] J. J. Moore and H. J. Feng, “Combustion synthesis of advanced materials: Part II. Classification, applications and modeling,” *Prog. Mater. Sci.*, vol. 39, no. 4–5, pp. 275–316, 1995.

- [60] I. Tomaszkiwicz, G. A. Hope, and C. M. B. Li, "Thermodynamic properties of silicides fluorine combustion calorimetric determination of the standard molar enthalpy of formation at the temperature 298.15 K," *J. Chem. Thermodyn.*, vol. 30, no. 27, pp. 585–596, 1997.
- [61] J. B. Holt and Z. A. Munir, "Combustion synthesis of titanium carbide: Theory and experiment," *J. Mater. Sci.*, vol. 21, no. 1, pp. 251–259, 1986.
- [62] R. Pampuch and L. Stobierski, "Solid combustion synthesis of refractory carbides: (A review)," *Ceram. Int.*, vol. 17, no. 2, pp. 69–77, 1991.
- [63] S. D. Dunmead, Z. A. Munir, J. B. Holt, and D. D. Kingman, "Simultaneous synthesis and densification of TiC/Ni-Al composites," *J. Mater. Sci.*, vol. 26, no. 9, pp. 2410–2416, 1991.
- [64] J. J. Moore, D. W. Readey, H. J. Feng, K. Monroe, and B. Mishra, "The combustion synthesis of advanced materials," *JOM*, vol. 46, no. 11, pp. 72–78, 1994.
- [65] Z. Fan, C. Ji, Z. Xi, and Z. Guan, "Standard Gibbs free energy of formation of the high- T_c superconducting compound $YBa_2Cu_3O_{6.5+\delta}$," *Supercond. Sci. Technol.*, vol. 2, no. 1, pp. 43–46, 1989.
- [66] J. Wang, "Experimental and Thermodynamic Study on the Mg-X (X : Ag, Ca, In, Li, Na, Sn, Sr and Zn) Multicomponent Systems," 2014.
- [67] D. H. Kang *et al.*, "Interfacial free energy controlling glass-forming ability of Cu-Zr alloys," *Sci. Rep.*, vol. 4, pp. 1–5, 2014.
- [68] L. L. Wang, Z. A. Munir, and Y. M. Maximov, "Thermite reactions: their utilization in the synthesis and processing of materials," *J. Mater. Sci.*, vol. 28, no. 14, pp. 3693–3708, 1993.
- [69] F. Zhanguo, J. Chunlin, X. Zhengping, and G. Zhongyi, "Standard Gibbs free energy of formation of the high- T_c superconducting compound $YBa_2Cu_3O_{6.5+}$," *Supercond. Sci. Technol.*, vol. 2, no. 1, pp. 43–46, Jun. 1989.
- [70] A. G. Merzhanov, "Fundamentals, achievements, and perspectives for development of solid-flame combustion," *Russ. Chem. Bull.*, vol. 46, no. 1, pp. 1–27, 1997.
- [71] K. Morsi, "The diversity of combustion synthesis processing: A review," *J. Mater. Sci.*, vol. 47, no. 1, pp. 68–92, 2012.

- [72] J. F. Crider, "Self-propagating high temperature synthesis- a soviet method for producing ceramic materials," *Sci. Technol.*, pp. 1–11, 2005.
- [73] G. Tavadze and A. Shteinberg, "Production of advanced materials by methods of self-propagating high-temperature synthesis," in *Springer Briefs in Materials*, no. 30, 2013.
- [74] I. Borovinskaya, T. Ignatieva, and V. Vershinnikov, "Self-propagating high-temperature synthesis of ultrafine tungsten carbide powders," *Tungsten Carbide-Process. Appl.*, pp. 1–20, 2012.
- [75] A. Biswas, S. Roy, K. Gurumurthy, N. Prabhu, and S. Banejee, "A study of self-propagation high-temperature synthesis of NiAl in thermal explosion mode," *Acta Mater.*, vol. 50, pp. 757, 2002.
- [76] A. S. Mukasyan and A. S. Rogachev, "Discrete reaction waves: Gasless combustion of solid powder mixtures," *Prog. Energy Combust. Sci.*, vol. 34, no. 3, pp. 377–416, 2008.
- [77] S. Hwang, A. S. Mukasyan, A. S. Rogachev, and A. Varma, "Combustion wave microstructure in gas-solid reaction systems:experiments and theory," *Combust. Sci. Technol.*, vol. 123, no. 1–6, pp. 165–184, 1997.
- [78] K. Brezinsky, "Gas-phase combustion synthesis of materials," *Symp. Combust.*, vol. 26, no. 2, pp. 1805–1816, 1996.
- [79] A. F. Temperature, "Combustion in gas-phase processes," pp. 17–21, 2007.
- [80] A. G. Merzhanov, "History and recent developments in SHS," *Ceram. Int.*, vol. 21, no. 5, pp. 371–379, 1995.
- [81] I. P. Borovinskaya, "Chemical classes of the SHS processes and materials," *Pure Appl. Chem.*, vol. 64, no. 7, pp. 919–940, 1992.
- [82] J. Sarkar, "Sputtering target manufacturing," in *Sputtering Materials for VLSI and Thin Film Devices*, pp. 197–289, 2014.
- [83] A. Varma and J.-P. Lebrat, "Combustion synthesis of advanced materials," *Chem. Eng. Sci.*, vol. 47, no. 9–11, pp. 2179–2194, 1992.
- [84] A. Varma, A. S. Rogachev, A. S. Mukasyan, and S. Hwang, "Combustion synthesis of advanced materials: principles and applications," *Adv. Chem. Eng.*, vol. 24, pp. 79–226, 1998.
- [85] S. L. González-Cortés and F. E. Imbert, "Fundamentals, properties and

- applications of solid catalysts prepared by solution combustion synthesis (SCS),” *Appl. Catal. A Gen.*, vol. 452, pp. 117–131, 2013.
- [86] A. Varma, B. Li, and A. Mukasyan, “Novel synthesis of orthopaedic implant materials,” *Adv. Eng. Mater.*, vol. 4, no. 7, pp. 482–487, 2002.
- [87] T. I. and V. V. I. Borovinskaya, “Self-propagating high-temperature synthesis of ultrafine tungsten carbide powders,” in *Intech open science*, 2012.
- [88] S. H. Hong, H. J. Ryu, W. H. Sohn, and C. K. Kim, “Homogeneous forming technology of composite materials and its application to dispersion nuclear fuel,” pp. 149–160, 1997.
- [89] A. Varma, A. S. Mukasyan, A. S. Rogachev, and K. V. Manukyan, “Solution combustion synthesis of nanoscale materials,” *Chem. Rev.*, vol. 116, no. 23, pp. 14493–14586, 2016.
- [90] M. Lackner, *Combustion synthesis : novel routes to novel materials*. Bentham Science Publishers, 2010.
- [91] A. Feng and Z. A. Munir, “Relationship between Field Direction and Wave Propagation in Activated Combustion Synthesis,” *J. Am. Ceram. Soc.*, vol. 79, no. 8, pp. 2049–2058, 1996.
- [92] B.-Y. L. Arvind Varma, Alexander Mukasyan, “Synthesis of orthopaedic implant,” *United States Patent, US 6,896,846 B1*, 2005.
- [93] G. Tosun, N. Orhan, and L. Özler, “Investigation of combustion channel in fabrication of porous NiTi alloy implants by SHS,” *Mater. Lett.*, vol. 66, no. 1, pp. 138–140, 2012.
- [94] P. S. To, “Chapter 7 : Basics of X-ray Diffraction,” in *Solutions*, pp. 1–25, 1999.
- [95] A. Authier, *Early days of X-ray crystallography*. Oxford University Press, 2013.
- [96] N. Waeselmann, “Structural transformations in complex perovskite-type relaxor and relaxor-based ferroelectrics at high pressures and temperatures,” 2012.
- [97] “The Electromagnetic Spectrum: X-rays.” [Online]. Available: <http://www.darvill.clara.net/emag/emagxray.htm>. [Accessed: 24-Jun-2018].
- [98] H. Stanjek and W. Häusler, “Introduction To Powder/ Polycrystalline Diffraction,” *Hyperfine Interact.*, vol. 154, pp. 107–119, 2004.
- [99] DannaLab, “What is X-ray diffraction,” 2012. [Online]. Available: <http://www.xrpd.eu/>. [Accessed: 24-Jun-2018].

- [100] B. Hafner, “Energy dispersive spectroscopy on the SEM: A primer,” *Characterization Facility, University of Minnesota*, 2006. [Online]. Available: <http://scholar.google.com/scholar/hl/en&btnG/Search/q/intitle:Energy/Dispersive/Spectroscopy/on/the/SEM>.
- [101] “Grain boundary resistance and nonlinear coefficient correlation figure se bse sem images of triangular precipitates at snmnb0 sample ~ wiring diagram components.” [Online]. Available: <http://farhek.com/jd/118519y/grain-boundary/795sg8/>. [Accessed: 26-Jun-2018].
- [102] M. & Associates, “Energy dispersive spectrometers,” 2005.
- [103] Y. Leng, *Materials Characterization*. 2013.
- [104] M. M. Mohamed, “X-Ray Technology.” [Online]. Available: <http://slideplayer.com/slide/6188331/>. [Accessed: 25-Jun-2018].
- [105] J. Ye, “Preparation and characterisation of novel carbon materials for refractory castable applications,” pp. 69–72, 2014.
- [106] H. Myalska, B. Dybowski, and G. Moskal, “WC-Co coatings and sinters modified with nano-sized tic microstructure – quantitative evaluation,” *Adv. Sci. Technol. Res. J.*, vol. 11, no. 1, pp. 220–231, 2017.
- [107] Fischer Technology Inc., “Methods: X-ray fluorescence analysis, energy dispersive (ED-XRF).” [Online]. Available: <http://www.fischer-technology.com/en/united-states/knowledge/methods/material-testing/x-ray-fluorescence2/>. [Accessed: 25-Jun-2018].
- [108] “XRF Basic Principles.” [Online]. Available: <https://www.slideshare.net/mebecker1/xrf-basic-principles-13490841>. [Accessed: 29-Jun-2018].
- [109] J. M. Guthrie, “Overview of X-ray fluorescence,” in *Archaeometry Laboratory, University of Missouri Research Reactor*, 2012.
- [110] “Instrumental techniques and experimental methods,” pp. 81–103, 2000.
- [111] P. Brouwer, *Theory of XRF*. 2010.
- [112] *Standard Test Method for Water Absorption , Bulk Density , Apparent Porosity , and Apparent Specific Gravity of Fired Whiteware Products 1*, vol. 88, no. Reapproved 2006. 2011.
- [113] D. C. Zipperian, “Metallographic specimen preparation basics,” in *Pace Technologies*, pp. 1–13, 2009.

- [114] D. C. Zipperian, *METALLOGRAPHIC HANDBOOK*. 2011.
- [115] *Outokumpu HSC Chemistry for windows: HSC 4.1*, Outokumpu Research Oy, Finland. 1999.
- [116] A. Cambeses, J. H. Scarrow, and C. De Purchil, "Pathways for quantitative analysis by x-ray diffraction," *An Introd. to Study Mineral.*, pp. 73–92, 2012.
- [117] G. Balcerowska-czerniak, A. Wronkowski, A. J. Anto, Ł. Skowro, and A. A. Wronkowska, "Chemometrics and intelligent laboratory systems the potential of multivariate analysis to phase identification based on x-ray diffraction patterns," *Chemom. Intell. Lab. Syst.*, vol. 135, pp. 126–132, 2014.
- [118] X. Huang, L. Zhang, Z. Zhao, and C. Yin, "Microstructure transformation and mechanical properties of TiC-TiB₂ ceramics prepared by combustion synthesis in high gravity field," *Mater. Sci. Eng. A*, vol. 553, pp. 105–111, 2012.
- [119] I. G. Cano, I. P. Borovinskaya, M. A. Rodriguez, and V. V Grachev, "Effect of dilution and porosity on self-propagating high-temperature synthesis of silicon nitride," *J. Am. Ceram. Soc.*, vol. 85, no. 9, pp. 2209–2211, 2002.
- [120] H. S. Kim, J. K. Yoon, G. H. Kim, J. M. Doh, S. I. Kwun, and K. T. Hong, "Growth behavior and microstructure of oxide scales grown on WSi₂ coating," *Intermetallics*, vol. 16, pp. 360–372, 2008.
- [121] B. A. Gnesin, I. B. Gnesin, and A. N. Nekrasov, "The interaction of carbon with Mo₅Si₃ and W₅Si₃ silicides. Nowotny phase synthesis," *Intermetallics*, vol. 41, pp. 82–95, 2013.

VITAE

Name Mr. Si Thu Myint Maung

Student ID 5910120069

Educational Attainment

Degree	Name of Institution	Year of Graduation
Bachelor of Engineering (Metallurgy)	Kyaukse Technological Universtiy, Myanmar	2012
Master of Engineering (Metallurgical and Materials Science)	Yangon Technological Universtiy, Myanmar	2017

Scholarship Awards during Enrolment

1. Scholar of the 2016 scholarship awards for Master and Ph.D. studies under Thailand's Education Hub for Southern Region of ASEAN Countries (TEH-AC)
2. PSU. GS. Financial Support for Thesis (Fiscal Year 2016)